Experimental calibration of iron and multiple sulfur isotope fractionation processes relevant to mid-ocean ridge hydrothermal systems

A Dissertation
SUBMITTED TO THE FACULTY OF THE
UNIVERSITY OF MINNESOTA
BY

Drew D. Syverson

IN PARTIAL FULFILLMENT OF THE REQUIREMENTS
FOR THE DEGREE OF
DOCTOR OF PHILOSOPHY

Adviser: William E. Seyfried, Jr.

July 2015

Acknowledgements

My time as a student at the University of Minnesota, in the great and beautiful city of Minneapolis, was by far the best choice I have made in my life yet. This previous statement is only true because of my family and all of the great people I have met and supported me throughout my independence as an adult. However, of all people that facilitated my development as a geochemist, I have to thank my advisor William (Bill) Seyfried. Bill and I have known each other for almost a decade, throughout my undergraduate and during the pursuit of my doctorate at the Department of Earth Sciences. Our relationship is unique, to say the least, and has taught me how to work with others better and to think critically of all aspects of research and life. Finally, Bill is a supreme leader in geochemistry and I am grateful to have had the opportunity to serve under his guidance. He allowed me to explore freely with my experimental efforts while providing timely research and political advice that made the path to completion much less tumultuous.

The congregations of people who make the Department of Earth Sciences at the University of Minnesota run smoothly and generate research must be acknowledged, as I wouldn't be here without them. First of all, I would like to thank Sharon Kressler and Kathy Ohler for making my residency at the Department pleasant and always providing a smile. I thank Rick Knurr, my long time wet-chemistry lab mate, for always being there when I had any question and when I needed samples analyzed desperately. An experimental hydrothermal geochemist won't get far without a machinist, therefore, I want to thank Robert Jones and Mark Griffith for providing assistance on solving the many mechanical problems I encountered in the lab. I would like to thank my lab mates

throughout my graduate tenure. Specifically thanking Nick Pester, Andrew Luhmann, Ben Tutolo, Peter Scheuermann, Timothy Kiesel, and Adam Schaen for all of the helpful and entertaining discussions we shared in the lab or occasionally over a couple of beers. I thank my friends, Kang Ding, Chunyang Tan, and Shijun Wu, for providing all of their engineering expertise and for sharing their culture and language with me. I thank Brandy Toner, David Borrok, Shuhei Ono, Pat Shanks, and Paul Craddock for collaborating with me and providing advice, effectively advancing my research efforts during my doctorate education. Finally, I thank my committee members, David Kohlstedt, Emi Ito, and Jake Bailey for their help facilitating my completion of my degree.

Last, but definitely not least, I thank my family and personal friends that have supported me throughout the various stages of my life. I would not be here without the love and support provided by my mother and father, Susan and Jerry, making me truly grateful to have such great parents. The best part about my family is that I have four loving taller brothers, Josh, Grant, Seth, and Shea, who have always been great to grow up with and are always willing to share their life experiences and keep up to date with each other. I thank my grandfather, Clifford Arnold Stanley, for inspiring me to be a nice and caring person to all persons and for buying me fireworks as a kid. My best friends from Jamestown, ND, Jon Kemmis and Austin Tarno, definitely deserve a big thank you for always sticking with me when I moved to the “big city”. I would like to thank my best Minneapolis bike friends, specifically Spencer Niebuhr, Ben Tutolo, William Nachlas, and Steven Pupp, for joining me in the collective obsession of riding bikes in all types of extreme weather. I want to thank Ann Goyette for being an exemplary individual. Finally, I want to thank Rita Greenberg, Mike Anderson, Gauri Jadhav, and Richard Crockett for

being my extended siblings in Minneapolis and for taking care of me during some of the most interesting moments I have experienced here throughout the last decade.

Specific acknowledgements for Chapter 1.

I would like to thank the co-authors Dr. William Seyfried and Dr. David Borrok (UL at Lafayette). William helped inspire me to tackle the problem of Fe isotope fractionation and exchange processes at hydrothermal conditions, a relatively new research undertaking in geochemistry. I thank David Borrok for his constructive comments and for performing the Fe isotope sample processing and analyses by MC-ICP-MS at the University of Texas at El Paso. We thank Rick Knurr (UMN) for providing detailed sample analyses of the aqueous samples presented here. We also thank the Experimental Petrology Group (UMN) for providing the welding equipment necessary to accomplish this study. The authors thank the associate editor Dr. N. Dauphas, Dr. M. Zuilen, and two anonymous reviewers for providing constructive reviews that significantly improved the manuscript. This work was supported by the financial assistance of the NSF Grants OCE-1232704 (WES) and OCE-1061308 (DMB).

Specific Acknowledgments for Chapter 2.

I would like to thank the co-authors, Dr. Shuhei Ono (MIT), Dr. Pat Shanks (USGS), and Dr. William Seyfried (UMN) for their contributions to this work. Specifically, Shuhei and Pat always provided me constructive advice and were always there for questions to help clarify multiple S isotope systematics. Shuhei provided the opportunity to me to work in his lab at MIT to learn how to process S isotope samples for

analysis by GC-ICP-MS. Pat gave his expert advice in S isotope systematics of natural oceanic hydrothermal systems, facilitating the application of the naturally derived data to the newly revised experimental results. In particular for William Seyfried, he provided many great discussions, of which, were debated extensively, overall making this research effort more fulfilling. We would like to thank Rick Knurr (UMN) for providing detailed chemical analyses of the solution samples described here. We thank Dr. Nicholas Seaton (UMN) for providing his expertise in SEM imaging and Beth Fisher (UMN) for providing assistance with surface area analysis by gas adsorption techniques. I would like to personally thank Dr. Harry Oduro (MIT) and Dr. Jill McDermott (MIT) for providing essential instruction and assistance on the various techniques necessary for processing S isotope samples. This study was partially funded by the Doctoral Dissertation Fellowship from the University of Minnesota and chiefly funded by the NSF-OCE awards 1233257 (SO) and 1232704 (WES).

Specific acknowledgements for Chapter 3.

I would like to thank all of the co-authors of this study for making this research effort possible, Dr. Nick Pester (UMN/LBNL), Dr. Paul Craddock (UC/Schlumberger), and Dr. William Seyfried (UMN). Nick provided the experimental samples derived from his doctorate work. Paul helped me process the Fe isotope samples and he analyzed the Fe isotope composition of such samples by MC-ICP-MS at the Origins Laboratory at University of Chicago. The authors would like to thank the two anonymous reviewers and the associate editor, Dr. Bernard Marty, for their constructive comments, which made this paper undoubtedly more clear. We would also like to thank Rick Knurr (UMN) for

providing detailed chemical analyses of the fluid samples provided. The authors are grateful for the funding provided by the NSF grants OCE 0751771, 1061308, and 1232704 (WES). The corresponding author also acknowledges funding awarded by the University of Minnesota through the Doctoral Dissertation Fellowship during a portion of this research.

Dedication

To my family

Abstract

Mid-ocean ridge hydrothermal systems experience a multitude of physiochemical processes, which control the fate of metals leached from the crust as a consequence of changes in pressure, temperature, and chemical conditions along the fluid flow pathway in the subseafloor. The processes of phase separation, conductive cooling, and mixing of hydrothermal fluids with seawater, for example, can all induce changes in the saturation state of sulfides, effectively enriching metals as seafloor sulfide deposits. However, these specific processes are not well understood with respect to the nature of isotopic partitioning of metals and of sulfur between minerals and constituent aqueous species. Furthermore, recent advances in mass-spectrometry now allow the perspective of non-traditional isotope systems, such as iron (Fe) and low-abundance isotopes of sulfur (S), capable of examination. Thus, this set of studies focuses on three main processes, 1) rapid precipitation and 2) recrystallization of pyrite, and 3) phase separation of metal-bearing fluids, which have been attributed to enrichment of metal sulfides at the seafloor and by controlling the composition of hydrothermal fluids emitting from the oceanic crust. Chapters 1 and 2 focus on Fe and multiple S isotope systematics associated with pyrite and dissolved constituent aqueous species at 300-350°C and 500 bars during rapid precipitation and recrystallization. This experimental dataset provides important calibrations to the Fe and S isotope systems that were either lacking or inaccurate, consequently providing important constraints on theoretical predictions and the Fe and S isotope fractionations observed at mid-ocean ridge hydrothermal systems. Correspondingly, the complimentary Fe and S isotope data are applied to the East Pacific Rise 9-10°N mid-ocean ridge hydrothermal system, where the natural data suggests that pyrite is typically is in disequilibrium with high temperature vent fluids and is indicative of forming from FeS precursors. The focus of Chapter 3 is on the observed Fe isotope fractionation between vapor and liquid phases during phase separation of a Fe- and NaCl-bearing solution at pressure and temperature conditions indicative of volcanic activity in the shallow subseafloor along the mid-ocean ridge system. These data provide insight on how mass transport of Fe and the associated isotope fractionation between phases is a function of differences in speciation of Fe-Cl complexes during isothermal decompression, where the vapor phase is isotopically enriched in the heavy isotopes of Fe and consists of the neutral $FeCl_2$ complex while the chloride rich liquid phase is depleted and is dominated by the $FeCl_4^{2-}$ complex in solution.

Table of Contents

Chapter 1

Experimental determination of equilibrium Fe isotopic fractionation between pyrite and dissolved Fe under hydrothermal conditions

Chapter 2

Multiple Sulfur Isotope Fractionation and Mass Transfer Processes during Pyrite Precipitation and Recrystallization: An Experimental Study at 300 and 350°C

Chapter 3

Fe isotope fractionation during phase separation in the NaCl-H_2O System: An experimental study with implications for seafloor hydrothermal vents

List of Tables

Chapter 1

Chapter 2

Chapter 3

List of Figures

Chapter 1

Chapter 2

Chapter 3

Introduction

High temperature hydrothermal vent fields formed along Earth's mid-ocean ridge (MOR) system have been studied extensively since their discovery in the 1970's. Past field and experimental studies, by implementation of a variety of geochemical and geophysical techniques, have suggested that a multitude of hydrothermal processes occur deep in the crust and at the seafloor, providing important observational insight on the pervasiveness of hydrothermal alteration of the oceanic crust, formation of ore deposits, and the origins of life in extreme environments [*Alt and Teagle*, 1999; *Berndt et al.*, 1988; *Cole et al.*, 1987; *Seewald and Seyfried*, 1990; *Seyfried and Bischoff*, 1979; *Sleep et al.*, 2004]. Specifically, by use of increasingly sophisticated mass spectrometers, a new suite of geochemical tracers, iron (^{54,56,57,58}Fe) and sulfur (^{32,33,34,36}S) isotopes, are now utilized to gain a better understanding of biological and inorganic processes controlling the isotopic signatures of minerals and fluids evolved at hydrothermal systems [*Alt and Shanks*, 2011; *Bennett et al.*, 2009; *McDermott et al.*, 2015; *Ono et al.*, 2012; *Rouxel et al.*, 2008]. These hydrothermal processes inferred from Fe and S isotope systematics by analysis of natural data, however, have not been coupled with controlled experiments performed at relevant pressure, temperature, and chemical conditions to ensure an accurate interpretation of MOR hydrothermal systems. With these particular experimental constraints, the magnitude and relative importance, on an Earth system geochemical budget, of specific elemental fluxes, as a consequence of mid-ocean ridge hydrothermal activity, can be better quantified.

The primary basis of evaluating the processes that control the Fe and S isotopic composition of mineral and fluid samples derived from natural hydrothermal systems

along the MOR system is through the perspective of equilibrium predictions, of which, are derived from theory by use of first-principles calculations or spectroscopic measurements or from limited experimental data [*Blanchard et al.*, 2009; *Czarnacki and Hałas*, 2012; *Hill and Schauble*, 2008; *Ohmoto and Rye*, 1979; *Otake et al.*, 2008; *Polyakov and Soultanov*, 2011; *Rustad et al.*, 2010; *Schauble et al.*, 2001]. Theoretical predictions provide important constraints on the chemical and structural factors controlling the equilibrium distribution of Fe and S isotopes between mineral phases and dissolved constituents at a range of pressure, temperature, and chemical conditions. However, the combination of predictions from each theoretical model used can propagate large uncertainties when considering the different assumptions implemented for each chemical system imposed, such as between mineral-*mineral* versus mineral-*fluid* fractionation predictions [*Beard et al.*, 2010; *Blanchard et al.*, 2014]. Furthermore, theoretical predictions only provide information regarding equilibrium isotope fractionation systematics and do not consider pathway dependent isotope fractionation effects. Thus, experimental research efforts focusing on the verification of equilibrium predictions derived from theory while performing dynamic experiments emulating physiochemical processes indicative of MOR hydrothermal systems are greatly warranted, as few experimental data exist.

Thus, the set of experimental studies described in the following chapters of this dissertation will focus on three physiochemical processes that occur ubiquitously at MOR hydrothermal systems and have been proposed to induce significant differences in the Fe and S isotope composition amongst minerals and fluids: 1) rapid precipitation and 2) recrystallization of pyrite at hydrothermal conditions; 3) phase separation of Fe-bearing

NaCl-H_2O fluids at elevated temperatures and moderately low pressures indicative of water-rock interactions in the shallow oceanic crust. The Fe and S isotopic data produced from this set of studies are then used to compile a self-consistent fractionation database, which is compared to equilibrium predictions produced by theoretical calculations and from available Fe and S isotope data of pyrite and hydrothermal fluids sampled from active high temperature MOR hydrothermal systems.

Chapter 1: Experimental determination of equilibrium Fe isotopic fractionation between pyrite and dissolved Fe under hydrothermal conditions

Drew D. Syverson [a], David M. Borrok [b], William E. Seyfried, Jr. [a]

[a] *Department of Earth Sciences, University of Minnesota*
310 Pillsbury Drive, S.E., Minneapolis, Minnesota 55455-0231

[b] *School of Geosciences, University of Louisiana at Lafayette*
200 East University Ave, Lafayette, Louisiana 70504

Published in *Geochimica et Cosmochimica Acta,* vol. 122 (2013), pp. 170-183

Used with permission of the co-authors and by Elsevier Publishing

1.0. Summary

Fe isotope fractionation between pyrite (FeS_2) and dissolved Fe in NaCl- and sulfur-bearing aqueous fluids was determined under hydrothermal conditions (300-350°C, 500 bars). The data were collected using two different, but complementary, experimental approaches, one involving classical Fe isotope exchange between Fe in pyrite and dissolved Fe in coexisting fluid, while the other involved homogenous precipitation of pyrite in a redox and pH buffered chemical system. Results from these experiments indicate equilibrium Fe isotopic fractionation between pyrite and fluid, $\Delta^{56}Fe_{Pyr\text{-}Fe(aq)}$, of 0.99±0.29‰ (2σ), in $^{56}Fe/^{54}Fe$. The experimentally determined equilibrium pyrite-fluid Fe isotopic fractionation agrees with theoretical and spectrally-based predictions. The second series of experiments were conducted to better constrain the effect of precipitation rate on the temporal evolution of the Fe isotopic composition of pyrite and Fe bearing fluids in dynamic mixing environments, such as hydrothermal vent sites at mid-ocean

ridges. Rapid homogenous precipitation of pyrite at 300 and 350°C indicates that δ^{56}Fe of dissolved Fe is significantly greater than pyrite that formed during the earliest stage of the experiment, possibly facilitated by either equilibrium or kinetic isotope effects involving FeS as a reactant during pyrite formation. Subsequent recrystallization of pyrite results in a Fe isotopic fractionation with dissolved Fe that moves towards the experimentally determined equilibrium Fe isotopic fractionation with reaction progress. The experimental data reported here may help to decipher the complex kinetic and thermodynamic processes involved in pyrite formation at deep sea vents, while also providing constraints for the rapidly developing theoretical models used to estimate equilibrium Fe isotope fractionation between pyrite and fluid at elevated temperatures and pressures.

1.1. Introduction

There has been considerable debate regarding different mechanisms of pyrite formation in experimental and natural systems [*Butler and Rickard*, 2000; *Butler et al.*, 2004; *Ono et al.*, 2007; *Rickard and Luther*, 1997; 2007; *Schoonen and Barnes*, 1991; *Wilkin and Barnes*, 1996]. An important part of this debate is determining whether the observed Fe isotopic fractionations between Fe-sulfides and fluids collected at active high-temperature hydrothermal systems are representative of Fe isotopic equilibrium [*Polyakov and Soultanov*, 2011; *Rouxel et al.*, 2004; *Rouxel et al.*, 2008]. Current field data [*Beard et al.*, 2003; *Rouxel et al.*, 2004; *Rouxel et al.*, 2008; *Sharma et al.*, 2001] in conjunction with theoretical predictions [*Anbar et al.*, 2005; *Blanchard et al.*, 2009;

Rustad et al., 2010; *Schauble et al.*, 2001] and spectral data (Mössbauer spectroscopy, inelastic resonant X-ray scattering (INRXS)) [*Polyakov and Soultanov*, 2011; *Polyakov et al.*, 2007] suggest that the Fe isotopic composition of pyrite may not have equilibrated with dissolved Fe in coexisting hydrothermal fluid and with surrounding metal sulfides, such as chalcopyrite, in hydrothermal chimney structures at various active vent fields along the world's mid-ocean ridges. Furthermore, S-isotope disequilibrium between pyrite and coexisting hydrothermal vent fluids has been frequently attributed to the rapid precipitation of pyrite and limited isotopic exchange with aqueous S-species in hydrothermal vent systems [*Ono et al.*, 2007; *Shanks and Seyfried*, 1987; *Woodruff and Shanks*, 1988; *Yücel et al.*, 2011]. *Rouxel et al.* [2008] have explained that the Fe isotopic composition of pyrite may experience kinetic isotopic effects, such as rate-limiting exchange between $FeS_{(aq)}$ and $Fe(H_2O)^{2+}$ species [*Butler et al.*, 2005], during the rapid precipitation of FeS(s) and subsequent conversion to pyrite. This would result in the enrichment of the lighter isotopes of Fe in pyrite relative to dissolved Fe, contradicting predictions based on equilibrium Fe isotopic fractionation. The mechanism of pyrite formation through FeS reactants has been used to explain the Fe isotopic composition of pyrite relative to dissolved Fe at EPR 9-10°N [*Polyakov and Soultanov*, 2011]. By this interpretation, pyrite inherits its Fe isotope composition from the reactant phase (FeS), which subsequently changes slowly or not at all owing to sluggish rates of isotopic exchange between pyrite and dissolved Fe in the surrounding fluid. The persistent Fe isotopic inheritance of the reactant FeS phase in pyrite has also been experimentally observed at 100°C by *Guilbaud et al.* [2011a] during the formation of pyrite from FeS by

the H_2S pathway.

This study reports the first experimental Fe isotope fractionation data between pyrite and Fe-bearing aqueous fluid at hydrothermal temperatures and pressures (300-350°C, 500 bars), conditions particularly relevant to the formation of pyrite at deep-sea hydrothermal vents. Owing to the lack of experimental data of the type reported here, it is often necessary to extrapolate theoretical predictions and available experimental data obtained at ambient near-surface conditions to other chemical and physical conditions to provide support for one interpretation or another on mineral formation mechanism under hydrothermal conditions. Extrapolation of this sort necessarily involves large differences in temperature, pressure, and chemical composition, and thus, is subject to uncertainty. There can be no question that a wide range of field and theoretical studies would benefit from metal sulfide precipitation experiments and Fe isotope exchange experiments between pyrite and dissolved Fe at conditions more relevant to the formation of these phases in nature. Moreover, experimentally determined Mössbauer, INRXS, and theoretically determined β-factors, where $\Delta^{56}Fe_{A\text{-}B}(‰) \approx 10^3 ln\alpha^{56}_{A\text{-}B} = 10^3 ln\beta_A - 10^3 ln\beta_B$ [*Blanchard et al.*, 2009; *Polyakov and Soultanov*, 2011; *Rustad et al.*, 2010], need experimental verification, especially when used to predict equilibrium mineral-*fluid* fractionation [*Beard et al.*, 2010].

1.2. Experimental Design

1.2.1. Fe isotope partial exchange experiments

The partial-exchange approach [*Criss*, 1999; *Northrop and Clayton*, 1966;

Schuessler et al., 2007] was used to determine the equilibrium Fe isotope fractionation between pyrite and Fe-bearing fluid at experimental conditions. The Fe isotopic composition of the fluid and solid (pyrite) reactants were varied to maximize differences in their isotope compositions. For example, one pyrite reactant was hydrothermally synthesized by sulfidation of hematite. It is well recognized from theoretical and experimental data [*Hill et al.*, 2009; *Polyakov and Mineev*, 2000; *Schauble et al.*, 2001; *Skulan et al.*, 2002] that ferric Fe tends to be enriched in isotopically heavy Fe, and thus, pyrite derived from hematite can be expected to inherit this enrichment. This synthetically derived pyrite is referred to as Pyr1 in the Fe isotope exchange experiments. The synthetic pyrite crystals were produced in experiments performed in a titanium reactor with 103 cm^3 volume, which was of sufficient size to yield the amounts of pyrite needed to complete the exchange experiments. A second synthetic pyrite (Pyr2) was acquired from NanoCorps™. This pyrite is isotopically distinct (i.e., lighter) from that synthesized from hematite in our lab (Pyr1). Pyr2 is composed of sub-micron grains of pyrite, which were acid washed in boiling 6N HCl prior to use to remove any potential mineral or chemical contaminants. The third pyrite crystal (Pyr3) was naturally derived, and obtained from the research mineral collection at the University of Minnesota. This pyrite is isotopically lighter than Pyr2. It was ground under acetone, acid washed in boiling 6N HCl, and subsequently dried. Thus, all of the pyrite reactants used for the isotope exchange experiments were fine grained with sizes generally less than 50μm, very well crystallized, and associated with no other minerals, as indicated by X-ray diffraction analysis and SEM examination. In keeping with the overall experimental

strategy of enhancing Fe isotopic differences between pyrite and coexisting fluid, multiple Fe sources with distinct Fe isotope compositions (Table 1.1) were used to prepare the fluids for the exchange experiments. For example, analytical grade $FeCl_2 \bullet 4H_2O$ salt (RF1) and native Fe (RF2) were dissolved under nitrogen in water and HCl, respectively. The solutions were then diluted with distilled, de-ionized water, while the pH was slowly adjusted with NaOH or HCl, under nitrogen, to achieve a final concentration of dissolved Fe and $pH_{25°C}$ of approximately 20 mmol/kg and 1.5, respectively. The relatively low pH was needed to enhance the solubility of Fe coexisting with pyrite at experimental conditions, while also precluding possible formation of any other Fe-bearing mineral, as indicated by theoretical modeling results and results of "trial" hydrothermal experiments performed in our lab. The total dissolved Cl^- of the solutions was adjusted with analytical grade NaCl to obtain a concentration of ~1 mol/kg. Even in the moderately acidic fluids, at experimental conditions, however, the solubility of pyrite is limited, and thus, XFe_{Pyr} (mol % Fe in pyrite) was greater than 97% in all low fluid/mineral (F/M) ratio experiments (Table 1.2), effectively establishing a mineral (pyrite) buffered system. The relatively low F/M ratio at which these experiments were performed (0.2 grams pyrite and 2.5 grams Fe-bearing fluid) was largely a result of the volumetric limitations of the gold capsules used for the experiments (see below). Thus, the Fe isotopic composition of the fluid is a particularly sensitive indicator of the extent of isotope exchange, while the opposite is true of the coexisting pyrite crystals. The starting Fe isotopic composition of each individual fluid and pyrite used as a reactant is listed in Table 1.3. As a result of the pyrite buffered system for the low F/M

experiments, the initial pyrite Fe isotopic composition is accepted as the final Fe isotopic composition, since the Fe isotopic composition of the pyrite will not change (within analytical error) owing to constraints imposed by the relative abundance and the Fe isotopic composition of the pyrite and Fe-bearing fluid.

The exchange experiments were performed using closed flexible gold capsules (0.25 cm outer diameter, 0.20 mm wall thickness, 10 cm length, 4 ml internal volume) contained within a steel pressure vessel. The pressure vessel was enclosed in an insulated furnace, with multi-zone heating elements to eliminate thermal gradients. Temperature and pressure control of the experimental system is described in detail in section 2.2. The gold capsules were welded at one end before loading with solid and fluid reactants. In addition to the pyrite and Fe bearing fluid, a sufficient amount of native sulfur (5-10 mg) was added to each of the capsules to further assure pyrite stability at experimental conditions. The addition of native sulfur was always less than that needed to reach sulfur saturation during hydrolysis [*Ohmoto et al.*, 1994]. After loading the solid and fluid reactants, each gold capsule was purged with Ar gas to remove air before the open end was squeezed in a vice to create an initial seal. This seal was then arc welded while the capsule was submerged in liquid nitrogen to prevent heating of the capsule contents. The weight of the sealed capsule was then compared to the initial weight of the unsealed gold capsule plus the fluid and solid reactants. Sealed capsules that differed from the initial weight (before welding) by more than 1% were not used, and a replacement capsule was prepared and tested using a similar procedure. For the low F/M system exchange experiments, a total of four gold capsules were prepared.

The isotope exchange experiments for the four gold capsules were conducted at 350°C and 500 bars for 3384 hours, approximately the same amount of time needed for sulfur isotope exchange experiments involving pyrite to achieve near-complete exchange at a similar temperature [*Kajiwara and Krouse*, 1971; *Kajiwara et al.*, 1969; *Smith et al.*, 1977]. After the reaction duration, the pressure vessel was quenched rapidly, on the order of 5 minutes, by removing the pressure vessel from the furnace and exposing it to a high pressure stream of air. At the same time, the internal pressure was maintained at 150-300 bars, by a computer-controlled ISCO water pump, until a temperature of 150°C was achieved. The addition of the water more rapidly cooled the pressure vessel, but also maintained pressure on the gold capsules, enhancing the solubility of H_2S. Immediately after the pressure vessel was quenched and opened, the capsules were retrieved, and then cleaned (H_2O rinse) and weighed. The contents of each gold capsule (oriented vertically) were immediately frozen. Each capsule was then subjected to a sparging procedure to remove and recover H_2S produced from the partial dissolution of pyrite and hydrolysis of coexisting sulfur. In effect, this involved vertically placing each gold capsule, with contents still frozen in a gas-tight glass-sparging cell. The top of the capsule was punctured by a syringe needle, which had access to the capsule by a rubber septum external to the sparging-cell. A stream of high-purity Ar served as a carrier gas to transport H_2S to $AgNO_3$ solution that trapped it as Ag_2S. Full recovery of H_2S was facilitated by an external water bath that warmed the glass-sparging cell. Following quantitative recovery of Ag_2S, the gold capsule was then opened completely in an N_2 environment, and the fluid passed through a 0.2μm nylon filter while the pyrite crystals

were simultaneously separated from the coexisting fluid, rinsed with deionized water, and dried. The pyrite and fluid fractions were stored in acid-washed Savillex™ bottles prior to processing for Fe isotope analysis. An aliquot of the quenched solution was analyzed by ICP-OES for major and trace cations, while anions were determined by ion chromatography. The relative standard deviation (2σ) for the concentration of the individual dissolved components measured by ICP-OES and ion chromatography is ±2% for Na^+ and SO_4^{2-}, ±1% for Fe^{2+}, and ±1% for Cl^-. The relative standard deviation associated with measuring dissolved H_2S, determined from repeated Ag_2S gravimetric measurements of known amounts of H_2S derived from the decomposition of thioacetamide (C_2H_5NS) at high temperature, is ±3%. The pH was measured with a Thermo-Ross™ glass electrode, which was standardized prior to each solution allocation, and has an uncertainty of ±0.01 log units.

In addition to the four low F/M gold capsule exchange experiments, one Fe isotopic exchange experiment was performed with XFe_{Pyr} of 22% (high F/M #1) using a large gold cell (~78 cm^3). The experiment was performed for an identical length of time as the gold capsule experiments, facilitating comparison with these more pyrite-dominated experiments. Moreover, the experiment utilized ~0.1g of synthetic sub-micron pyrite (Pyr2) and a solution (RF3) containing ~56 mmol/kg $FeCl_2$ and ~1700 mmol/kg NaCl (Table 1.1), with a Fe isotope composition distinct from that used for the capsule experiments. The different Fe mass and isotope balances between the capsule and large volume gold cell experiments promoted the variability needed to better and more accurately determine the magnitude of Fe isotope exchange between pyrite and fluid. It is

important to note that in addition to the isotope variability noted above, the fluid used for the large volume gold cell exchange experiment was also characterized by relatively high concentrations of $Na_2S_2O_3$, Fe, and low pH (Table 1.1-1.2). These compositional modifications were made to again assure only pyrite-fluid equilibria at experimental conditions. As with other experiments using the large volume gold cell (see below), the head space above the fluid was flushed with nitrogen prior to closing a sampling valve external to the pressure vessel in which the cell was secured [*Seyfried et al.*, 1987]. The temperature and pressure were then brought to 350°C and 500 bars by activating temperature and pressure control systems. *In-situ* solution samples were taken at the beginning and end of the experiment to assess the Fe isotopic composition of the solution with reaction progress taking explicit account of this on chemical and isotope mass balances. The procedures implemented for processing and storing sampled solutions and pyrite are the same as the low F/M exchange experiments, as described above in section 1.2.1.

The advantage of supplementing the small volume gold capsule exchange experiments with the large volume gold cell experiment is that the latter permitted sufficient distribution of Fe in the fluid so as to cause a predictable and measureable change in the Fe isotope composition of pyrite. Thus, both the Fe isotope composition of the fluid and coexisting pyrite provided constraints for mineral-fluid fractionation processes.

1.2.2. Homogenous precipitation of pyrite

Flexible gold reaction cell technology [*Seyfried et al.*, 1987] was used to conduct

pyrite precipitation experiments at 300 and 350°C, 500 bars to examine the effect of this on Fe isotope systematics. Modifications, however, to the flexible gold cell were required. For example, the commercial grade-1 titanium that typically serves as the closure for the gold cell was replaced with a functionally similar device composed of grade-7 titanium (Pd-Ti), which is more resistant to reaction in acidic and Cl^- bearing fluid. Similar to the capsule experiments, the starting (reactant) solutions used for these experiments were prepared from analytical grade $FeCl_2 \bullet 4H_2O$, NaCl, and deionized water. Initially, the deformable gold cell (~78 cm^3) was filled under nitrogen with an appropriate amount $FeCl_2$ and NaCl, ~38 mmol/kg and ~1000 mmol/kg, respectively. The combined contents of the fluid were rendered acidic (pH ~ 1) to preclude precipitation of Fe-bearing minerals prior to heat up to experimental conditions. The ~38 mmol/kg Fe solutions were utilized to provide sufficient Fe for pyrite precipitation without exhausting the dissolved Fe inventory. Thus, the high Fe concentration during and after pyrite precipitation permitted steady state conditions to be achieved, providing some degree of buffering of dissolved Fe and its Fe isotopic composition during subsequent pyrite recrystallization reactions (see below). A key advantage of the flexible gold cell system is that it allows fluid reactants to be added and internally filtered fluid samples to be removed at any point in an experiment without changing temperature or pressure [*Seyfried et al.*, 1987].

Temperature control of these experiments was provided by a type-K thermocouple inserted directly into the fluid (H_2O) reservoir of the pressure vessel external to the gold reaction cell [*Seyfried et al.*, 1987]. The pressure vessel in turn was

secured in a furnace with temperature maintained constant (±2°C) by a time proportioning controller linked to the internal thermocouple. Pressure control was provided by a Heise analogue gauge with an uncertainty of approximately 0.1% of the operating pressure. The pressure vessel and its contents as well as the temperature control and fluid sampling systems rotate on an 180° axis approximately 10 times per minute, facilitating complete mixing of the contents of the gold reaction cell, while enhancing reaction between the fluid and coexisting minerals.

Once the desired temperature and pressure of the experiment were achieved, the $FeCl_2$ solution was sampled to verify that the initial Fe isotope composition and total dissolved Fe were consistent with constraints imposed by reactant abundance and composition. Subsequently, approximately 4-6 grams of a ~1 mol/kg solution $Na_2S_2O_3$ (Na□thiosulfate) was added to the contents of the gold cell by an HPLC pump, which metered the rate of fluid delivery through the sampling valve, while an external back pressure regulator simultaneously released fluid (H_2O) from the reservoir surrounding the gold cell, thereby maintaining the pressure of the hydrothermal system at the desired value. $Na_2S_2O_3$ undergoes hydrolysis to H_2S and SO_4^{2-} in a ratio of 1:1 (reaction 1), which induces pyrite precipitation upon interaction with the acidic $FeCl_2$ solution (reaction 2) [*Pokrovski et al.*, 2008; *Schoonen and Barnes*, 1991]. Although reaction 2 depicts the generation of dissolved H_2 in response to pyrite formation, in actuality this is limited by the presence of excess SO_4^{2-}, which by design serves as a redox buffer during the experiment. In effect, the experimental strategy used here takes explicit account of the relative abundances of $FeCl_2$ and $Na_2S_2O_3$ (together with imposed temperature, pressure,

and pH constraints) to achieve formation of a fixed (and predictable) amount of pyrite, while precluding formation of any other Fe-bearing mineral. This was confirmed by analysis of reaction products upon termination of the experiment by X-ray diffraction and by scanning electron microscopy.

$$Na_2S_2O_3 + H_2O \rightarrow H_2S + SO_4^{2-} + 2Na^+ \quad (1.1)$$

$$FeCl_2 + 2H_2S \rightarrow FeS_2 + H_2(aq) + 2H^+ + 2Cl^- \quad (1.2)$$

Subsequent to the addition of $Na_2S_2O_3$, fluid samples were taken at different time intervals to demonstrate the chemical and isotopic evolution of the system. The first sample from all of the precipitation experiments was taken less than one hour after the $Na_2S_2O_3$ injection (Table 1.2). This was done to better determine the initial Fe isotopic fractionation between precipitated pyrite and fluid (by Fe isotopic mass balance constraints), as well as the extent of pyrite precipitation (bulk Fe mass balance constraints). Time series samples from both the 300 and 350°C experiments were optimized to provide different information. For example, we assume that the sampling and short duration of the relatively low temperature 300°C experiment is better suited for data on the initial Fe isotopic fractionation between pyrite and fluid, while the longer term 350°C experiments with intermittent sampling better constrains information regarding pyrite-fluid recrystallization processes. Neither experiment afforded the opportunity for simultaneous sampling of the coexisting pyrite crystals at experimental conditions, information which, if available, could have provided more quantitative constraints on the processes inferred above from the temperature and sequence of samples acquired from analysis of the fluid alone.

The procedures implemented for storing the precipitated pyrite and $FeCl_2$ solutions sampled subsequent to the experiment are identical to the procedures used in the exchange experiments described in section 2.1. Dissolved H_2S concentrations were determined from the precipitation experiments by sampling the solutions at conditions with a gas-tight syringe attached to the sample valve external to the pressure vessel and subsequently injecting the solution (weight determined) into a glass-sparging system that carries the evolved H_2S into a $AgNO_3$ solution, trapped as Ag_2S, which was subsequently filtered and weighted (RSD = 3%). Other more stable components of the fluid (Fe^{2+}, SO_4^{2-}, Cl^-, and pH) were sampled and stored as previously described (section 1.2.1).

1.2.3. Fe isotope measurements

The Fe isotope composition of all Fe-bearing fluids and pyrite from the hydrothermal experiments were measured using a Nu Instruments MC-ICP-MS at the Center for Earth and Environmental Isotope Research at University of Texas El Paso. Fe separation and purification was achieved using anion-exchange column procedures to quantitatively isolate Fe from the experimental solution matrix [*Borrok et al.*, 2007]. Quantitative recovery of Fe after the column procedure was confirmed with independent measurements of dissolved Fe by ICP-MS performed at the Department of Earth Sciences at the University of Minnesota-Twin Cities. The MC-ICP-MS was set at "pseudo-high resolution mode" to differentiate N- and O-argide interferences overlapping into the peaks of ^{54}Fe, ^{56}Fe, and ^{57}Fe. All Fe isotopic ratios represented in delta notation in this

study are referenced with respect to the IRMM-14 Fe standard, which was subjected to the same preparation and column procedure:

$$\delta^{x}Fe = \left[\frac{R^{x/54}}{R^{x/54}_{IRMM-14}} - 1\right] * 10^{3} \quad \text{where x = 56 or 57} \qquad (1.3)$$

The Fe isotopic analysis procedure implemented the "standard-sample-standard" bracketing technique to account for mass bias and drift [*Borrok et al.*, 2009; *Dauphas et al.*, 2009]. Analytical precision for individual samples reported in this study was based on the 2σ deviation from the average of two or more replicates. Confirmation of the accuracy and precision of the Fe isotope measurements of the experimental samples was further tested by comparing these data with in-house standards and external reference materials, including BCR-2. The δ^{56}Fe of BCR-2 from 10 replicates, including samples from separate column preparation, measured over 4 separate analytical sessions was 0.119 ± 0.060‰. The voltage intensity of the procedural column blanks was compared against those for samples and the blank contributions were found to be negligible, less than 0.01% of the sample voltage. The linear regression of δ^{57}Fe versus δ^{56}Fe of all samples used in this study (Fig. 1.1) demonstrates that the Fe isotopic data conform to the predicted mass dependent fractionation relationship for Fe ($\delta^{57}Fe=1.47\times\delta^{56}Fe$).

1.3. Results and Discussion

1.3.1. Solution chemistry, speciation calculations, and pyrite solubility

The dissolved concentrations of experimental solutions sampled from exchange and precipitation experiments were used to determined pH and redox constraints at experimental conditions. These data could then be compared with theoretical models of

pyrite-fluid equilibria to show that phase equilibria had indeed been achieved. To accomplish this, however, distributions of aqueous species calculations were necessary. For these calculations, the standard states for the solids are defined as unit activity for pure end-member solids at the temperature and pressure of interest. The standard state for water is the unit activity of pure water. For aqueous species other than H_2O, the standard state is the unit activity of the species in a hypothetical one molal solution referenced to infinite dilution at the temperature and pressure of interest (350°C and 500 bar). Standard state thermodynamic properties for pyrite were taken from *Johnson et al.* [1992], water from *Haar et al.* [1984], $NaCl_{(aq)}$ from *Ho et al.* [2000], and all other aqueous species from *Shock and Helgeson* [1988], *Shock et al.* [1989], *Shock et al.* [1997], and *Sverjensky et al.* [1997], except $FeCl^{+}_{(aq)}$ and $FeCl_2°_{(aq)}$, which are from *Ding and Seyfried* [1992]. The temperature and pressure dependencies of thermodynamic properties for aqueous species, when applicable, were predicted using the parameters of the revised Helgeson-Kirkham-Flower equations of state for aqueous species [*Helgeson et al.*, 1981; *Shock et al.*, 1992; *Tanger and Helgeson*, 1988]. Calculations of equilibrium constants were facilitated with a modified version of SUPCRT92 [*Johnson et al.*, 1992; *Kong et al.*, 2013]. Speciation and solubility calculations were aided with the computer code GWB [*Bethke*, 2006]. Activity coefficients for the charged aqueous species were calculated from the extended Debye-Hückel equation or B-dot equation fitted to mean salt NaCl activity coefficients [*Helgeson et al.*, 1978; *Oelkers and Helgeson*, 1991]. The thermodynamic data and imposed constraints indicate that all fluid samples and derived aqueous species are in close agreement with pyrite-fluid equilibria at experimental

conditions (Fig. 1.2). Moreover, the data also indicate that owing to the low pH and activities of dissolved H_2S and SO_4^{2-}, which constrain the activity of dissolved H_2 (Fig. 1.2), Fe-bearing minerals other than pyrite are not stable or predicted to form. This is consistent with mineralogical examination of experimental run products.

The solution chemistry from the partial exchange experiments (low F/M #1-4 and high F/M #1-1 and #1-2) are shown in Table 1.1, where the initial $FeCl_2$ solutions are designated as RF1-RF3, while the final solutions for each gold capsule and large gold cell experiment are designated with the initial $FeCl_2$ solution and pyrite used, Pyr1-Pyr3. The exchange experiment product solutions are all within ~8% of their original dissolved Fe concentrations (RF1-RF3), the variability simply reflecting slight differences in total dissolve sulfur and pH unique to the different experiments. The high F/M #1 experiment, which allowed the initial (#1-1), and final solution (#1-2) to be sampled, indicates that the concentration of dissolved Fe remains relatively stable throughout the experiment. This experiment, however, has an elevated dissolved Cl^- (~1700 mmol/kg) and Fe (~56 mmol/kg) concentration, and low pH to enhance Fe solubility, in keeping with the overall rationale for this experiment (see above). Thus, the modeled results inherit these effects and account for the relative position of the modeled data in comparison with that from the pyrite-dominated capsule experiments (Fig. 1.2).

All of the solutions used for the pyrite precipitation experiments initially contained approximately 38 mmol/kg $FeCl_2$, 1000 mmol/kg NaCl, and no dissolved sulfur, as emphasized above. The injection of $Na_2S_2O_3$ into the Fe bearing system is predictably manifest by the observed increases in total dissolved SO_4^{2-} and H_2S, and

corresponding decrease in dissolved Fe (Table 1.2), in keeping with pyrite precipitation. The thermodynamically modeled fluid chemistry from the precipitation experiment at 350°C (Fig. 1.2) provides some confirmation of this. The relative lack of separation between the two fluid samples acquired with different degrees of reaction progress, however, suggests that the precipitation is rapid and followed by a stage of crystal growth (recrystallization) that is not particularly obvious by corresponding changes in the measured (Table 1.2) or thermodynamically modeled fluid chemistry (Fig. 1.2). Recrystallization effects following precipitation are apparent both at 300 and 350°C by changes in crystal morphology as revealed by SEM images (Fig. 1.3). Indeed, the short-term precipitation experiment at 300° displays a large degree of surface area heterogeneity, while pyrite crystals have a transitional morphology that is indicative of rapid formation from FeS(s) [*Graham and Ohmoto*, 1994]. Pyrite from the 350°C experiment, having reacted longer and at the higher temperature, is clearly better crystallized, and displays layer by layer growth towards a striated cubic-octahedral pyrite morphology in keeping with results and interpretations from earlier studies of pyrite precipitation and growth in hydrothermal experiments reported by *Murowchick and Barnes* [1987].

1.3.2. Fe isotope partial exchange between pyrite and dissolved Fe

The partial isotope exchange approach [*Criss*, 1999; *Northrop and Clayton*, 1966] was used in this study to determine the equilibrium Fe isotopic fractionation between pyrite and dissolved Fe, as shown:

$$10^3\ln(\alpha^{56}_{initial}) = 10^3\ln(\alpha^{56}_{equilibrium}) - 1/F*10^3[\ln(\alpha^{56}_{final}) - \ln(\alpha^{56}_{initial})] \qquad (1.4)$$

$$10^3 \ln\alpha^{56}_{\text{Pyr-Fe(aq)}} \approx \Delta^{56}\text{Fe}_{\text{Pyr-Fe(aq)}} = \delta^{56}\text{Fe}_{\text{Pyr}} - \delta^{56}\text{Fe}_{\text{Fe(aq)}} \quad (1.5)$$

This classic approach has primarily been applied to lighter isotope systems, such as those involving O and C, but has recently been used as well to determine the extent of exchange (F, Eq. 4) and the equilibrium Fe isotope fractionation factor between pyrrhotite and peralkaline melt at 840-1000°C [*Schuessler et al.*, 2007]. The value of this approach draws strength from its application to chemical systems at low to moderate temperatures where isotope exchange is incomplete. This approach, therefore, is particularly well suited to the present study, since it is well known that pyrite-fluid equilibria are sluggish, as indicated by results of field and theoretically based observations [*Bluth and Ohmoto*, 1988; *Ono et al.*, 2007; *Polyakov and Soultanov*, 2011; *Rouxel et al.*, 2004; *Rouxel et al.*, 2008; *Shanks and Seyfried*, 1987; *Woodruff and Shanks*, 1988].

The Fe isotope composition of all $FeCl_2$ solutions and pyrite before and after hydrothermal reaction, reveal changes in keeping with the exchange of isotopes at experimental conditions (Tables 1.3 and 1.4). Fe isotope exchange reflects constraints imposed by the initial Fe isotopic composition and relative abundance of reactant Fe sources and reaction progress. This is perhaps best illustrated by results from the exchange experiment with high F/M ratio (#1), where the mole percent of Fe in pyrite is only 22% of the total Fe inventory. The final Fe isotope composition of the fluid (high F/M #1-2) and pyrite (Pyr3R-high F/M) both change significantly in comparison with constraints imposed by the Fe isotope composition and relative abundances of the reactants (Tables 1.3 and 1.4). In contrast, pyrite from the gold capsule experiments,

where the mole fraction (percent) of Fe in pyrite is approximately 97%, cannot significantly change its isotope composition owing to the low fluid/mineral (pyrite) ratio and the slight difference in the Fe isotope composition of the pyrite and fluid reactants. As emphasized earlier, it is the Fe isotopic change of the fluid from each of the gold capsule experiments that provides the clearest measure of the extent of exchange and can best be used to calculate the fractionation of Fe isotopes between pyrite and the coexisting Fe bearing fluid. The initial, final, and the change in the Fe isotopic fractionation between pyrite and dissolved Fe for all experiments are reported in Table 1.4 and plotted in Fig. 1.4. Only the Fe isotopic composition of the initial reactant pyrite for the low F/M gold capsule experiments were analyzed, since the Fe isotope composition is effectively buffered, as described above.

The linear regression [*Mahon*, 1996; *York*, 1966] of the bivariate experimental data (dashed line in Fig. 1.4) results in an extrapolated (y-intercept) equilibrium Fe isotope fractionation factor between pyrite and dissolved Fe, $\Delta^{56}Fe_{Pyr\text{-}Fe(aq)}$, of 0.99±0.29‰. The slope (-1/F) suggests that ~64% exchange took place between pyrite and dissolved Fe within the experimental duration of 3384 hours. Equilibrium calculations of Fe isotope fractionation between pyrite and dissolved Fe, $\Delta^{56}Fe_{Pyr\text{-}Fe(aq)}$, at 350°C predict that pyrite should be isotopically enriched in the heavy isotopes of Fe relative to a coexisting Fe-bearing fluid by ~1.00-1.45‰ [*Blanchard et al.*, 2009; *Polyakov and Soultanov*, 2011; *Rustad et al.*, 2010]. The present study provides the first experimental data in support of the predicted direction of Fe isotope enrichment, while also demonstrating that the magnitude of the Fe isotopic fractionation tends to be in good

agreement with pyrite β-factors from *Blanchard et al.* [2009], when these data are combined with β-factors for aqueous Fe ($Fe(H_2O)^{2+}$) from *Rustad et al.* [2010] (Fig. 1.5). As emphasized previously (see *Beard et al.* [2010]), β-factors for mineral-mineral and fluid-fluid reactions tend to agree with available experimental data, while the opposite is true for mineral-fluid data. By using a common source for model data for aqueous Fe, we can better compare our data with available model data for pyrite, although this probably still underestimates the contribution of the fluid species uncertainties to the modeled pyrite-fluid data.

The experimental data for pyrite-fluid fractionation reported here conforms to a well-defined linear relationship, as expected for the exchange of isotopes between reactants in the course of pyrite recrystallization [*Northrop and Clayton*, 1966]. The use of two different types of experiments to gain additional separation between isotope reservoirs of the reactants adds confidence to the correlation we observed. In spite of the length of time for which the experiments were conducted (3384 hours), calculations indicate incomplete exchange, the relatively high temperature (350°C) notwithstanding. Indeed, the observed extent of Fe isotope exchange is significantly less than reported for sulfur isotope exchange between pyrite and coexisting sulfide minerals at a similar temperature [*Kajiwara and Krouse*, 1971; *Kajiwara et al.*, 1969; *Smith et al.*, 1977], underscoring the need to re-evaluate S isotopic exchange studies of sulfides and aqueous S-species with isotopic tracers, such as rare isotopes and enriched isotopic spikes, coupled with metal isotopic systems such as Fe, Cu, and Zn to assess the degree of equilibration between the phases of interest. Experiments of this sort in combination with

companion experiments implementing isotopic spikes (three-isotope method) can provide equilibrium fractionation factors at temperatures well below the moderately high temperatures used for the present study [*Guilbaud et al.*, 2011b; *Matsuhisa et al.*, 1978; *Shahar et al.*, 2008; *Wu et al.*, 2012].

As suggested above, differences between predicted and experimentally determined Fe isotopic fractionation data for pyrite-dissolved Fe^{2+} equilibria arise from uncertainties in β-factors for pyrite, but more importantly from extrapolation of aqueous Fe β-factors from ambient conditions to the P-T conditions of the experimental study. As of now, there have been a number of published Fe isotope *ab-initio* based studies [*Anbar et al.*, 2005; *Hill et al.*, 2010; *Rustad et al.*, 2010; *Schauble et al.*, 2001] that have evaluated the isotopic effects of Fe hydration and formation of Cl^- complexes on the individual β-factors of coexisting aqueous species. The effects of higher order Fe-chloro-complexes at elevated P-T conditions, however, have not been critically examined. In addition, INRXS spectral measurements conducted on pyrite are needed to assess the validity of the β-factors for pyrite previously determined through Mössbauer and theoretical methods [*Blanchard et al.*, 2012; *Polyakov and Soultanov*, 2012]. The experimental data reported here provide an independent means of comparison critical to the evaluation of the data and the theoretical and spectral approaches used to acquire them. For example, the equilibrium fractionation data reported from the exchange experiments at 350°C can be used to estimate the Fe force constant of pyrite [*Dauphas et al.*, 2012], assuming the β-factor of $Fe^{2+}_{(aq)}$ from *Rustad et al.* [2010] at 350°C, allowing an extrapolation of the β-factor of pyrite as a function of temperature (see Eq. 13 in

Dauphas et al. [2012]). The estimate of the calculated Fe force constant of pyrite from this experimental study, 283±40 N/m (2σ), is used to provide the regression of the β-factor versus temperature in Fig. 1.6 (shaded region) shown in comparison to β-factors predicted by *Polyakov et al.* [2007] (dotted line) and *Blanchard et al.* [2012] (dashed line). The predicted β-factor from this study is in agreement with the predicted β-factors from *Blanchard et al.* [2012].

1.3.3. Fe isotope systematics during pyrite precipitation experiments

Previous experimental work at elevated conditions (up to 300°C) by *Schoonen and Barnes* [1991] has shown that pyrite forms rapidly in the presence of FeS and thiosulfate. Furthermore, *Ono et al.* [2007] has demonstrated from ^{33}S constraints of S-isotopic exchange and mixing that thiosulfate is an important intermediate between H_2S, SO_4^{2-}, and pyrite during precipitation and subsequent recrystallization in active seafloor chimney environments and the subsurface of these systems where H_2S and Fe-bearing hydrothermal fluids mix with SO_4^{2-} rich seawater. Thus, the precipitation experiments performed as part of the present study can provide clues to the effects of mixing and mineralization on Fe isotope partitioning in natural systems.

The observed increase in $\delta^{56}Fe$ of dissolved Fe relative to the isotopically depleted Fe isotope composition inferred for the first-formed pyrite crystals reasonably resembles the predicted fractionation of FeS-$Fe^{2+}_{(aq)}$, $\Delta^{56}Fe_{FeS\text{-}Fe(aq)}$, from the combination of β-factors from *Polyakov et al.* [2007] (FeS, troilite) and *Rustad et al.* [2010] ($Fe(H_2O)^{2+}$) (Fig. 1.7). In Fig. 1.7, the triangles represent the initial Fe isotope fractionation between pyrite and dissolved Fe, where the 300°C experiment and the

350°C experiments, #1 and #2, are identified by red, purple, and green triangles, respectively. The initial Fe isotopic fractionations, t_i, presented in Fig. 1.7 between pyrite and dissolved Fe^{2+} were calculated by bulk chemical and isotopic mass balance of dissolved Fe^{2+} from data presented in Table 1.5. *Polyakov and Soultanov* [2011] suggest that rapidly precipitated pyrite inherits the Fe isotopic composition of the intermediate phase, mackinawite (FeS), which is isotopically fractionated at equilibrium with respect to dissolved Fe. We substitute the β-factor for mackinawite with a "FeS" phase more representative of the current experimental P-T conditions, such as pyrrhotite [*Delacour et al.*, 2008; *Lennie et al.*, 1995; *Rickard and Luther*, 1997], by assuming similar β-factors with troilite [*Dauphas et al.*, 2012; *Polyakov et al.*, 2007] since the predicted troilite β-factor agrees well with the experimental equilibrium fractionations observed at high temperature between pyrrhotite and silicate melt [*Polyakov et al.*, 2007; *Schuessler et al.*, 2007]. By this interpretation, the apparent disequilibrium Fe isotope composition of pyrite, observed in some natural systems, reflects not kinetic isotope effects, but rather Fe isotope equilibrium involving a metastable intermediary. However, an alternative interpretation can be inferred by fitting the experimental data from the 350°C precipitation experiments to a Rayleigh fractionation model [*Skulan et al.*, 2002], yielding a kinetic isotope fractionation factor, $1000\ln{}^{56}\alpha_{Pyr\text{-}Fe(aq)} \approx \Delta^{56}Fe_{Pyr\text{-}Fe(aq)}$, of -0.29±0.24‰ (2σ). Although there are few data to constrain a model such as this, the magnitude of each initial isotopic fractionation at 350°C between bulk pyrite and dissolved Fe^{2+} correlates with the extent of pyrite precipitation, indicative of a Rayleigh fractionation process. The calculated fractionation factor suggests that the first formed

pyrite would be isotopically light relative to the coeval Fe-bearing hydrothermal fluid and that both phases must progressively become isotopically heavier during precipitation of increasingly greater amounts of pyrite. This latter kinetic mechanism is in accord with inferences from field Fe and S-isotope data of sulfides and hydrothermal fluids [*Rouxel et al.*, 2008], and low temperature FeS formation experiments [*Butler et al.*, 2005; *Guilbaud et al.*, 2011a; *Guilbaud et al.*, 2010; *Guilbaud et al.*, 2011b].

With increasing reaction progress, pyrite recrystallization promotes Fe isotopic exchange during each experiment at 300 and 350°C, as shown by the continued decrease in δ^{56}Fe of the dissolved Fe with time (Table 1.5). This is also shown by the change between the initial and final Fe isotopic fractionation between pyrite and dissolved Fe (Fig. 1.7, squares labeled t_f represent the measured final isotopic fractionation between pyrite and dissolved Fe). The final Fe isotopic fractionation measured for the longest reaction duration (1082 hours) at the highest temperature (350°C #2), indicates a provisional Fe isotopic fractionation between pyrite and dissolved, $\Delta^{56}Fe_{Py\text{-}Fe(aq)}$, of approximately +0.44‰ (square labeled "t_f" #2, Fig. 1.7). Although this value is less than that derived from the pyrite-fluid exchange experiments by approximately 0.55‰, the time series trend moves in the correct direction and is of interest mechanistically. Owing to the uncertain extent of isotope exchange between the precipitated pyrite and the Fe bearing fluid, however, the data cannot be used to determine equilibrium Fe isotopic fractionation effects in the absence of an isotopic tracer to quantify mass transfer processes. Nevertheless, these data in combination with constraints imposed by the isotope exchange experiments provide additional insight on the effect of rates of

mineralization in the Fe-S-H_2O system on Fe isotope fractionation processes. Insights of this sort are highly relevant to unraveling the relative roles of equilibrium and kinetic processes of pyrite and similar sulfide minerals at deep-sea vents at mid-ocean ridges, where mineralization occurs rapidly and in some cases irreversibly owing to the high temperatures and the dramatically different chemistry of seawater and vent fluid. Inferences drawn from Fe isotope data of pyrite from this environment as a means for constraining phase equilibria (chemistry, temperature) must be applied with great caution.

1.4. Conclusion

We report here the first experimental determination of equilibrium Fe isotope fractionation between pyrite and dissolved Fe ($\Delta^{56}Fe_{Pyr\text{-}Fe(aq)}$) at 350°C and 500 bars, yielding a value of 0.99±0.29‰ (2σ). The partial isotope exchange method was used to obtain these experimental data. The experimental strategy benefited from adjusting the isotopic composition and relative mass abundances of Fe in pyrite and the coexisting aqueous fluid. Although the experiments were conducted for more than 3300 hours, data indicate incomplete isotope exchange (~64%). The experimentally determined fractionation factor is in generally good agreement with predictions based on spectral data when these estimates are combined with a common theoretical data source of data for aqueous Fe^{2+}. Concern exists, however, as to the accuracy of the predicted Fe isotope data for aqueous species, considering the chemical complexity of the experimental fluids and the elevated temperatures at which the experiments were performed.

Distribution of aqueous species calculations at experimental conditions not only

confirm pyrite-fluid equilibria, but also effectively preclude existence of any other Fe-bearing mineral, in keeping with analysis of experimental runs products. In addition to the isotope exchange experiments, precipitation experiments were performed at 300 and 350°C, 500 bars. Results of these experiments suggest rapid formation of pyrite and Fe isotope fractionation broadly consistent with crystal growth from FeS intermediaries; however, an alternative model involving kinetic isotope effects cannot be ruled out, in the absence of additional data. Time series observations from the precipitation experiments suggest recrystallization and pyrite crystal growth that continues to fractionate Fe isotopes gradually enriching the mineral in the heavier Fe isotope.

The experimental data can be applied to natural pyrite bearing hydrothermal systems to better constrain reaction processes and conditions of formation. The reported data, however, can also be used to test predictions of Fe isotope fractionation based on Mössbauer spectroscopy and INRXS synchrotron radiation data. On the other hand, results of the precipitation experiments can provide clues to the mechanism of pyrite formation in natural hydrothermal systems, as a consequence of mixing between "endmember" metal-bearing fluids and SO_4^{2-}-rich seawater, and subsequent crystal growth effects. Experiments of the type reported here need to be expanded to include a wider range of minerals, fluids, and chemical systems if progress is to be made with the quantitative interpretation of the rapidly expanding database of non-traditional isotopes in of minerals and fluids in marine and terrestrial hydrothermal systems.

Table 1.1: Reactant (RF1-RF3) and product (Low F/M and High F/M) solution chemistry for the Fe isotope exchange experiments at 350°C, 500 bars.

Solutions	$pH_{25°C}$	$[Fe^{2+}]$	$[Na^{+}]$	$[Cl^{-}]$	$[H_2S]$	$[SO_4^{2-}]$
RF1	2.26	20.1	972	1012	-	-
RF2	2.27	19.3	1007	1046	-	-
RF3	1.29	55.6	1558	1670	-	-
Low F/M #1 (Pyr2-RF1)	2.01	18.4	1056	1123	5.8	6.9
Low F/M #2 (Pyr1-RF2)	2.36	21.1	1011	1090	4.4	5.1
Low F/M #3 (Pyr2-RF2)	2.21	16.1	1020	1099	5.0	6.8
Low F/M #4 (Pyr3-RF2)	1.77	20.3	1007	1072	11.1	10.8
High F/M #1-1 (Pyr2-RF3)	1.23	50.5	1570	1698	18.4	54.2
High F/M #1-2 (Pyr2-RF3)	1.30	51.4	1545	1675	11.8	48.3

Brackets represent total dissolved concentration in mmol/kg. Chemical data from low F/M experiments refer to quench fluids, while the high F/M data represent fluids sampled at elevated temperatures and pressures, and analyzed subsequently.

Table 1.2: Solution chemistry sampled from the pyrite precipitation experiments at 300 and 350°C and 500 bars.

300°C	Time (hours)	$pH_{25°C}$	f(%)	$[Fe^{2+}]$	$[H_2S]$	$[SO_4^{2-}]$	$[Na^+]$	$[Cl^-]$	Solution (grams)
0	-	1.06	100	37.8	0	0	861	1036	43.9
$Na_2S_2O_3$ inj.	0.0	6.67		0	-	-	1992		3.9*
1	0.8	1.16	35.8	13.6	16.8	67	947	969	43.7
2	56	1.1	28.1	11.9	16.1	70	963	983	39.0
3	68	1.1	22.0	11.6	16.5	67	935	958	31.4
Final Pyrite	68	-	-	-	-	-			-
350°C #1	Time (hours)	$pH_{25°C}$	f(%)	$[Fe^{2+}]$	$[H_2S]$	$[SO_4^{2-}]$	$[Na^+]$	$[Cl^-]$	Solution (grams)
0	-	1.05	100	36.9	0	0	870	1030	44.1
$Na_2S_2O_3$ inj.	0.0	6.67		0	-	-	1992		5.7*
1	0.3	1.22	23.7	8.8	21.8	86	966	942	46.8
2	332	1.14	20.4	8.0	18.0	87	956	950	40.9
3	398	1.17	17.7	7.8	23.4	87	958	951	35.2
Final Pyrite	398	-	-	-	-	-			-
350°C #2	Time (hours)	$pH_{25°C}$	f(%)	$[Fe^{2+}]$	$[H_2S]$	$[SO_4^{2-}]$	$[Na^+]$	$[Cl^-]$	Solution (grams)
0	-	1.06	100	38.5	0	0	863	1033	53.9
$Na_2S_2O_3$ inj.	0.0	6.67			-	-	1992		5.9*
1	0.6	1.13	5.2	2.0	n.a.	101	994	924	52.7
2	720	1.08	4.1	1.7	30.7	98	1009	928	48.5
3	1082	1.15	4.4	2.1	33.2	101	1002	943	43.9
Final Pyrite	1082	-	-	-	-	-			-

*Amount (grams) of ~1 mol/kg $Na_2S_2O_3$ solution injected into the gold cell. Brackets represent total dissolved concentration in mmol/kg. The percent of dissolved Fe remaining, f, after precipitation is derived from Fe mass balance of the sampled solution chemistry (see text). Not analyzed (n.a.).

Table 1.3: Fe isotopic composition, $\delta^{56}Fe$ and $\delta^{57}Fe$, of the initial reactant $FeCl_2$ solutions (RF1-RF3) and pyrite (Pyr1-Pyr3) for the exchange experiments.

Solutions and Pyrite	$\delta^{56}Fe \pm 2\sigma$ (‰)	$\delta^{57}Fe \pm 2\sigma$ (‰)	n
RF1	-0.354 ± 0.078	-0.486 ± 0.274	5
RF2	-0.405 ± 0.069	-0.654 ± 0.124	3
RF3	0.246 ± 0.095	0.399 ± 0.304	3
Pyr1	0.273 ± 0.065	0.482 ± 0.245	3
Pyr2	-0.018 ± 0.072	0.001 ± 0.228	3
Pyr3	-0.075 ± 0.033	-0.117 ± 0.168	2
Solution Low F/M #1	-0.842 ± 0.084	-1.220 ± 0.441	2
Solution Low F/M #2	-0.522 ± 0.101	-0.708 ± 0.117	2
Solution Low F/M #3	-0.903 ± 0.031	-1.306 ± 0.037	3
Solution Low F/M #4	-0.731 ± 0.151	-0.956 ± 0.055	2
Solution High F/M #1-1	-0.188 ± 0.070	-0.350 ± 0.009	2
Solution High F/M #1-2	-0.153 ± 0.052	-0.257 ± 0.301	3
Pyr3R-HighF/M	0.331 ± 0.311	0.584 ± 0.319	2

The Fe isotopic composition of sampled and final product $FeCl_2$ solutions of each experiment and pyrite for the High F/M experiment is also shown in the lower portion of the table. The High F/M experiment includes two samples, #1-1 and #1-2, that represent the initial and final solution of the experiment, respectively.

Table 1.4: The initial, final, and the relative change of the Fe isotopic fractionation, $\Delta^{56}Fe$, between pyrite and dissolved Fe for each exchange experiment.

Exchange Experiment	Starting Assemblage	$XFe_{(Pyr)}$ (%)	$\Delta^{56}Fe_{Initial} \pm 2\sigma$ (‰)	$\Delta^{56}Fe_{Final} \pm 2\sigma$ (‰)	$\Delta^{56}Fe_{Final-Initial} \pm 2\sigma$ (‰)
Low F/M#1	Pyr2-RF1	97.1	0.34 ± 0.11	0.82 ± 0.11	0.49 ± 0.16
Low F/M #2	Pyr1-RF2	97.2	0.68 ± 0.09	0.80 ± 0.12	0.12 ± 0.15
Low F/M #3	Pyr2-RF2	97.1	0.39 ± 0.10	0.89 ± 0.08	0.50 ± 0.13
Low F/M #4	Pyr3-RF2	97.2	0.33 ± 0.08	0.66 ± 0.15	0.33 ± 0.17
High F/M #1-2	Pyr3-RF3	22.0	-0.26 ± 0.12	0.49 ± 0.09	0.75 ± 0.15
Least Squares Fit Y-intercept:	$\Delta^{56}Fe(Equil.) \pm 2\sigma$ (‰)	0.99 ± 0.29	Slope:	-1.56 ± 0.60	

Results of least squares fit of the initial Fe isotopic fractionation versus the relative change in Fe isotopic fractionation between pyrite and dissolved Fe is shown in the bottom row of the table. The regressed data indicate that the equilibrium Fe isotopic fractionation between pyrite and dissolved Fe, $\Delta^{56}Fe_{(Equil.)}$, is 0.99 ± 0.29‰, and the extent of exchange, as indicated by the inverse of the slope, is ~64%. The Fe isotopic fractionation and the linear regression reported are plotted in Fig 1.4.

Table 1.5: Fe isotope composition ($\delta^{56}Fe$ and $\delta^{57}Fe$) of the initial $FeCl_2$ solutions (sample "0"), $FeCl_2$ solutions after pyrite precipitation ("1-3"), and final pyrite.

300°C	Time (hours)	*f*(%)	$[Fe^{2+}]$	$\delta^{56}Fe \pm 2\sigma$ (‰)	$\delta^{57}Fe \pm 2\sigma$ (‰)
0	-	100	37.8	-0.391 ± 0.199	-0.716 ± 0.381
1	0.8	35.8	13.6	0.047 ± 0.209	0.152 ± 0.163
2	56	28.1	11.9	-0.145 ± 0.107	-0.197 ± 0.226
3	68	22.0	11.6	-0.328 ± 0.073	-0.444 ± 0.284
Final Pyrite	68	-	-	-0.611 ± 0.154	-0.934 ± 0.226
350°C #1	Time (hours)	f(%)	$[Fe^{2+}]$	$\delta^{56}Fe \pm 2\sigma$ (‰)	$\delta^{57}Fe \pm 2\sigma$ (‰)
0	-	100	36.9	-0.323 ± 0.154	-0.430 ± 0.226
1	0.3	23.7	8.8	-0.181 ± 0.262	-0.236 ± 0.023
2	332	20.4	8.0	-0.432 ± 0.097	-0.461 ± 0.226
3	398	17.7	7.8	-0.592 ± 0.241	-0.930 ± 0.178
Final Pyrite	398	-	-	-0.451 ± 0.127	-0.803 ± 0.185
350°C #2	Time (hours)	f(%)	$[Fe^{2+}]$	$\delta^{56}Fe \pm 2\sigma$ (‰)	$\delta^{57}Fe \pm 2\sigma$ (‰)
0	-	100	38.5	-0.578 ± 0.198	-0.720 ± 0.362
1	0.6	5.2	2.0	0.272 ± 0.029	0.296 ± 0.067
2	720	4.1	1.7	-0.770 ± 0.033	-1.168 ± 0.033
3	1082	4.4	2.1	-0.784 ± 0.015	-1.292 ± 0.061
Final Pyrite	1082	-	-	-0.348 ± 0.025	-0.638 ± 0.084

Total dissolved Fe concentrations are in mmol/kg. The fraction of dissolved Fe remaining, *f*, after the precipitation event (sample "1") versus the observed initial Fe isotopic fractionation for each 350°C experiment is used to regress a kinetic Fe isotopic fractionation factor using a Rayleigh model (see text). Calculated initial and the measured final Fe isotopic fractionation between pyrite and dissolved Fe at 300 and 350°C for all precipitation experiments are plotted in Fig. 1.7.

Figure 1.1

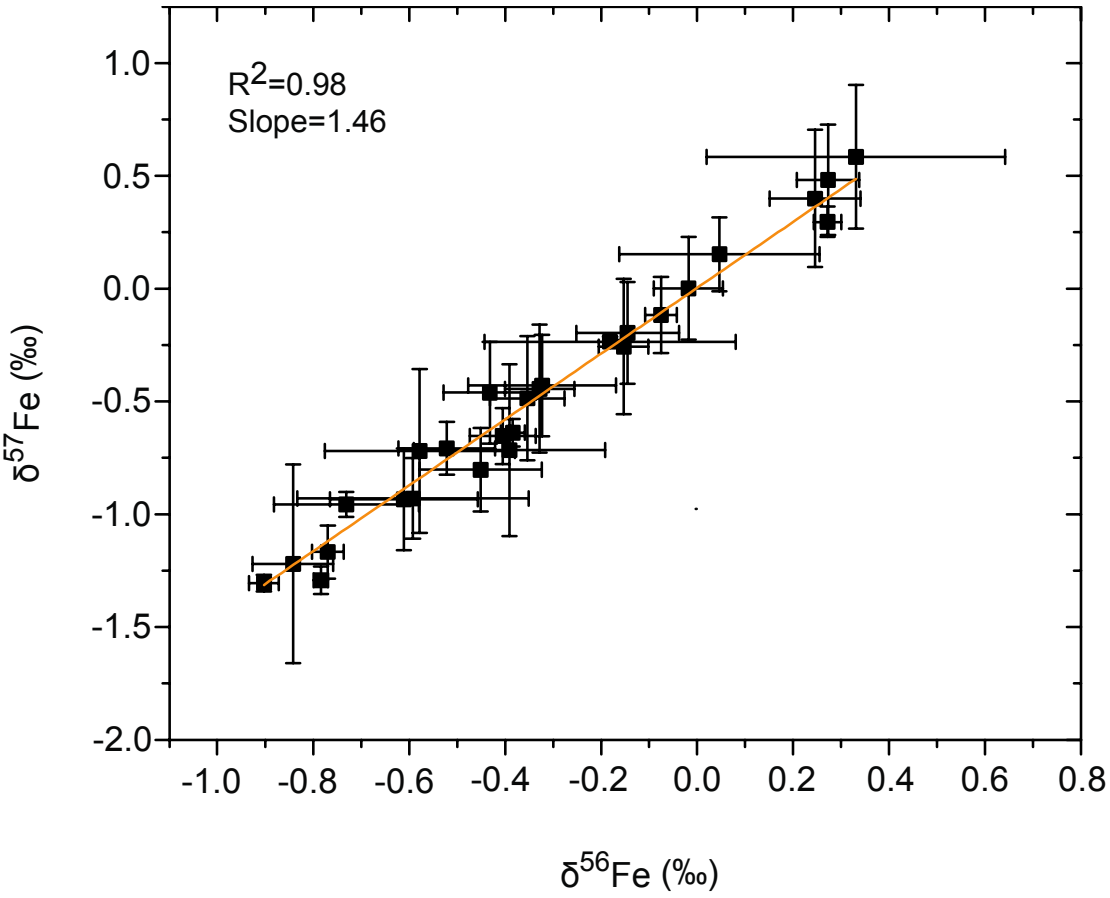

Fig. 1.1 Plot of $\delta^{57}Fe$ versus $\delta^{56}Fe$ for the Fe isotopic data shown in this study ($FeCl_2$ solutions and pyrite). Error bars show 2σ error from at least two or more individual mass spectrometric analyses. All Fe isotopic data are reported in Tables 3 and 5 in main text.

Figure 1.2

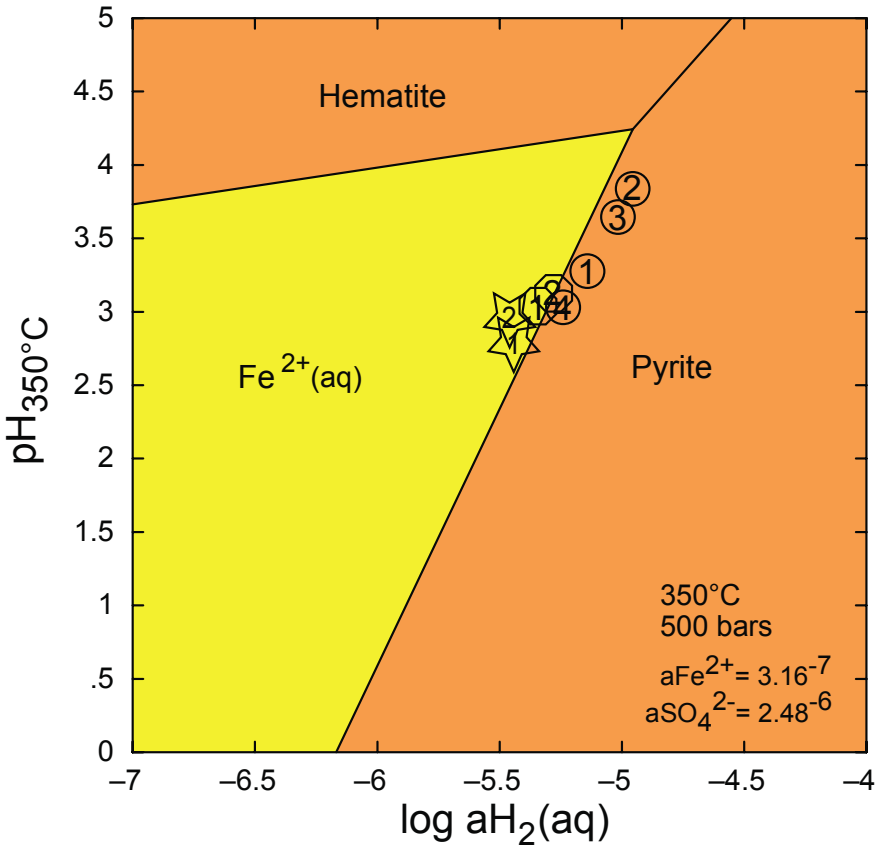

Fig. 1.2 $pH_{350°C}$ versus log $aH_{2(aq)}$ diagram delineating the phase boundaries between aqueous Fe^{2+} and Fe-bearing minerals, pyrite and hematite at 350°C, 500 bars. The symbols on the diagram depict data from the present experiments (circles #1-4 represent results from the low F/M ratio experiments, stars #1-2 represent the two solutions sampled from high F/M ratio experiment, while octagons #1-2 indicate the final solution from the two pyrite precipitation experiments at 350°C). The activity of $H_{2(aq)}$ was calculated from the dissolved concentrations of SO_4^{2-} and H_2S following speciation at experimental conditions (see text). All of the data plot on/near the pyrite-dissolved Fe^{2+} join in keeping with pyrite-fluid equilibria. Minerals other than pyrite were not observed by SEM examination following the experiments, consistent with phase equilibria calculations.

Figure 1.3

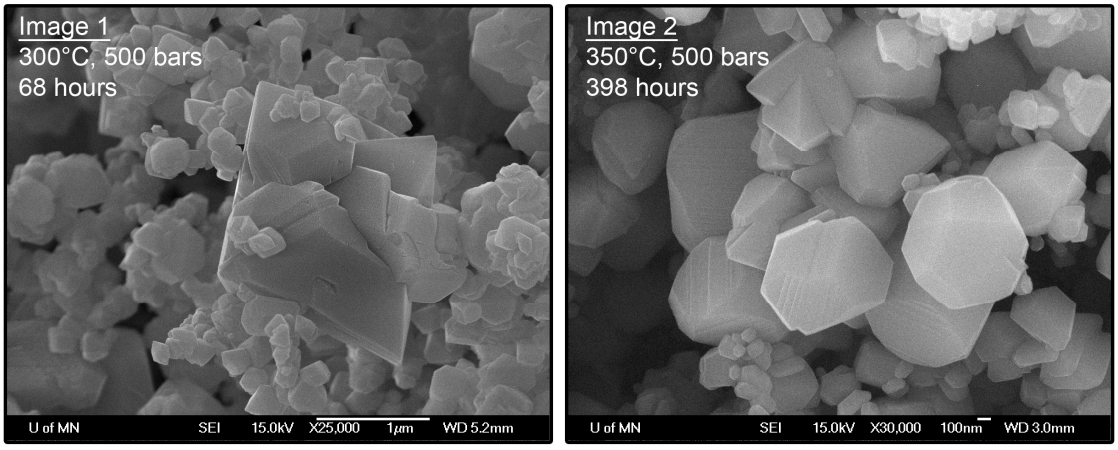

Fig. 1.3 SEM images of pyrite from hydrothermal precipitation experiments at 300 and 350°C, 500 bars. Image #1 shows pyrite precipitated from a $FeCl_2$ solution at 300°C and 500 bars upon injection of a $Na_2S_2O_3$ solution. The scale is shown on the bottom right of each image as a white bar. The pyrite crystals exhibit a transitional morphology towards the common pyrite habit form, o{111}, which is commonly found when formed from FeS reactants [*Graham and Ohmoto*, 1994]. Note the high degree of heterogeneity in grain size during the relatively short reaction interval (68 hours). Image #2 shows pyrite, formed from rapid precipitation, after 398 hours of recrystallization in the presence of a $FeCl_2$ and sulfur-bearing solution at 350°C and 500 bars. The crystal morphology of the pyrite shown is indicative of fast recrystallization rates due to the high temperature, Fe and S rich fluid, and the large degree of initial surface area heterogeneity.

Figure 1.4

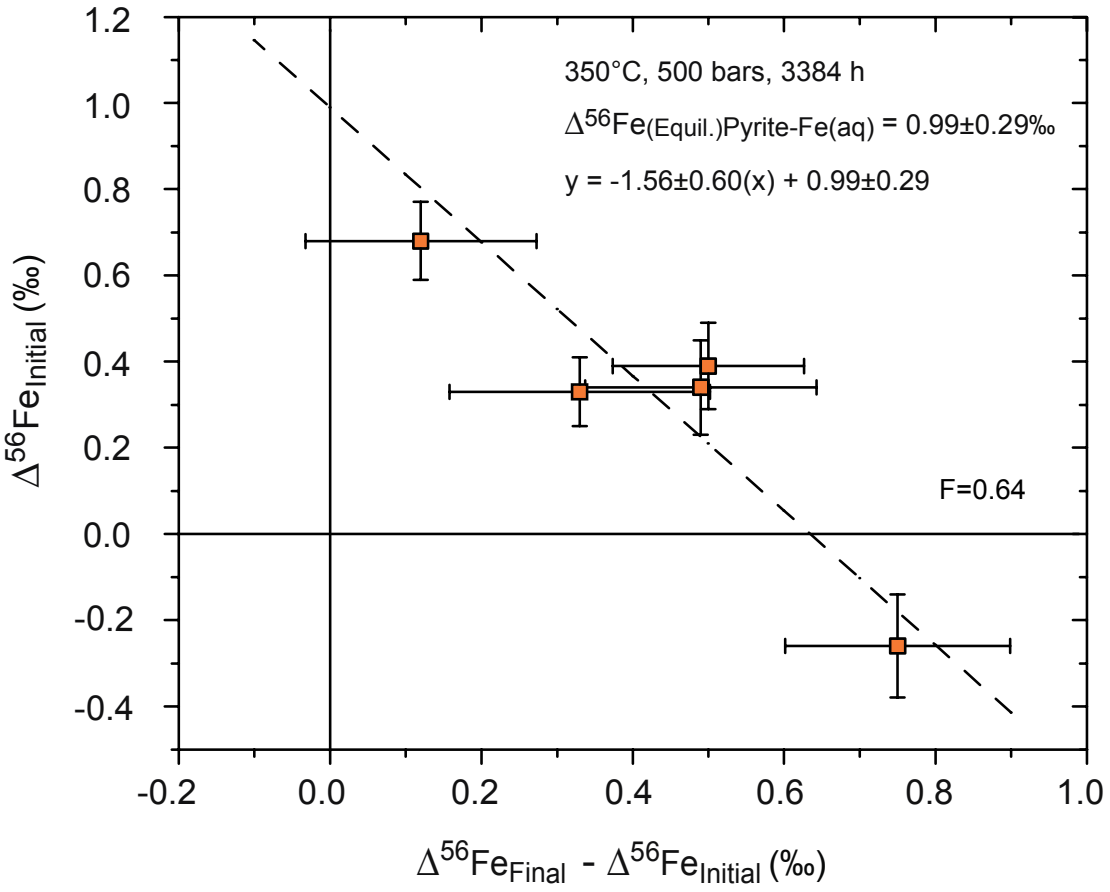

Fig. 1.4 Data from Table 4 that illustrate Fe isotope exchange between pyrite and dissolved Fe at 350°C, 500 bars, and 3384 hours of reaction for each of the designated experiments (see text). The data were obtained by plotting the initial Fe difference in the Fe isotopic composition between the two phases ($\Delta^{56}Fe_{Initial}$) relative to the change in the Fe isotopic composition between the phases after the reaction interval ($\Delta^{56}Fe_{Final}$ - $\Delta^{56}Fe_{Initial}$). The y-intercept determined from bivariate linear regression of the Fe isotopic data indicates that the extrapolated equilibrium Fe isotope fractionation factor between pyrite and dissolved Fe, $\Delta^{56}Fe_{Pyr\text{-}Fe(aq)}$, is 0.99±0.29. The slope, F^{-1}, of the linear regression provides an estimate on the degree of exchange, 64%, between pyrite and dissolved Fe over the course of the 3384 hour experiment. The linear relationship exhibited by the Fe isotopic data is consistent with constraints imposed by the partial exchange technique, model assumptions, and the experimental strategy implemented.

Figure 1.5

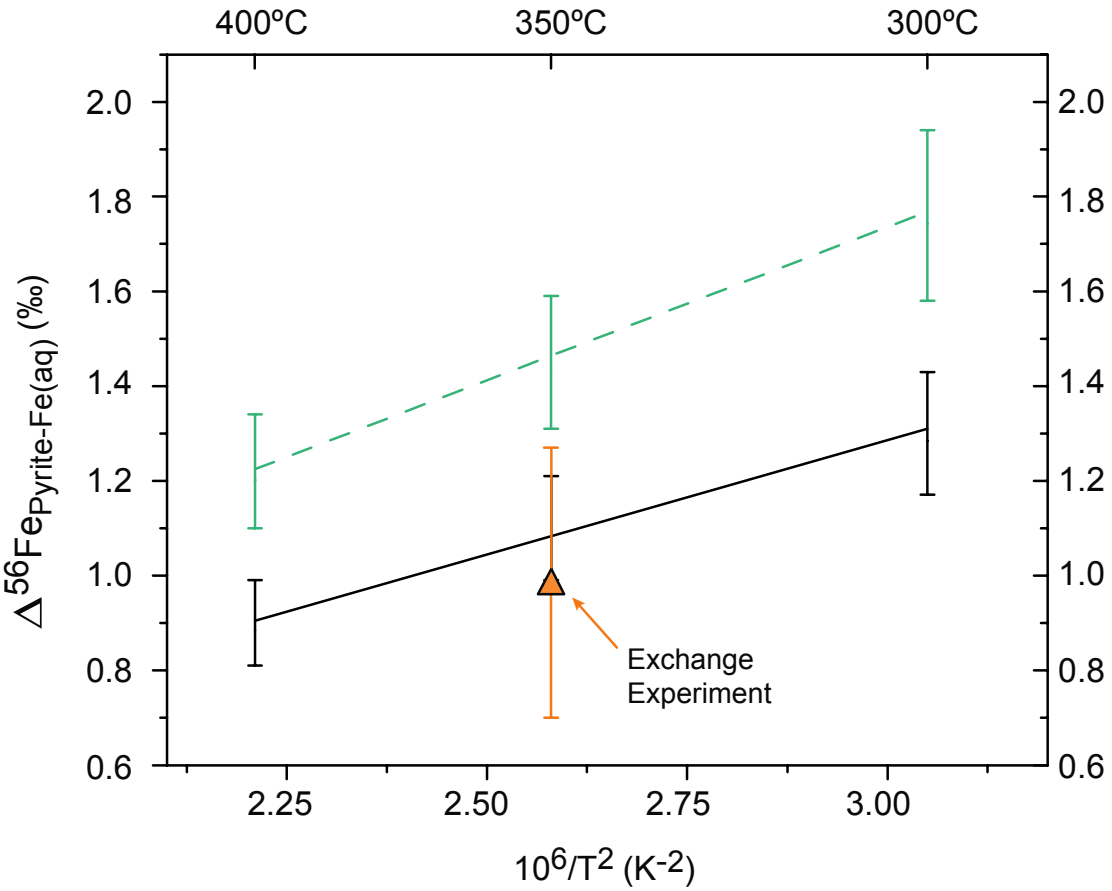

Fig. 1.5 Experimentally determined equilibrium Fe isotope fractionation between pyrite and dissolved Fe at 350°C and 500 bars ($\Delta^{56}Fe_{Pyrite\text{-}Fe(aq)}$, 0.99±0.29‰, triangle) in comparison with theoretical predictions. The predicted fractionations were calculated from $Fe(H_2O)^{2+}$ β-factor of *Rustad et al.* [2010] and β-factors for pyrite from *Blanchard et al.* [2012] and *Polyakov and Soultanov* [2011] (see text). The β-factor for the aqueous Fe^{2+} species reported by *Rustad et al.* [2010] is essentially identical to analogous data at 350°C reported by *Polyakov and Soultanov* [2011]. The predicted equilibrium Fe isotopic fractionation between pyrite and dissolved Fe from *Blanchard et al.* [2012] and *Rustad et al.* [2010] data is represented by the black solid line whereas the alternative data for pyrite from *Polyakov and Soultanov* [2011] when combined with the *Rustad et al.* [2010] data is represented by the dashed line. In general, data from the present experiment tend to correlate better with the latter source, although in light of uncertainties in Fe isotope fractionation effects imposed on Fe-bearing aqueous species by composition and temperature, comparisons of this sort are very preliminary. All error bars shown for the predicted fractionations between pyrite and dissolved Fe represent 10% of the predicted fractionations.

Figure 1.6

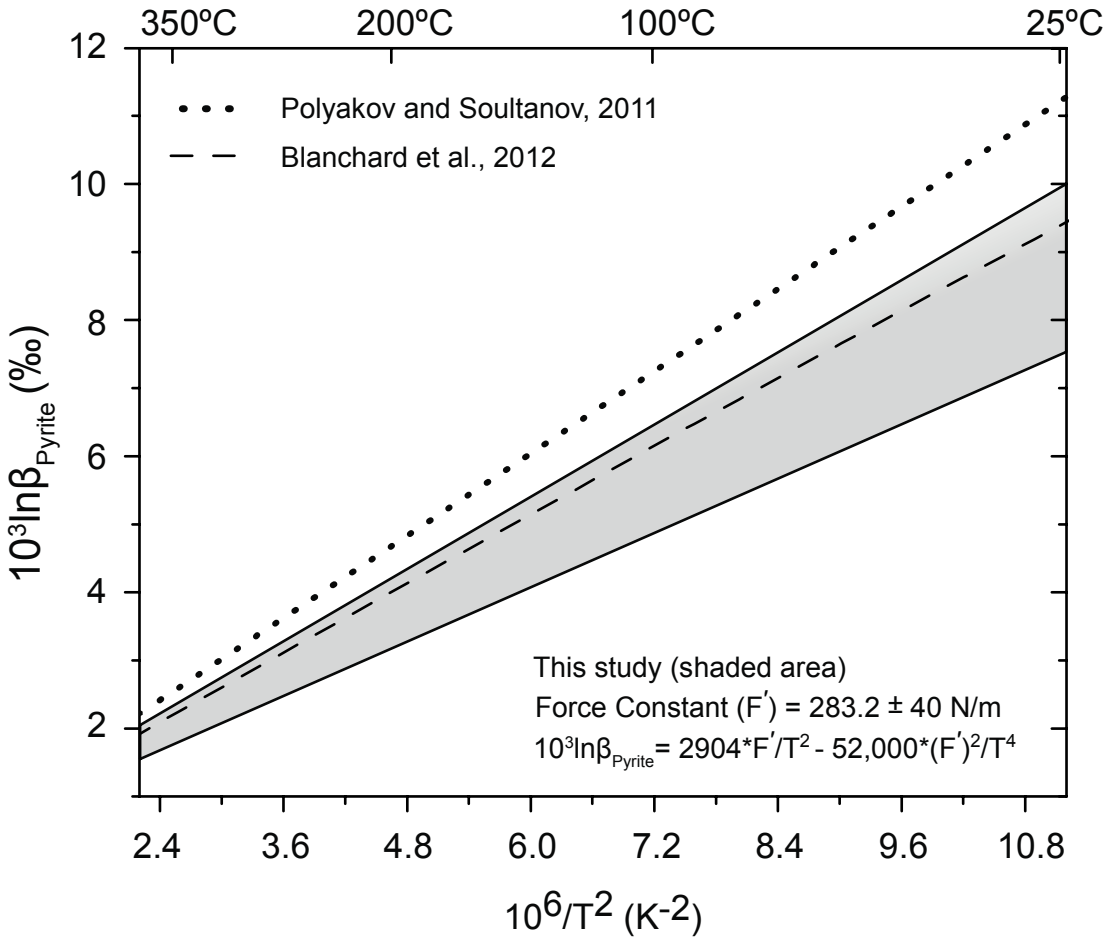

Fig. 1.6 Comparison of extrapolated β-factors as a function of temperature estimated from Mössbauer measurements ([*Polyakov and Soultanov*, 2011], dotted line), DFT calculations ([*Blanchard et al.*, 2012], dashed line), and the experimentally determined equilibrium fractionation between pyrite and dissolved Fe^{2+} from this study (shaded region, 2σ uncertainty). The shaded region represents the predicted $10^3 \ln\beta$ from the estimated Fe force constant [*Dauphas et al.*, 2012] determined from this study by using the β-factor for $Fe^{2+}_{(aq)}$ from *Rustad et al.* [2010]. The β-factor can be extrapolated versus temperature by using the estimated Fe force constant and the equation presented in the figure (Eqs. 13 in *Dauphas et al.* [2012]). The predicted pyrite β-factors from this study agrees well with the estimated β-factors from *Blanchard et al.* [2012].

Figure 1.7

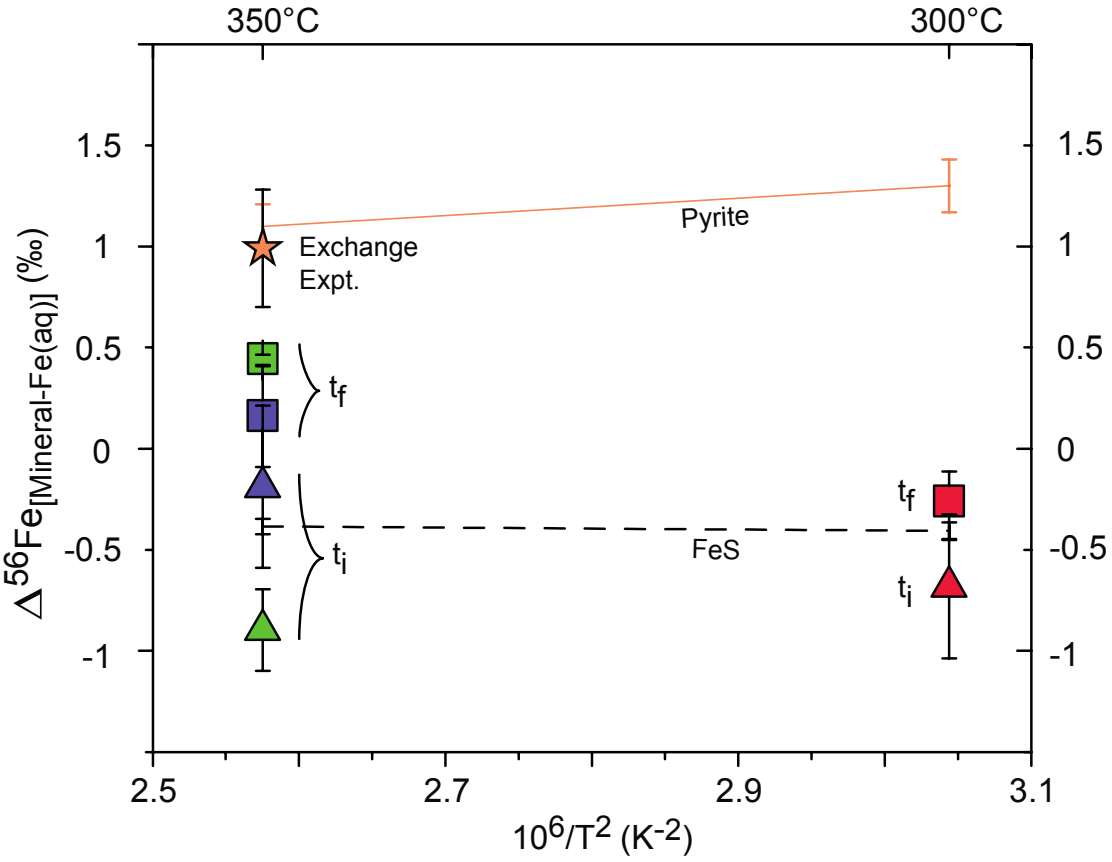

Fig. 1.7 Mineral(sulfide)-fluid Fe isotope fractionation ($\Delta^{56}Fe_{Mineral\text{-}Fe2+(aq)}$) versus temperature for pyrite [*Blanchard et al.*, 2012] and FeS [*Polyakov et al.*, 2007] in comparison with results from precipitation experiments (this study) . The β-factor for the $Fe(H_2O)^{2+}$ aqueous complex used for the predicted mineral-fluid equilibrium Fe isotopic fractionation with the Fe-bearing sulfides are from *Rustad et al.* [2010]. The initial Fe isotope fractionation during pyrite precipitation, calculated by mass balance, at 300°C (red symbols) and 350°C (Expt. #1 and Expt. #2 designated as purple and green, respectively) are designated by triangles, and labeled "t_i". As time proceeds for each experiment at both temperatures, the recrystallization of pyrite promotes Fe isotopic exchange, creating a transitional Fe isotopic fractionation between pyrite and dissolved Fe, labeled as squares and designated "t_f", trending towards the equilibrium fractionation. At 350°C, the time series data suggest early stage depletion in the heavy isotope of Fe, which ultimately trends towards the experimentally determined equilibrium exchange Fe isotopic fractionation determined for pyrite-fluid (orange star labeled "Exchange Expt."). Fe isotope data at 300°C behave similarly to the 350°C data. These data can be interpreted as a kinetic process where the incipient formation of pyrite may originate from FeS reactants. In addition, the relationship in the initial Fe isotopic fractionation for each experiment at 350°C as a function of *f*, the degree of $Fe^{2+}_{(aq)}$ remaining in solution (Table 5), suggests that a Rayleigh process may control the observed fractionations, possibly with Fe as the reactive component during the formation of pyrite.

Chapter 2

Multiple Sulfur Isotope Fractionation and Mass Transfer Processes during Pyrite Precipitation and Recrystallization: An Experimental Study at 300 and 350°C

Drew D. Syverson [a], Shuhei Ono [b], Wayne C. Shanks, III [c], William E. Seyfried, Jr [a].

[a] *Department of Earth Sciences, University of Minnesota*
310 Pillsbury Drive, S.E., Minneapolis, Minnesota 55455-0231

[b] *Department of Earth, Atmospheric, and Planetary Sciences, Massachusetts Institute of Technology, 77 Massachusetts Avenue, Cambridge, Massachusetts 02139-4307*

[c] *U.S. Geological Survey, 937 Denver Federal Center, Denver, Colorado 80255*

Published in *Geochimica et Cosmochimica Acta,* vol. 165 (2015), pp. 418-434

Used with permission of the co-authors and by Elsevier Publishing

2.0. Summary

Equilibrium multiple sulfur isotope fractionation factors ($^{33}S/^{32}S$ and $^{34}S/^{32}S$) between aqueous SO_4, H_2S, and coexisting pyrite under hydrothermal conditions were determined experimentally at 300-350°C and 500 bars. Two different experimental techniques were used to determine the fractionation factors and the rate of S isotope exchange between pyrite and constituent aqueous species, H_2S and SO_4; (1) closed system gold capsule pyrite−H_2S exchange experiments and (2) complimentary time-series experiments at 300 and 350°C, 500 bars using flexible gold cell hydrothermal equipment, which allowed monitoring the multiple S isotope composition of dissolved S

species during pyrite precipitation and subsequent recrystallization. The three isotope technique was applied to the multiple S isotope data to demonstrate equilibrium S isotope fractionation between pyrite and H_2S. Results at 350°C indicate $ln^{34}\alpha_{Pyrite/H2S}$ = -1.9‰ and $ln^{33}\alpha_{Pyrite/H2S}$ = -1.0‰. The $ln^{34}\alpha_{Pyrite/H2S}$ is not only different in magnitude but also in sign from the commonly used value of 1‰ from *Ohmoto and Rye* [1979]. This experimental study also demonstrated initial S isotope disequilibrium amongst the aqueous S-species and pyrite during rapid precipitation, despite aqueous speciation indicating pyrite saturation at all stages. Textural, crystallographic, and S isotope interpretations suggest that pyrite formed by means of the FeS pathway. The initial S isotope disequilibrium between formed pyrite and dissolved S-species was effectively erased and approached isotopic equilibrium upon recrystallization during the course of 4297 hours. Interpretation of seafloor hydrothermal vent sulfides using the revised equilibrium $^{34}S/^{32}S$ fractionation between pyrite and H_2S suggests that pyrite is close to S isotope equilibrium with vent H_2S, contrary to previous conclusions. The experimental data reported here broaden the range of pyrite formation mechanisms at seafloor hydrothermal vents, in that mineral formation pathway and equilibration rates need to be considered to account for the well-recognized S isotope variability that often characterizes these systems.

2.1. Introduction

Multiple sulfur isotope studies (^{32}S, ^{33}S, ^{34}S, ^{36}S) have provided important insight on a wide range of geochemical processes linked to the Earth's S-cycle throughout geological time [*Farquhar and Wing*, 2003; *Jamieson et al.*, 2013; *Ono et al.*, 2006; *Ono*

et al., 2003; *Penniston-Dorland et al.*, 2012]. In particular, it has been recognized that different mass dependent fractionation processes follow measurably different fractionation laws, providing an effective means to better differentiate between microbial and inorganically controlled processes [*Farquhar et al.*, 2003; *Johnston et al.*, 2005; *Ono et al.*, 2007; *Sim et al.*, 2011; *Young et al.*, 2002]. Understanding hydrothermal processes via S isotopes requires experimentally and theoretically determined $^{33}S/^{32}S$ and $^{34}S/^{32}S$ equilibrium fractionation factors (α^{33} and α^{34}). Previous studies utilizing traditional $^{34}S/^{32}S$ as well as multiple isotope systematics using ^{32}S, ^{33}S, and ^{34}S[1] have demonstrated signatures of isotopic disequilibrium versus equilibrium, providing unique information on the extent of seawater entrainment into high temperature reaction zones, residence time of hydrothermal fluids, and the role of seawater sulfate/anhydrite buffering on the eventual S isotope composition of dissolved H_2S in vent fluids and sulfide minerals in chimney deposits on the seafloor [*Bluth and Ohmoto*, 1988; *Kerridge et al.*, 1983; *McDermott et al.*, 2015; *Ono et al.*, 2007; *Ono et al.*, 2012; *Peters et al.*, 2011; *Peters et al.*, 2010; *Shanks and Seyfried*, 1987; *Woodruff and Shanks*, 1988]. However, a complete interpretation of S isotope systematics of hydrothermal systems cannot be obtained without further examination of requisite experimental and theoretical data.

Equilibrium fractionation factors provide a thermodynamic framework to interpret S isotope systematics for hydrothermal fluids and coexisting minerals at mid-ocean ridge (MOR), back-arc, and arc environments. *Ohmoto and Rye* [1979] determined S isotope fractionation factors consistent with available experimental, theoretical, and empirical data [*Czamanske and Rye*, 1974; *Grootenboer and Schwarcz*, 1969; *Kajiwara and*

[1] $\Delta^{33}S = \delta^{33}S - \theta_{Ref} \bullet \delta^{34}S$, where θ_{Ref} is equivalent to 0.515 and $\delta^{y}S = \left[\frac{R^{y/32}}{R^{y/32}_{VCDT}} - 1\right]$ (‰), where y = 33 or 34

Krouse, 1971; *Kajiwara et al.*, 1969; *Kiyosu*, 1973; *Nakai*, 1970; *Price and Shieh*, 1979; *Robinson*, 1973; *Salomons*, 1971; *Smith et al.*, 1977]. The fractionation factors tabulated by *Ohmoto and Rye* [1979] have been widely used with little modification for several decades and are warranted to be tested experimentally with multiple S isotope systematics.

Recent advances in spectroscopic measurements and theoretical predictions [*Blanchard et al.*, 2009; *Dauphas et al.*, 2012; *Polyakov and Soultanov*, 2011; *Polyakov et al.*, 2007] have been used to calibrate $^{34}S/^{32}S$ fractionation between sulfide minerals (e.g. pyrite vs. sphalerite) and are in agreement with the generally accepted values in *Ohmoto and Rye* [1979]. However, theoretical and spectroscopic-based fractionation between minerals and aqueous species (e.g. pyite−H_2S), rather than mineral−mineral or fluid−fluid species, have often produced questionable results as a consequence of the different techniques and assumptions required for modeling each solid/fluid phase of interest [*Balan et al.*, 2009; *Beard et al.*, 2010; *Blanchard et al.*, 2012; *Blanchard et al.*, 2014; *Rustad et al.*, 2010].

Sakai [1968] calculated equilibrium $^{34}S/^{32}S$ fractionation factors for aqueous SO_4 and H_2S from first principles using measured or estimated vibrational frequencies with isotope fractionation theory [*Bigeleisen and Mayer*, 1947; *Sakai*, 1968; *Urey*, 1947]. In some cases theoretical isotope fractionation factors between aqueous S-species are calibrated experimentally at temperatures (typically 200-400°C) where exchange rates are fast enough for laboratory equilibration [*Ohmoto and Lasaga*, 1982]. In addition, recent theoretical calculations for triple (or quadruple) isotope systems for gaseous and aqueous

S-species have shown that $^{33}S/^{32}S$ and $^{36}S/^{32}S$ fractionation estimates vary significantly depending on the theoretical models employed [*Otake et al.*, 2008].

The above issues underscore the need for experimental data to ground truth past observations and test the theoretically based equilibrium fractionation factors at conditions relevant to natural mineral−fluid systems at elevated temperatures and pressures. Equilibrium multiple S isotope fractionation factors for sulfide mineral−aqueous sulfide/sulfate pairs, however, have not been examined experimentally until now. Thus, hydrothermal experiments at 300 and 350°C, 500 bars were carried out to assess the fractionation of multiple S isotopes between dominant S-bearing aqueous species in the H_2S-SO_4-NaCl-$FeCl_2$-HCl-H_2O system coexisting with pyrite. In the present experimental study, we apply the three isotope approach initially developed by *Matsuhisa et al.* [1978] for oxygen isotope fractionation (^{16}O, ^{17}O, ^{18}O). In our experiments, the approach to isotope equilibrium is monitored by mass-dependent relationships amongst the ^{32}S, ^{33}S, ^{34}S isotope system. Complimentary long-term $\delta^{34}S-\Delta^{33}S$ exchange and pyrite precipitation experiments are carried out using a range of natural S isotope compositions. The coupling of the exchange experiments with the time-series precipitation experiments allows improved determination of the direction and magnitude of isotope exchange between pyrite and aqueous S-species.

Pyrite is ubiquitous in both marine and terrestrial hydrothermal systems and its precipitation mechanisms have been studied and debated extensively [*Berner*, 1970; *Butler et al.*, 2004; *Guilbaud et al.*, 2011a; *Guilbaud et al.*, 2010; *Guilbaud et al.*, 2011b; *Luther*, 1991; *Murowchick and Barnes*, 1987; *Rickard and Luther*, 1997; 2007; *Schoonen and Barnes*, 1991; *Syverson et al.*, 2013; *Yücel et al.*, 2011]. However, the potential role

of pyrite in catalyzing or inhibiting isotope exchange amongst aqueous S-species during precipitation and recrystallization has not been studied. Additionally, irreversible processes, such as the rapid precipitation of pyrite, may contribute to anomalous (non-zero) $\Delta^{33}S$ values in coexisting mineral−fluid S-reservoirs by a combination of isotope mixing and fractionation [*Ono et al.*, 2006]. Thus, the experimental data may provide insight on the effect of temperature dependent mass transfer reactions involving S isotopes throughout the evolution of mineralization at hydrothermal systems. The two different experimental strategies employed in this study, static (exchange) and dynamic (precipitation), are necessary to resolve these questions.

2.2. Experimental Methods

2.2.1. Pyrite–H_2S S isotope exchange experiments

Pyrite–H_2S exchange experiments were conducted by reacting natural or synthetic pyrite crystals with H_2S; H_2S is derived from the partial dissolution of pyrite and total hydrolysis of native sulfur starting material. The exchange experiments were carried out in sealed gold capsules, which in turn were placed in a steel pressure vessel. Each gold capsule (0.25 cm outer diameter, 0.20 mm wall thickness, 10 cm length, 4 ml internal volume) was loaded with pyrite (~0.2 g), native sulfur (5 to 6 mg), and solution (~2 g) and welded shut. The sealed capsules and water-filled steel pressure vessel were pressurized to 500 bars and heated isobarically to 350°C. Each capsule was reacted for a total of 3384 hours, quenched to less than 150°C within approximately five minutes, and analyzed subsequently after cooling to room temperature within 30 minutes. The reactant pyrite crystals (Pyr1–Pyr3) were derived from multiple sources, as described in *Syverson*

et al. [2013]. Briefly, Pyr1 is synthesized hydrothermally by sulfidation of hematite by native sulfur, Pyr2 is synthesized and acquired from Nano-Corps^{TM}, and Pyr3 is naturally derived. All three types of pyrite crystals are well crystallized, moderately sized (less than 50 μm), and free of other phases as indicated by scanning electron microscopy (SEM) and X-ray diffraction (XRD). The reactant native sulfur undergoes rapid hydrolysis at temperatures greater than 200°C, yielding H_2S and HSO_4^- in a 3:1 ratio, respectively [*Ellis and Giggenbach*, 1971; *Oana and Ishikawa*, 1966; *Robinson*, 1973], as follows:

$$4S^0 + 4H_2O \rightarrow 3H_2S + HSO_4^- + H^+ \qquad (2.1)$$

Sulfur hydrolysis results in low pH and elevated concentrations of H_2S and SO_4, which ensures the chemical system remains in the pyrite stability field. The low initial S^0/H_2O ratios allow the system to be undersaturated with respect to native sulfur in a 1 mol/kg NaCl solution at 350°C and 500 bars. In addition to NaCl concentration, the solutions used in the experiments contain approximately 20 mmol/kg Fe^{2+} and had an initial $pH_{25°C}$ of approximately 2.3 (Table 2.1). In effect, the chemical composition of the fluid was adjusted to be near pyrite saturation at experimental conditions, but far removed from isotopic equilibrium between the mineral and fluid reservoirs, thereby enhancing the driving force for isotopic exchange. Sulfur derived from pyrite comprised approximately 99% of the total S in the mineral−fluid system. Therefore, the S isotope composition of H_2S is particularly sensitive to isotopic exchange during the recrystallization of pyrite.

2.2.2. Pyrite precipitation experiments

The pyrite precipitation experiments were performed using flexible gold reaction cell technology [*Seyfried et al.*, 1987]. This hydrothermal equipment allows fluid to be

added to an on-going experiment, unambiguously establishing "time zero" for the start of a specific chemical reaction, in this case pyrite precipitation. Similarly, fluid can be removed from the reaction cell in the course of an experiment, providing *in-situ* fluid samples at operational P-T conditions. Thus, heat-up and quench effects involving mineral and fluid components are minimized. In addition, the experimental solution is only exposed to inert chemical components during the course of each experiment, maintaining the integrity of the chemical and isotopic composition of sampled solutions. Further details of the flexible gold cell reactor system and of modifications are provided by *Syverson et al.* [2013].

The starting solution for the pyrite precipitation experiments (Table 2.2) was an acidified $FeCl_2$ (37-59 mmol/kg) - NaCl solution (1000 mmol/kg), which was loaded to a N_2 purged gold reaction cell (78 cm^3). The deformable gold reaction cell and supporting on-line sampling equipment were installed in a steel pressure vessel then pressurized to 500 bars and heated, isobarically, either to 300 or 350°C. Pyrite precipitation was initiated in response to the addition of approximately 4 to 7 grams of a Na-thiosulfate ($Na_2S_2O_3$) (1000 mmol/kg) solution, corresponding to an initial $S_2O_3^{2-}$ concentration of approximately 100 mmol/kg. At experimental conditions, thiosulfate dissociates rapidly by hydrolysis, generating H_2S and SO_4 in a 1:1 molar ratio [*Pokrovski et al.*, 2008; *Sakai and Dickson*, 1978; *Schoonen and Barnes*, 1991; *Wilkin and Barnes*, 1996] as follows:

$$S_2O_3^{2-} + H_2O + H^+ \rightarrow H_2S + HSO_4^- \qquad (2.2)$$

When pyrite is formed in the system, the overall reaction can be written as:

$$1.75H_2S + 0.25HSO_4^- + Fe^{2+} \rightarrow FeS_{2\,(Pyrite)} + 1.75H^+ + H_2O \qquad (2.3)$$

Accordingly, reaction stoichiometry predicts production of HSO_4^- and H_2S in equal proportions during thiosulfate disproportionation and consumption of H_2S and HSO_4^- at a 7:1 ratio during pyrite formation. Although the disproportionation of thiosulfate titrates H^+, the pH of the experimental solution remains effectively buffered due to the initial low pH and the production of H^+ resulting from charge balance constraints as dissolved Fe^{2+} is removed from solution by precipitation of pyrite (Table 2.2).

The S-species, HSO_4^- and H_2S, in addition to the likely existence of residual thiosulfate [*Chu et al.*, 2004; *Ohmoto and Lasaga*, 1982; *Ono et al.*, 2007], provide a well-known and effective pathway for homogeneous precipitation of pyrite formation [*Murowchick and Barnes*, 1986; 1987; *Schoonen and Barnes*, 1991]. Importantly, the addition of thiosulfate and its dissociation products also provides a redox buffer that limits Fe-mineral formation to the pyrite stability field, although this does not exclude the formation of metastable FeS intermediaries, which likely facilitated the incipient stages of precipitation from a homogenous solution [*Syverson et al.*, 2013]. The fluid in all experiments was rendered acidic, adjusted to low $pH_{25°C}$ (~1), creating conditions that promote fast S isotope exchange between SO_4 and H_2S [*Ohmoto and Lasaga*, 1982]. The acidic experimental solution also ensures that H_2S and HSO_4^- are the dominant aqueous S-species coexisting with pyrite at experimental pressure and temperature conditions.

Time-series fluid samples were taken to assess the extent of S isotope exchange and isotope fractionation among SO_4, H_2S, and pyrite, as the pyrite initially nucleated and subsequently crystallized. Upon completion of the experiment (after 3 to 180 days), the pressure vessel and its contents were quenched, similar to as described for the pyrite−H_2S exchange experiments. The rapid quench procedure was used to prevent S isotope

exchange between fluid and pyrite. Upon complete cooling, the pressure vessel and reaction cell were opened and pyrite crystals removed. The pyrite run products were then washed with deionized water, dried, and stored under an Ar atmosphere. The product pyrite was then studied by XRD and imaged by SEM to confirm that pyrite was indeed the only mineral present.

2.2.3. Thermodynamic modeling

Chemical speciation of the aqueous samples from each experiment was assessed using a thermodynamic database and modeling software [*Kong et al.*, 2013] to assess the effect of temperature and reaction progress on the distribution of aqueous S-bearing species and pyrite−fluid chemical equilibrium (Fig. 2.1). The thermodynamic data are largely derived using algorithms consistent with the Helgeson-Kirkham-Flowers equations of state and subsequent revisions [*Helgeson et al.*, 1981; *Shock et al.*, 1992; *Sverjensky et al.*, 1997; *Tanger and Helgeson*, 1988]. Details of the modeling approach are discussed in *Tutolo et al.* [2014]. Input to the model includes the total composition of fluid components (i.e., mNa^+, mCl^-, mFe^{2+}, mSO_4^{2-}, mH_2S) together with $pH_{25°C}$ (Tables 2.1 and 2.2). The measured fluid $pH_{25°C}$ is used with appropriate mass action and charge balance equations to calculate pH at experimental conditions (Fig. 2.1), which is necessary to calculate homogenous and heterogeneous chemical equilibria.

2.3. S Isotope Systematics

2.3.1. S separation and isotopic analysis

The pyrite crystals recovered from all of the experiments and the reactant native sulfur from the pyrite–H_2S exchange experiments were converted to H_2S with a boiling

chromous chloride solution [*Oduro et al.*, 2011]. The H_2S produced in the exchange experiments was sampled using a gas-tight glass sparger specifically designed to contain the gold capsules. Each capsule, placed vertically in the sparger, was punctured at the top with two holes by a syringe needle that entered the sparger through a septum. A continuous flow of N_2 purged through the syringe needle and inside the glass sparger, where the liberated H_2S flowed into $AgNO_3$ (0.1 mol/kg) solution and precipitated quantitatively as Ag_2S. Similarly, fluid samples from the pyrite precipitation experiments were taken in glass gas-tight syringes upon opening a high pressure titanium valve external to the gold reaction cell (cf: *Seyfried et al.* [1987]). The fluid samples were immediately weighed, and then injected into a sparge cell that was continuously purged with N_2 into $AgNO_3$ solution where it precipitated as Ag_2S. The residual fluid in the sparge cell was recovered and added to a $BaCl_2$ solution to precipitate SO_4 as $BaSO_4$, which was then converted to H_2S by the Thode technique [*Thode et al.*, 1961]; the evolved H_2S was carried by N_2 and trapped in $AgNO_3$ solution (0.1 m/kg) as precipitated Ag_2S. Sulfur isotope ratios were also measured for sulfonate (inner)- and sulfane (outer)-S of Na-thiosulfate (S source fluid prior to reaction) following the protocol reported by *Agarwala et al.* [1965]. Accordingly, the Na-thiosulfate was mixed with $AgNO_3$ to precipitate the sulfane-S (II) as Ag_2S. This precipitate was then separated by filtration, while the remaining sulfonate-S (VI) in the filtrate was mixed with $BaCl_2$ solution and precipitated as $BaSO_4$ and subjected to the Thode technique to produce Ag_2S for isotopic analysis.

Isotope analyses of all S-bearing compounds in source components and reaction products (fluid/mineral) were carried out at the Massachusetts Institute of Technology

using SF_6 generated by reaction of Ag_2S with $F_{2(g)}$ and purified by gas chromatography [*Ono et al.*, 2006]. SF_6 was analyzed in a Thermo MAT 253 isotope ratio mass-spectrometer using a dual-inlet mode for measurement of masses 127, 128, 129, and 131 (corresponding to $^{32}SF_5^+$, $^{33}SF_5^+$, $^{34}SF_5^+$, and $^{36}SF_5^+$, respectively). Reproducibility for complete analysis from fluorination, GC purification, and isotope ratio analysis are 0.14 and 0.26‰ (1σ) for $\delta^{33}S$ and $\delta^{34}S$, respectively. The average precision for $\Delta^{33}S$ is 0.006‰ (1σ) based on repeated analysis of international reference materials [*Ono et al.*, 2007; *Ono et al.*, 2012]. All S isotopic ratios in this study are reported in standard delta notation and are referenced with respect to the Vienna Cañon Diablo Troilite (VCDT) S reference scale, which is defined by the international reference material (IAEA-S1) to have –0.055 and -0.300‰ for $\delta^{33}S$ and $\delta^{34}S$, respectively [*Ono et al.*, 2007].

In this study we report standard delta notation, δ^yS, in all tables and majority of figures:

$$\delta^yS = \left[\frac{R^{y/32}}{R^{y/32}_{VCDT}} - 1\right] (‰) \qquad (2.4)$$

where y = 33 or 34. However, we also use modified delta notation, δ^yS', [*Angert et al.*, 2003; *Hulston and Thode*, 1965; *Young et al.*, 2002] to linearly describe multiple S isotope fractionation systematics between S-bearing phases/species:

$$\delta^yS' = ln\left[\frac{\delta^yS}{1000} + 1\right] \qquad (2.5)$$

We define the observed deviation from the reference equilibrium mass dependent fractionation for ^{33}S in capital delta notation, $\Delta^{33}S$, as [*Angert et al.*, 2003; *Ono et al.*, 2003]:

$$\Delta^{33}S = \delta^{33}S' - {}^{33}\theta_{ref}\,\delta^{34}S' \qquad (2.6)$$

where $^{33}\theta_{ref}$ is 0.515.

2.3.2. Multiple S isotope exchange: pyrite–H_2S

Pyrite–H_2S exchange systematics are described in terms of $\delta^{34}S$–$\Delta^{33}S$ (Fig. 2.2) and are largely similar to three-isotope approach concepts utilized by *Matsuhisa et al.* [1978], *Levin et al.* [2014], and *Jamieson et al.* [2006]. In effect, this exchange method compares the change in the triple S isotope fractionation of pyrite relative to H_2S, i.e. $\delta^{34}S_{Pyrite}$–$\delta^{34}S_{H2S}$ and $\Delta^{33}{}_{Pyrite}$–$\Delta^{33}{}_{H2S}$, before and following incremental isotopic exchange at experimental conditions. The $\Delta^{33}S$ fractionation between pyrite and H_2S, with reaction progress, effectively approaches zero (within analytical uncertainty of S isotope measurements, <0.008‰), as a consequence of the intrinsic equilibrium three isotope fractionation between pyrite and H_2S, $^{33}\theta_{Pyrite/H2S}$[2], being approximately equal to $^{33}\theta_{ref}$, 0.515 [*Ono et al.*, 2007]. With application of these constraints, the $^{34}S/^{32}S$ equilibrium isotope fractionation, $10^3 ln(^{34}\alpha_{(Pyrite/H2S)})$, can be estimated by bi-variate linear regression of the terminal $\delta^{34}S$–$\Delta^{33}S$ fractionations derived from the exchange experiments, as defined by equation 7:

$$\delta_{Pyrite}(t) - \delta_{H2S}(t) = \frac{\delta^0_{Pyrite} - \delta^0_{H2S} + \delta^e_{Pyrite} - \delta^e_{H2S}}{\Delta^0_{Pyrite} - \Delta^0_{H2S}} \left(\Delta_{Pyrite}(t) - \Delta_{H2S}(t)\right) + 10^3 ln(^{34}\alpha_{(Pyrite/H2S)}) \quad (2.7)$$

Where the *y*-intercept defines the equilibrium $^{34}S/^{32}S$ fractionation between pyrite and H_2S, $10^3 ln^{34}\alpha_{(Pyrite/H2S)}$ ($\simeq \delta^{34}S_{Pyrite} - \delta^{34}S_{H2S}$) and the slope defines the average degree of initial disequilibrium between pyrite and H_2S for all of the experiments compared (see Appendix A for the derivation of equation 7 and additional details). The superscript terms, "0" and "e", define time zero and equilibrium after infinite time, respectively. It

[2] $^{33}\theta = \left[\frac{ln(^{33}\alpha_{A/B})}{ln(^{34}\alpha_{A/B})}\right]$ where A/B represents SO_4^{2-}–H_2S, SO_4^{2-}–Pyrite, and Pyrite–H_2S (see Appendix A)

must be noted that this approach (Fig. 2.2) is only valid when applied to S isotope systems with small $\delta^{34}S$ and $\Delta^{33}S$ fractionations at equilibrium (ca. ≥10‰ for $\delta^{34}S$). Large mass-dependent fractionation results in non-linearity in $\delta^{34}S$–$\Delta^{33}S$ space upon mixing and fractionation between two S-bearing phases/species during isotopic exchange. In addition, the reactants must have contrasting $\Delta^{33}S$ values (i.e. disequilibrium) at time zero for this exchange approach to be effective.

The accuracy and sensitivity for $\Delta^{33}S$ measurements of S-bearing fluids and pyrite allow the triple isotope approach to be used for natural abundance isotope compositions, providing a powerful means to constrain equilibrium phase relations to compliment the traditional approach based on $^{34}S/^{32}S$ fractionation systematics alone. In particular, the mass dependent correlation of errors for $\delta^{33}S$ and $\delta^{34}S$, which cancel out when calculating $\Delta^{33}S$ values, lead to high-resolution and improved uncertainty with $\Delta^{33}S$ applications [*Ono et al.*, 2007]

2.3.3. Homogenous pyrite precipitation and recrystallization

Time series pyrite precipitation/recrystallization experiments were performed to compare with the S isotope data derived from the pyrite–H_2S exchange experiments and with natural MOR hydrothermal vent sulfide data. The time series data provide insight on the rate of S isotope exchange between pyrite and the aqueous S-reservoir. The concentration and S isotope composition of aqueous species were measured throughout the experiment and compared with the pyrite precipitate at the end of each experiment. The extent of S isotope exchange is evaluated by measuring the terminal $\Delta^{33}S$ fractionation of SO_4 relative to H_2S or pyrite, and pyrite relative to H_2S; i.e. $\Delta^{33}S_{SO4}$–$\Delta^{33}S_{H2S\ or\ Pyrite}$ and $\Delta^{33}S_{Pyrite}$–$\Delta^{33}S_{H2S}$. Thus, when comparing all aqueous S-

species and pyrite with respect to each other, the approach to S isotope equilibrium of the mineral−fluid system can be observed by convergence of all $\Delta^{33}S$ fractionation data towards effectively zero

.

2.4. Experimental Chemical Results

2.4.1. Pyrite–H_2S exchange experiments

The solution chemistry from the multiple S isotope exchange experiments (#5-1–#5-4) is shown in Table 2.1, wherein each experiment is described by the composition of the S-bearing reactants, pyrite (Pyr1–Pyr3), and native sulfur. The S-mass balance of the exchange experiments is such that the mineral reservoir is dominant (>99%) relative to the total dissolved S-species. The product solution Fe^{2+} concentration for each capsule is within 9% of the initial concentration, whereas the variability of dissolved S and pH reflects small differences in the initial S^0/H_2O mass ratio. Thermodynamic modeling of the solution chemistry for each capsule at P-T-X conditions of all experiments (Fig. 2.1) indicates that pyrite is at chemical equilibrium and indeed the only mineral present in the experimental system after reaction, which is also corroborated from SEM examination and XRD analysis of the mineral product.

2.4.2. Pyrite precipitation experiments

The chemical analyses of sequential samples of the hydrothermal fluids indicate that nucleation and precipitation of pyrite was virtually instantaneous at 300°C (Expt. #1) and 350°C (Expt. #2, 3, and 4) (Table 2.2). The precipitation of pyrite predictably induces large changes in the concentration of dissolved Fe and S species, although the change in $pH_{25°C}$ is modest owing to the decidedly low pH of the experimental source

fluid. Thus, after pyrite precipitation, dissolved Fe decreased from approximately 40 to 60 mmol/kg to between 2 and 14 mmol/kg. For each experiment, total dissolved SO_4 accounts for approximately 80% of total dissolved S-species in the residual fluid, with H_2S as the lesser component; the precipitated pyrite accounts for 42-49% of the total S in the mineral−fluid system, in keeping with constraints imposed by reactions (2) and (3). The S mass balance of the precipitation experiments is in sharp contrast with the exchange experiments. Fluid−mineral equilibria calculations are in excellent agreement with the formation of pyrite and only pyrite as the final reaction product (Fig. 2.1). Evidence for pyrite being the lone product of the precipitation process is also supported by results of SEM (Fig. 2.3) and XRD analyses. However, the crystal habit of the precipitated and recrystallized pyrite suggests that FeS(s) may play a potential role as a precursor prior to complete formation of pyrite upon sulfidation [*Graham and Ohmoto*, 1994]. Run products were specifically examined for the presence of native sulfur and marcasite [*Murowchick and Barnes*, 1986], but these phases were not observed, due to temperature and redox constraints more favorable for pyrite formation.

2.5. Multiple S Isotope Results

2.5.1. Reactant S-sources: native sulfur, pyrite, and thiosulfate

The S isotopic composition of starting native sulfur is 9.7, 18.8, and 0.038‰ for $\delta^{33}S$, $\delta^{34}S$, and $\Delta^{33}S$, respectively, while the terminal S isotopic composition of the pyrite crystals used for the exchange experiments ranged from -0.8 to 6.7, -1.5 to 13.1, and -0.068 to 0.002‰ for $\delta^{33}S$, $\delta^{34}S$, and $\Delta^{33}S$, respectively (Table 2.3). The bulk S isotopic composition of the thiosulfate used for the pyrite precipitation experiments is 1.8, 3.6,

and 0.010‰ for $\delta^{33}S$, $\delta^{34}S$, and $\Delta^{33}S$, respectively (Table 2.4). The sulfane-S (outer S) is more depleted in ^{34}S than the sulfonate-S (inner S) by 4.7‰. The disproportionation of both native sulfur and thiosulfate is rapid and non-reversible at experimental conditions.

2.5.2. Pyrite–H_2S exchange experiments: $\delta^{34}S$–$\Delta^{33}S$ systematics

The multiple S isotope pyrite–H_2S fractionation data, $\delta^{34}S_{Pyrite}$–$\delta^{34}S_{H2S}$ versus $\Delta^{33}S_{Pyrite}$–$\Delta^{33}S_{H2S}$, after recrystallization for 3384 hours follows the linear relationship expected from equation 7 (Fig. 2.4, Table 2.3). The S mass balance of each exchange experiment dictates that the pyrite S isotope reservoir will not change in isotope composition, but rather, the H_2S coexisting in the aqueous reservoir responds and records isotope exchange effects. As expected, from mass balance constraints and from multiple S isotope systematics, the $\Delta^{33}S_{H2S}$ data approaches that of the coexisting pyrite (Table 2.3), although $\Delta^{33}S_{H2S}$ data from experimental sample #5-1 H_2S exceeds that of the coexisting pyrite, #5-1 Pyr1, possibly due to isotopic heterogeneity of the reactant pyrite crystals used. The equilibrium $^{34}S/^{32}S$ fractionation between pyrite and H_2S, $10^3 ln^{34}\alpha_{(Pyrite\text{-}H2S)}$, determined from the linear regression of the multiple S isotope data from the exchange experiments is -1.9 ± 0.8‰ (1σ). This is markedly different from past equilibrium estimates at 350°C of 1‰ [*Ohmoto and Goldhaber*, 1997]. The equilibrium $^{33}S/^{32}S$ fractionation between pyrite and H_2S, $10^3 ln^{33}\alpha_{(Pyrite\text{-}H2S)}$, is -1‰.

2.5.3. Pyrite precipitation: $^{33,34}S/^{32}S$ fractionation systematics between SO_4 and H_2S

Multiple S isotope fractionation data (Table 2.4, Fig. 2.5) for the aqueous S-species after the precipitation of pyrite at 300°C (Expt. #1) reveal initial small SO_4-H_2S fractionation followed by an increase towards the predicted equilibrium value with reaction progress (arrow inset, Fig. 2.5) with *apparent* equilibrium attained at 56 hours

(data for 56 and 68 hour samples are virtually identical with data symbols overlapping). After less than an hour of reaction progress, the data for the $^{33}S/^{32}S$ and $^{34}S/^{32}S$ isotope fractionation for the SO_4–H_2S pair was 9.5 and 18.6‰, respectively. The data after 68 hours of reaction are statistically identical to theoretical predictions for the $^{33}S/^{32}S$ and $^{34}S/^{32}S$ isotope fractionation of 11.1 and 21.5‰, respectively, based on results of measured vibrational frequency data and *ab-initio* calculations [*Ono et al.*, 2007; *Otake et al.*, 2008]. We choose to use the equilibrium fractionation predictions for SO_4–H_2S equilibria derived by *Ono et al.* [2007] in Fig. 2.5, as these predictions agree more closely than *Otake et al.* [2008] with respect to the experimental fractionation data observed here. In the case of $^{34}S/^{32}S$ fractionation, this is also in excellent agreement with previously determined experimental data [*Ohmoto and Lasaga*, 1982].

Analogous multiple S isotope data from the 350°C experiments (Expts. #2–4; Table 2.4, Fig. 2.5) also closely follow predictions from recent models and earlier experiments. The time series trends of $^{33}S/^{32}S$ and $^{34}S/^{32}S$ fractionation data between SO_4 and H_2S observed from all experiments at 350°C trend towards equilibrium predictions with reaction progress (arrow inset). Moreover, the overall agreement between the measured SO_4−H_2S $^{33}S/^{32}S$ and $^{34}S/^{32}S$ fractionation data at both experimental temperatures (300 and 350°C) with theoretical predictions and previous experimental data, suggest that the formation of other S-species, such as SO_2 or S_3^- [*Bondarenko and Gorbaty*, 1997; *Pokrovski and Dubrovinsky*, 2011; *Pokrovski and Dubessy*, 2015; *Truche et al.*, 2014], which might undergo hydrolysis and disproportionation to SO_4 and H_2S upon quench, is unlikely at these particular experimental conditions.

Surprisingly, the rate of change at 350°C in $^{33}S/^{32}S$ and $^{34}S/^{32}S$, for Expt. #4, with reaction progress towards the predicted equilibrium for SO_4–H_2S fractionation is slower than that estimated from the homogenous S isotope exchange rate model at similar pH and total S concentrations (95% exchange within 3 hours) [*Ohmoto and Lasaga*, 1982]. This observation is less apparent for Expt. #2 and #3, possibly due to less reactive surface area of pyrite present, as less pyrite was precipitated from solution relative to Expt. #4. This result suggests that the rate of equilibration between the aqueous S-species in the pyrite−fluid system is inhibited by the recrystallization of pyrite during the early stages of reaction.

2.5.4. Pyrite precipitation: $^{34}S/^{32}S$ fractionation systematics between pyrite and aqueous S-species

The measured $^{34}S/^{32}S$ isotopic fractionation between pyrite and H_2S from Expt. #1 at 300°C, 4.26‰ (Table 2.4), is far from the previously estimated equilibrium fractionation, approximately 1‰. The $^{34}S/^{32}S$ fractionation between pyrite and SO_4 is also far from equilibrium with past equilibrium predictions. Analogous S isotope fractionation data at 350°C (Expt. #2–#4) are also not consistent, with respect to past equilibrium estimates. In fact, with increasing extent of reaction, the measured fractionations progressively approach the revised equilibrium fractionation estimate from this study. For example, the terminal S isotope fractionation between pyrite and H_2S measured for the experiment of longest duration (Expt. #4: 4297 hours) at 350°C, -1.95‰, is farther from the estimated equilibrium fractionation of 1‰ [*Ohmoto and Rye*, 1979], than the shorter term experiments, Expt. #2 (399 hours) and #3 (1082 hours): 0.19 and -0.47‰, respectively. The observed final S isotope fractionation between pyrite and

H_2S or SO_4 at 350°C differs from estimated equilibrium fractionation factors for $^{34}S/^{32}S$ by approximately 3‰. These differences provide important constraints on the distribution of S isotopes during rapid pyrite formation and subsequent recrystallization of pyrite.

2.5.5. Pyrite precipitation: $\Delta^{33}S$ systematics between pyrite and aqueous S-Species

$\Delta^{33}S$ values for H_2S, SO_4, and pyrite from each precipitation experiment fall within a narrow range from -0.012 to 0.041, although some variability still exists within and between experiments (Table 2.4 and Fig. 2.6). The variability in $\Delta^{33}S$ values for pyrite and the aqueous S-species reflects 1) isotope exchange between H_2S and SO_4 in response to the effects of thiosulfate decomposition and the rapid precipitation of pyrite at the start of each experiment and 2) the exchange of S isotopes between these aqueous species and pyrite during recrystallization in the course of the long term 350°C experiments. Although it is clear that temperature and reaction time contribute to the observed variability, systematic variation of the $\Delta^{33}S$ data with reaction progress suggests that the mineral−fluid S isotope system attains isotopic equilibrium in the longest-term precipitation experiment. This is exhibited best by comparing the $\Delta^{33}S$ fractionation among the S-bearing species and between the aqueous S-species and pyrite (Fig. 2.7), where the establishment of an equilibrium S isotopic distribution of the system is revealed by convergence of all $\Delta^{33}S$ fractionation values toward zero after 4297 hours of exchange.

2.6. Discussion

2.6.1. Equilibrium $^{34}S/^{32}S$ fractionation between pyrite and H_2S at 350°C

The equilibrium $^{34}S/^{32}S$ fractionation between pyrite and H_2S at 350°C derived from the multiple S isotope data from this study deviates significantly from estimates by *Ohmoto and Rye* [1979]. The likely reason for such disparity is due to the limited amount of experimental data to accurately estimate the equilibrium fractionation between pyrite and H_2S. The majority of compiled sulfide mineral–H_2S equilibrium fractionations reported are indirectly determined from a combination of a number of experimental $^{34}S/^{32}S$ studies, including fractionations between sulfide mineral–sulfide mineral, sulfide mineral–native sulfur, and native sulfur–H_2S/SO_4. Such approaches can inherit large uncertainties from propagation of analytical uncertainties and from experimental limitations, such as not being able to sample the solution phase at conditions for extended amounts of time [*Czamanske and Rye*, 1974; *Kajiwara and Krouse*, 1971; *Kajiwara et al.*, 1969; *Robinson*, 1973; *Sakai and Dickson*, 1978; *Uyama et al.*, 1985]. A few experimental studies [*Kiyosu*, 1973; *Nakai*, 1970] directly analyzed mineral−fluid sulfide S isotope fractionations. For example, *Kiyosu* [1973] performed $^{34}S/^{32}S$ isotope exchange experiments to determine the equilibrium $^{34}S/^{32}S$ fractionation between galena, sphalerite, and HS^- and found galena and sphalerite to be depleted and enriched in the ^{34}S, respectively, relative to coexisting HS^- at equilibrium throughout the temperature range of 100-300°C. *Nakai* [1970] is the only previous S isotope study which examined the $^{34}S/^{32}S$ fractionation between pyrite and aqueous S-species directly (SO_4, in particular) and concluded that isotopic exchange between pyrite and the aqueous S-reservoirs is rapid and equilibrium is approached within a few hours at 280°C. This observation

directly contradicts results from this experimental study conducted at higher temperature (350°C) and much longer duration (>4000 hours), and use of $\Delta^{33}S$ systematics to serve as an independent means of tracing equilibration of the mineral–fluid system (Fig. 2.7). The rate of S isotope exchange between the pyrite and aqueous S-reservoirs at 280°C is likely too slow to allow observable change in the S isotope composition of pyrite and SO_4 within the short duration of the experiments performed by *Nakai* [1970].

The experimentally determined equilibrium fractionation at 350°C, -1.9‰, also differs from recent theoretical estimates, where the difference in β-factors (reduced partition function ratios) between pyrite and H_2S from *Blanchard et al.* [2009] and *Otake et al.* [2008], respectively, suggest an equilibrium $^{34}S/^{32}S$ fractionation of +1.7‰ at 350°C. Large uncertainties result when calculating equilibrium fractionations by comparing results from different theoretical frameworks (i.e. mineral versus fluid) [*Beard et al.*, 2010; *Blanchard et al.*, 2012; *Blanchard et al.*, 2014; *Rustad et al.*, 2010]. In the case for pyrite, the calculation of $^{34}S/^{32}S$ β-factors can be made with predicted $^{56}Fe/^{54}Fe$ β-factors [*Blanchard et al.*, 2009; *Polyakov et al.*, 2013], as Fe and S β-factors are directly related based on their elemental contribution in kinetic energy in the lattice structure of pyrite (i.e. Fe and S force constants) relative to the total kinetic energy of pyrite at a given temperature. Empirically derived Fe force constant data from experimental equilibrium Fe isotope fractionation data between pyrite and dissolved Fe at 350°C by *Syverson et al.* [2013], same set of experiments as this study, agrees well with theoretical and spectroscopic predictions of the pyrite Fe force constant, thus, lending confidence in the accuracy of the theoretically predicted $^{34}S/^{32}S$ β-factor for pyrite. We hypothesize that the discrepancy in comparison of fractionations predicted for pyrite and

H_2S $^{34}S/^{32}S$ β-factors [*Blanchard et al.*, 2009; *Otake et al.*, 2008] with the equilibrium fractionation from this study likely arises from an inaccuracy in the magnitude of the $^{34}S/^{32}S$ β-factor for H_2S at 350°C. Inaccuracies may develop due to differences in theoretical assumptions for pyrite and H_2S, for example. Specifically for H_2S, inaccuracy in the $^{34}S/^{32}S$ β-factor predicted from studies such as *Otake et al.* [2008] and *Czarnacki and Hałas* [2012] could result from differences in the treatment of hydration of H_2S and anharmonicity with each theoretical model used. This study conjoined with *Syverson et al.* [2013] provides an example of a self-consistent data set from which Fe and S isotope fractionation systematics between pyrite and aqueous species can be used to evaluate the integrity of theoretical mineral−fluid fractionation predictions, especially for elevated pressure and temperature conditions indicative of seafloor hydrothermal systems.

Further experimental research needs to be conducted to calibrate the equilibrium multiple S isotope fractionations between a variety of metal sulfides and aqueous S-species at a range of temperature, pressure, and chemical conditions. It is expected that the magnitude of the equilibrium $^{34}S/^{32}S$ isotope fractionation between pyrite and aqueous S-species will decrease at increasing temperatures. However, it is less certain if pyrite will remain isotopically lighter than the total aqueous sulfide species, $\Sigma S^{2-}(aq)$, at equilibrium at different temperatures and chemical conditions relative to this study. For example, there may be a $^{34}S/^{32}S$ fractionation crossover between pyrite and H_2S upon a decrease in temperature or a shift in pH, at fixed temperature, will redistribute the relative abundance of aqueous sulfide species, effectively changing the sign and magnitude of S isotope fractionation between pyrite and $\Sigma S^{2-}(aq)$. Evaluation of these particular problems will help address further questions regarding the state of S isotopic (dis)equilibrium

between pyrite and other metal sulfides relative to aqueous S-species evolved at a variety of hydrothermal systems.

2.6.2. Exchange rate between pyrite and the aqueous S-reservoir at 350°C

To examine the level of reaction between the mineral and fluid S-reservoirs from the precipitation experiments at 350°C, the degree and rate of S isotope exchange between pyrite and the aqueous S-reservoir was quantified by applying the time-series $^{34}S/^{32}S$ isotope fractionation data between pyrite and H_2S to equation 8 [*Cole et al.*, 1983; *Ohmoto and Lasaga*, 1982]:

$$ln[(\alpha_{Eq}-\alpha_f)/(\alpha_{Eq}-\alpha_0)] = -kC_{\Sigma S}At \qquad (2.8)$$

where α_{Eq}, α_0, α_f, are the equilibrium fractionation factors at t = infinite (equilibrium), at t = 0 (initial), and t = t (final), respectively. The equilibrium pyrite–H_2S $^{34}S/^{32}S$ fractionation determined from this study is used (-1.9‰), while the initial $^{34}S/^{32}S$ fractionation is assumed to be +1.0‰, of which, provides the best fit y-intercept of the time-series fractionation data regressed to zero. This latter constraint is necessary since the initial fractionation of each experiment could not be measured directly. The expression in the brackets on the left side of equation 8 is equivalent to 1-F, where F is the degree of isotopic exchange (Fig. 2.8). Because the measured $^{34}S/^{32}S$ fractionation between pyrite and H_2S at the longest duration from the precipitation experiments, 4297 hours (Expt. #4), exceeds the estimated equilibrium fractionation by 0.05‰, we assume the mineral–fluid system has reached approximately 95% exchange toward equilibrium. The overall rate of isotope exchange is assumed to be proportional to the rate constant (k, [kg_{soln}/mol S/cm^2_{Pyrite}/hr]), the total concentration of S in solution, $C_{\Sigma S}$, (SO_4 + H_2S = 0.124 mol/kg, which is the calculated average of 350°C data from Table 2.2), and the

total surface area of pyrite, A, (4.85×10^5 cm^2; the average total pyrite surface area from all of the precipitation experiments at 350°C; determined from specific surface area analysis by N_2 gas adsorption isotherms). The rate constant, log(*k*), calculated to be -7.93, was determined from the slope of the linear regression of equation 8 forced through the origin, resulting in an R^2 of 0.99.

As indicated by Fig. 2.8, significant S isotope exchange takes place between pyrite and the aqueous S-reservoir, approximately 95%, in the course of 4297 hours after the pyrite precipitation event. In accord with $^{34}S/^{32}S$ fractionation data, convergence of $\Delta^{33}S$ values of pyrite, H_2S, and SO_4 demonstrate an approach to equilibrium with reaction progress (Fig. 2.7). Similarly, complimentary Fe isotope data from the pyrite precipitation experiments presented by *Syverson et al.* [2013] indicate that the pyrite–aqueous Fe-reservoirs have also undergone a considerable degree of iron isotopic exchange, approximately 76%, towards equilibrium during the same extent of reaction progress. The variation in the degree of exchange between the S and Fe isotope systems may reflect differences in 1) the analytical uncertainty of S and Fe isotope measurements, 2) the uncertainty in the initial and final S and Fe fractionations between pyrite and aqueous species, 3) uncertainty in the experimentally determined equilibrium fractionations, and 4) dissimilar total concentrations of S and Fe in solution (Table 2.2). If the rate of S isotope exchange is dependent on the total concentration of S in solution [*Ohmoto and Lasaga*, 1982], then the experimentally observed rate of equilibration from this study is likely much faster than equilibration rates at MOR hydrothermal vent system, where the total S in solution, in the form of H_2S, typically does not exceed concentrations greater than 10 mmol/kg [*German and Seyfried*, 2014]. Exchange

experiments performed by *Kiyosu* [1973] demonstrated significant S isotope exchange within a short duration of time (~10's of hours) between galena and sphalerite, with coexisting concentrated HS^- (800 mmol/kg). Such rapid overall rates of equilibration are likely facilitated by the significant concentration of HS^- in solution, roughly eight times more than that present in the time-series pyrite precipitation experiments.

If we apply the pyrite exchange rate data derived from this study to simulate natural hydrothermal systems (similar surface area as the pyrite in this study, with a high-temperature solution containing 10 mmol/kg total S with a constant S isotope composition) the pyrite S-reservoir would take approximately 10 years to equilibrate with coexisting H_2S, SO_4 or anhydrite ($CaSO_4$). *Ono et al.* [2007] compared $\delta^{34}S-\Delta^{33}S$ trends of chimney sulfides and vent fluid H_2S relative to seawater SO_4 at hydrothermal vents sites on the East Pacific Rise (EPR) and Mid-Atlantic Ridge (MAR) and found that S isotope exchange does indeed occur between the S-bearing mineral(s) and aqueous S-species, although the majority of vent H_2S and metal sulfides still remain in isotopic disequilibrium with respect to seawater SO_4 and between each other. It is likely that S and Fe isotope equilibrium between pyrite and hydrothermal fluids is rarely achieved in natural hydrothermal vent systems as a result of 1) temporal fluctuations in the temperature and isotope composition of vent fluids [*Bluth and Ohmoto*, 1988], 2) inheritance of S and Fe isotope compositions indicative of pathway dependent precursors required for pyrite formation [*Guilbaud et al.*, 2011a; *Polyakov and Soultanov*, 2011; *Rouxel et al.*, 2008; *Syverson et al.*, 2013], and 3) the slow rate of isotope exchange between pyrite and fluid.

2.6.3. Hydrothermal pyrite formation

Seafloor vent chimney sulfides, especially pyrite, are in some cases depleted in $\delta^{34}S$ relative to vent-fluid H_2S (Fig. 2.9) [*Bluth and Ohmoto*, 1988; *Kerridge et al.*, 1983; *Rouxel et al.*, 2008; *Shanks*, 2001; *Shanks and Seyfried*, 1987; *Shanks et al.*, 1995; *Woodruff and Shanks*, 1988], and were commonly interpreted to be far from S isotope equilibrium when compared to past equilibrium estimates [*Ohmoto and Rye*, 1979]. Results from the present multiple S isotope study, however, demonstrate that pyrite is expected to be depleted in the heavy isotopes of S relative to H_2S at equilibrium at 350°C, and that the majority of sampled hydrothermal vent systems are closer to S isotope equilibrium than previously thought. Specifically, comparison of $^{34}S/^{32}S$ isotope data of pyrite and coexisting H_2S sampled from the EPR 9-10°N hydrothermal vent field [*Rouxel et al.*, 2008] with the revised pyrite−H_2S equilibrium fractionation at 350°C (Fig. 2.10) indicates that pyrite is relatively close to S isotope equilibrium with H_2S. The pyrite and H_2S $^{34}S/^{32}S$ isotope compositions from EPR 9-10°N plot between the equilibrium fractionations of FeS–H_2S and pyrite–H_2S, similar to the majority of compiled pyrite–H_2S $^{34}S/^{32}S$ fractionation data from a variety of high temperature MOR vent systems [*Shanks*, 2001], suggesting that FeS may be pivotal as a precursor to the formation of pyrite. Similarly, S isotope results from the time-series pyrite precipitation experiments are also consistent with an intermediary role of FeS during pyrite formation (Fig. 2.10, inset figure). The experimental data demonstrate isotopic evolution of the mineral–fluid reservoirs by the change in the $^{34}S/^{32}S$ fractionation data near FeS–H_2S equilibrium initially and then trending towards pyrite–H_2S equilibrium with increasing extent of reaction. A more robust constraint for the formation of FeS precursors upon pyrite

formation is obtained from the Fe isotope system, since the conversion of FeS to pyrite involves the partial oxidation of FeS and addition of external sulfur to FeS. *Rouxel et al.* [2008] analyzed the Fe isotope composition of pyrite and coexisting vent fluids from EPR 9-10°N. The observed Fe isotope disequilibrium recorded by pyrite relative to aqueous Fe can be explained by inheritance of the Fe isotope composition of FeS, an intermediate phase produced during the rapid formation of pyrite [*Polyakov and Soultanov*, 2011]. Complimentary experimental Fe isotope evidence from the pyrite precipitation experiments presented by *Syverson et al.* [2013] is also consistent with the model that pyrite is likely formed from an intermediate FeS phase. The FeS model is also in line with observations of the transformative crystallographic nature of the recrystallizing pyrite in this study (Fig. 2.3) [*Graham and Ohmoto*, 1994]. Furthermore, the hydrothermal data observed here are in agreement with low temperature S and Fe isotope data, which demonstrate that FeS is readily formed upon interaction between S- and Fe-aqueous species and is an instrumental reactive component for pyrite formation [*Butler et al.*, 2004; *Butler et al.*, 2005; *Guilbaud et al.*, 2011a]. The S and Fe isotope data obtained here do not provide sufficient evidence to allow unambiguous determination of the S oxidant, likely either SO_4 or $S_2O_3^{2-}$, upon pyrite formation from FeS precursors. Additionally, this particular hydrothermal mechanism of pyrite formation produces small mass-dependent Δ^{33} values that are consistent with hydrothermally derived sulfides at MOR systems, such as at EPR 9-10°N [*Ono et al.*, 2007; *Peters et al.*, 2010]. This observation is in stark contrast with the formation of biogenic sulfides produced by the reduction of seawater SO_4, which are anomalous in Δ^{33} values [*Farquhar et al.*, 2003; *Johnston et al.*, 2005; *Ono et al.*, 2006]. The inferences gained by

combination of field and experimental S and Fe isotope data provide evidence that the formation of the precursor, FeS, is ubiquitous and necessary for pyrite nucleation from solution at similar P-T-X conditions present at MOR hydrothermal vent systems and ore depositional environments elsewhere.

2.7. Conclusions

Triple S isotope ($^{33}S/^{32}S$ and $^{34}S/^{32}S$) systematics were studied amongst pyrite, SO_4, and H_2S during the precipitation and recrystallization of pyrite at hydrothermal conditions relevant to natural submarine hydrothermal systems. Using the combination of $\delta^{34}S$ and $\Delta^{33}S$ exchange systematics, we update the equilibrium $^{34}S/^{32}S$ fractionation between pyrite and H_2S at 350°C to be -1.9‰. The value is different from the previously recommended value of +1‰ [*Ohmoto and Rye*, 1979] and from combination of recent spectroscopic and theoretical predictions [*Blanchard et al.*, 2009; *Ono et al.*, 2007; *Otake et al.*, 2008; *Polyakov and Soultanov*, 2011; *Polyakov et al.*, 2013]. The revised $^{34}S/^{32}S$ pyrite–H_2S equilibrium fractionation at 350°C compared with MOR hydrothermal sulfide data suggests that the S isotope system is closer to equilibrium than previously suggested. Our experiments demonstrate relatively sluggish equilibration rates between the aqueous S-species, H_2S and SO_4, at 350°C upon precipitation and during the early stages of pyrite recrystallization, compared to the homogenous (fluid) S isotope system, low pH and high dissolved concentrations of coexisting S-species notwithstanding. This result may provide better constraints on the residence times of hydrothermal fluid in the subseafloor of natural hydrothermal systems, where pyrite is ubiquitous. These data confirm that anomalous $\delta^{34}S$ and $\Delta^{33}S$ values amongst SO_4, H_2S, and pyrite may be produced during

the incipient stage of rapid pyrite nucleation and precipitation suggestive of pyrite formation from FeS precursors, and relatively long reaction times are likely needed to erase these effects. The role of FeS as a precursor for hydrothermal pyrite formation, recognized from seafloor vent and laboratory Fe isotope studies [*Rouxel et al.*, 2008; *Syverson et al.*, 2013], lends strength to this interpretation. Thus, pathway dependent S isotope fractionation effects during pyrite precipitation at deep sea vents provide a new and critical insight into the long-standing question for S isotope disequilibrium between sulfide minerals and vent fluid H_2S.

Table 2.1: Initial and sampled fluid chemistry of each pyrite – H_2S exchange experiment after 3384 hours of recrystallization at 350°C and 500 bars.

Capsule	$X_{S(Pyr)}$	$pH_{25°C}$	$[Fe^{2+}]$	$[H_2S]$	$[SO_4]$	$[Na^+]$	$[Cl^-]$
Starting Solution	-	2.31	20.1	0	0	992	1076
5-1 (Pyr3-S^0)	0.99	2.01	20.5	5.8	14.7	988	1072
5-2 (Pyr1-S^0)	0.99	2.36	21.1	4.4	5.1	1011	1090
5-3 (Pyr3-S^0)	0.99	1.77	20.3	11.1	10.8	1007	1072
5-4 (Pyr2-S^0)	0.99	2.21	21.3	5.2	6.7	982	1062

All concentrations are represented in mmol/kg solution. The relative standard deviation (2σ) for the concentration of the individual dissolved components by ICP-OES and ion chromatography is ±2% for Na^+ and SO_4, ±1% for Fe^{2+}, and ±1% for Cl. The relative standard deviation associated with H_2S is ±3%.

Table 2.2: Sampled fluid chemistry of each precipitation experiment with time.

300°C #1	Time (hrs)	$pH_{25°C}$	$[Fe^{2+}]$	$[H_2S]$	$[SO_4]$	$[Na^+]$	$[Cl^-]$	Soln. Mass
1-1	-	1.06	37.8	0	0	861	1036	43.4
$Na_2S_2O_3$ inj.	0.0	6.67	0	0	0	1992	0	*3.9
1-2	0.8	1.16	13.6	16.8	67	947	969	49.0
1-3	56	1.10	11.9	16.1	70	963	983	43.2
1-4	68	1.06	11.6	16.2	67	935	958	38.6
350°C #2	Time (hrs)	$pH_{25°C}$	$[Fe^{2+}]$	$[H_2S]$	$[SO_4]$	$[Na^+]$	$[Cl^-]$	Soln. Mass
2-1	-	1.05	36.9	0	0	870	1030	44.1
$Na_2S_2O_3$ inj.	0.0	6.67	0	0	0	1992	0	*5.7
2-2	0.3	1.22	8.5	21.8	86	966	942	50.8
2-3	332.7	1.14	8.0	18.0	87	956	950	46.8
2-4	398.7	1.17	7.8	23.3	86	958	951	40.9
350°C #3	Time (hrs)	$pH_{25°C}$	$[Fe^{2+}]$	$[H_2S]$	$[SO_4]$	$[Na^+]$	$[Cl^-]$	Soln. Mass
3-1	-	1.06	38.5	0	0	863	1033	53.9
$Na_2S_2O_3$ inj.	0.0	6.67	0	0	0	1992	0	*5.9
3-2	0.6	1.13	2.0	n.a.	101	994	924	52.6
3-3	720	1.08	1.7	30.7	98	1009	928	48.5
3-4	1082	1.15	2.1	33.2	101	1002	943	43.9
350°C #4	Time (hrs)	$pH_{25°C}$	$[Fe^{2+}]$	$[H_2S]$	$[SO_4]$	$[Na^+]$	$[Cl^-]$	Soln. Mass
4-1	-	1.04	59.1	0	0	872	1033	50.6
$Na_2S_2O_3$ inj.	0.0	6.67	0	0	0	1992	0	*7.1
4-2	0.5	1.10	8.4	15.9	108	1103	1040	55.5
4-3	25	1.11	7.7	17.6	110	1114	1042	51.9
4-4	46	1.10	7.6	18.3	110	1100	1038	49.3
4-5	865	1.08	7.6	19.4	111	1097	1035	46.4
4-6	3553	1.13	7.6	20.7	111	1126	1021	43.2
4-7	4297	1.07	7.3	19.2	110	1116	1018	40.6

All concentrations are represented in mmol/kg solution. The injection of the Na-thiosulfate solution, prior to sampling event 2, is indicated by the presence of sulfur species in the system and the increase of the Na^+ concentration. The relative standard deviation (2σ) for the concentration of the individual dissolved components by ICP-OES and ion chromatography is ±2% for Na^+ and SO_4, ±1% for Fe^{2+}, and ±1% for Cl^-. The relative standard deviation associated with H_2S is ±3%. The dashes, "-", indicate the sampling prior to the injection of the Na-thiosulfate solution. Time "zero" is immediately after the thiosulfate injection. *Amount (grams) of Na-thiosulfate solution injected into gold cell. The solution mass reported is representative of the mass before each sampling event.

Table 2.3: Multiple S isotope data for the pyrite – H_2S partial exchange experiments after 3384 hours of recrystallization at 350 °C and 500 bars.

Native S source	$\delta^{33}S$	$\delta^{34}S$	$\Delta^{33}S$
S^0	9.655	18.756	0.038
Product Pyrite and H_2S	$\delta^{33}S$	$\delta^{34}S$	$\Delta^{33}S$
5-1 Pyr1	0.982	1.954	-0.024
5-2 Pyr2	-0.794	-1.503	-0.020
5-3 Pyr3	2.055	4.087	-0.048
5-4 Pyr4	6.651	13.089	-0.068
5-1 H_2S	2.704	5.330	-0.038
5-2 H_2S	-0.722	-1.407	0.002
5-3 H_2S	0.973	1.947	-0.030
5-4 H_2S	5.098	9.989	-0.034

The average precision for $\delta^{33}S$ and $\delta^{34}S$ is 0.010‰ (1σ), respectively. The average precision for $\Delta^{33}S$ is 0.006‰ (1σ).

Table 2.4: S isotopic composition of the thiosulfate source and sampled SO_4, H_2S, and product pyrite.

Thiosulfate Source		$\delta^{33}S$ (Inner-S)	$\delta^{34}S$ (Inner-S)	Δ^{33} (Inner-S)	$\delta^{33}S$ (Outer-S)	$\delta^{34}S$ (Outer-S)	$\Delta^{33}S$ (Outer-S)
		3.081	5.979	0.006	0.684	1.302	0.014
Expt. #1 300°C	Time (hours)	$\delta^{33}S$ (SO_4)	$\delta^{34}S$ (SO_4)	Δ^{33} (SO_4)	$\delta^{33}S$ (H_2S)	$\delta^{34}S$ (H_2S)	Δ^{33} (H_2S)
1-1	-	-	-	-	-	-	-
1-2	0.8	6.542	12.766	-0.012	-2.974	-5.801	0.018
1-3	56	7.069	13.769	0.001	-4.030	-7.841	0.016
1-4	68	6.846	13.255	0.041	-4.261	-8.307	0.026
Pyrite (1-4)	68	-2.088	-4.046	-0.002			
Expt. #2 350°C	Time (hours)	$\delta^{33}S$ (SO_4)	$\delta^{34}S$ (SO_4)	Δ^{33} (SO_4)	$\delta^{33}S$ (H_2S)	$\delta^{34}S$ (H_2S)	$\Delta^{33}S$ (H_2S)
2-1	-	-	-	-	-	-	-
2-2	0.3	6.065	11.821	-0.006	-3.469	-6.746	0.011
2-3	333	6.232	12.120	0.008	-2.892	-5.668	0.031
2-4	399	6.244	12.135	0.012	-2.576	-5.017	0.011
Pyrite (2-4)	399	-2.494	-4.828	-0.004			
Expt. #3 350°C	Time (hours)	$\delta^{33}S$ (SO_4)	$\delta^{34}S$ (SO_4)	Δ^{33} (SO_4)	$\delta^{33}S$ (H_2S)	$\delta^{34}S$ (H_2S)	$\Delta^{33}S$ (H_2S)
3-1	-	-	-	-	-	-	-
3-2	0.6	n.a.	n.a.	n.a.	n.a.	n.a.	n.a.
3-3	720	6.532	12.670	0.028	-2.786	-5.424	0.012
3-4	1082	5.939	11.498	0.034	-2.745	-5.348	0.012
Pyrite (3-4)	1082	-2.978	-5.816	0.022			
Expt. #4 350°C	Time (hours)	$\delta^{33}S$ (SO_4)	$\delta^{34}S$ (SO_4)	Δ^{33} (SO_4)	$\delta^{33}S$ (H_2S)	$\delta^{34}S$ (H_2S)	$\Delta^{33}S$ (H_2S)
4-1	-	-	-	-	-	-	-
4-2	0.5	6.399	12.426	0.019	-1.780	-3.436	-0.009
4-3	25	6.678	12.968	0.020	-2.044	-3.985	0.010
4-4	46	6.529	12.673	0.022	-1.757	-3.447	0.020
4-5	865	6.276	12.166	0.029	-1.708	-3.333	0.010
4-6	3553	6.788	13.183	0.020	-2.060	-4.031	0.018
4-7	4297	7.158	13.938	0.004	-2.084	-4.046	0.002
Pyrite (4-7)	4297	-3.082	-5.996	0.010			

The average precision for $\delta^{33}S$ and $\delta^{34}S$ is 0.010‰ (1σ), respectively. The average precision for $\Delta^{33}S$ is 0.006‰ (1σ). The dashes, "-", indicate the sampling prior to the injection of the Na-thiosulfate solution when there is no sulfur in solution. Time "zero" is immediately after the thiosulfate injection. "n.a." indicates that the individual sample was not analyzed for S isotopes.

Figure 2.1

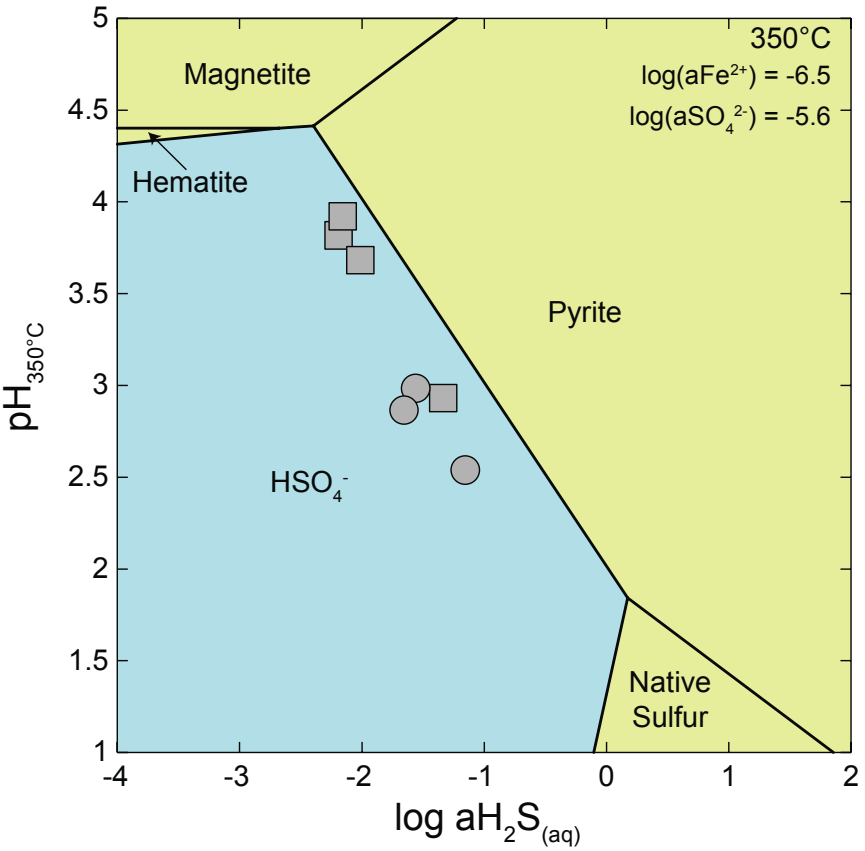

Fig. 2.1 Model $pH_{350°C}$ versus $aH_2S_{(aq)}$ depicting phase boundaries between aqueous HSO_4^- and Fe- and S-bearing minerals, magnetite, hematite, pyrite, and native sulfur at 350°C and 500 bars for all experiments presented. The terminal (final) speciated fluid samples derived from the gold capsule exchange and the pyrite precipitation experiments are depicted as squares and circles, respectively. All of the data plot near the HSO_4^-–pyrite join, suggesting pyrite–fluid chemical equilibria. Speciated fluid chemistry from Expt. #1, at 300°C, (not shown) also demonstrates HSO_4^-–pyrite saturation equilibrium. The model activities of dissolved Fe^{2+} and SO_4^{2-} (top right) are derived from the average speciated activity of each from all experiments presented. Thus, the plotted data are offset from the HSO_4^-–pyrite join. Speciation calculations of individual experiments plot directly along the HSO_4^-–pyrite join. See text for sources of thermodynamic data for minerals and aqueous species used for the construction of the activity diagram.

Figure 2.2

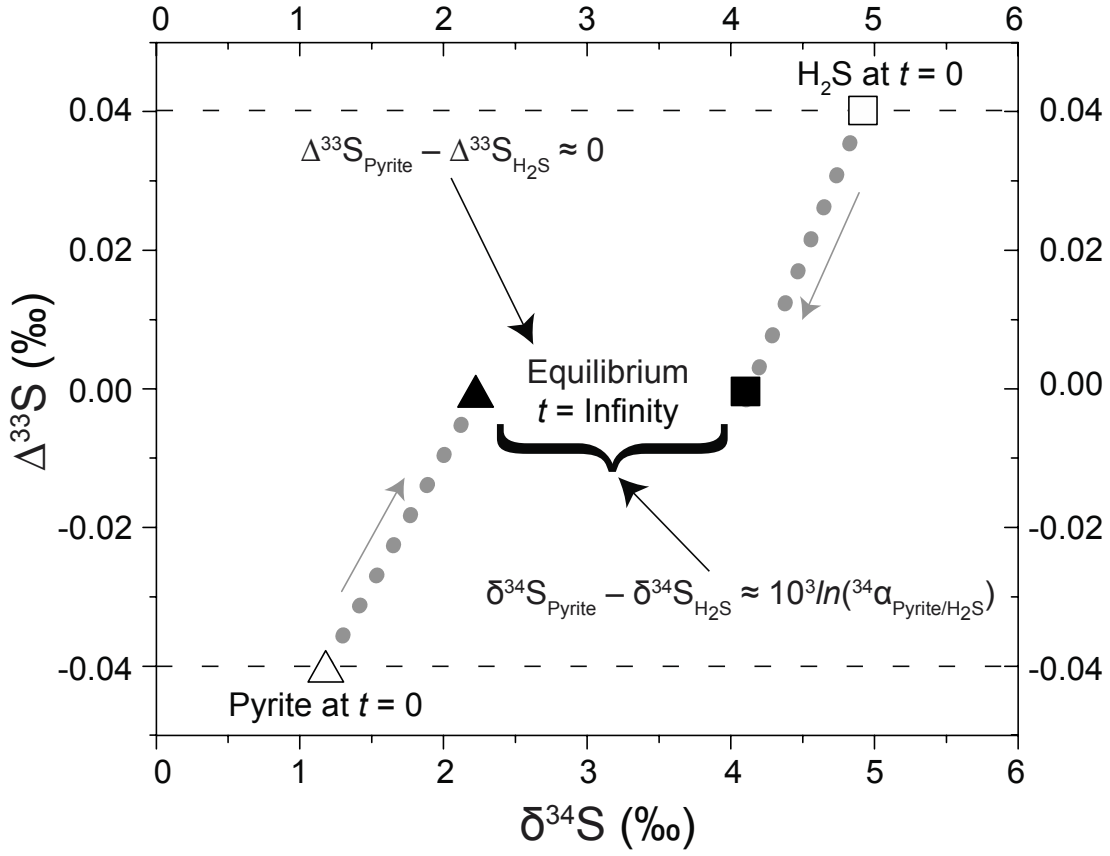

Fig. 2.2 Schematic illustration of $\delta^{34}S$–$\Delta^{33}S$ exchange systematics between pyrite and H_2S, which differ in $\delta^{34}S$ and $\Delta^{33}S$ compositions at the initial stage of the exchange reaction, $t = 0$. The recrystallization of the pyrite at 350°C drives isotopic exchange between pyrite and H_2S at hydrothermal conditions. For this example, the S isotope mass balance between the mineral–fluid reservoirs is poised at 50:50. The extent of exchange is depicted as the grey arrows for both pyrite and H_2S along the grey dotted line. Equilibrium is established at t = Infinity, where both pyrite and H_2S share similar $\Delta^{33}S$ and are offset in $\delta^{34}S$ by the $^{34}S/^{32}S$ equilibrium fractionation, $10^3 ln(^{34}\alpha_{Pyrite/H2S})$. The $\delta^{34}S$–$\Delta^{33}S$ approach assumes that the trajectory of pyrite and H_2S from initial to equilibrium conditions is approximately linear, allowing application of equation 2.7 (see text and Appendix A).

Figure 2.3

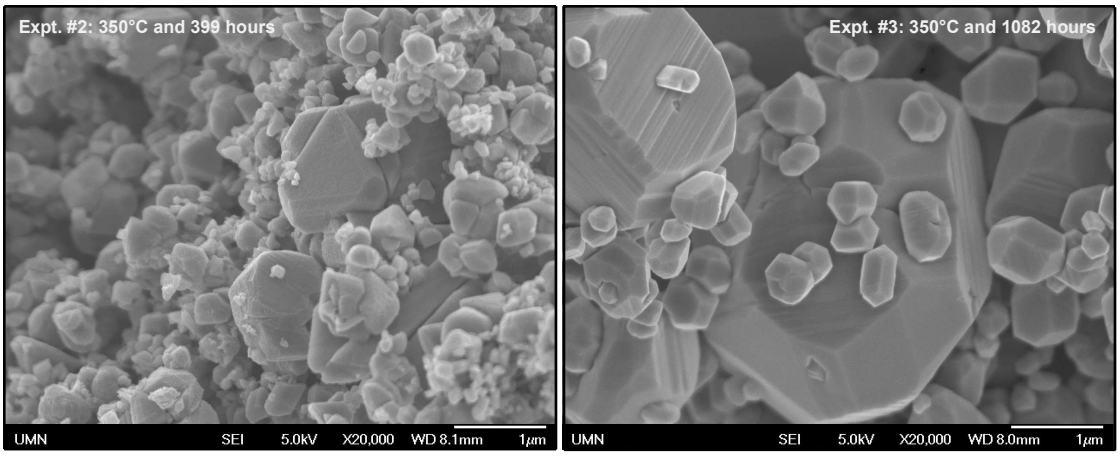

Fig. 2.3 Scanning electron microscope images of precipitated pyrite at 350°C after recrystallization for 399 and 1082 hours, Expt. #2 and 3, respectively. The transition of the pyrite grains from subhedral to a more euhedral morphology during grain growth coupled with steady state chemistry of the coexisting fluid with time (Table 2) suggests recrystallization is the dominant isotopic exchange mechanism. The habit of the pyrite morphology of pyrite is indicative of formation upon sulfidation of precursor FeS, rather than direct nucleation from solution, as evidenced by past pyrite nucleation and growth experiments by and *Graham and Ohmoto* [1994].

Figure 2.4

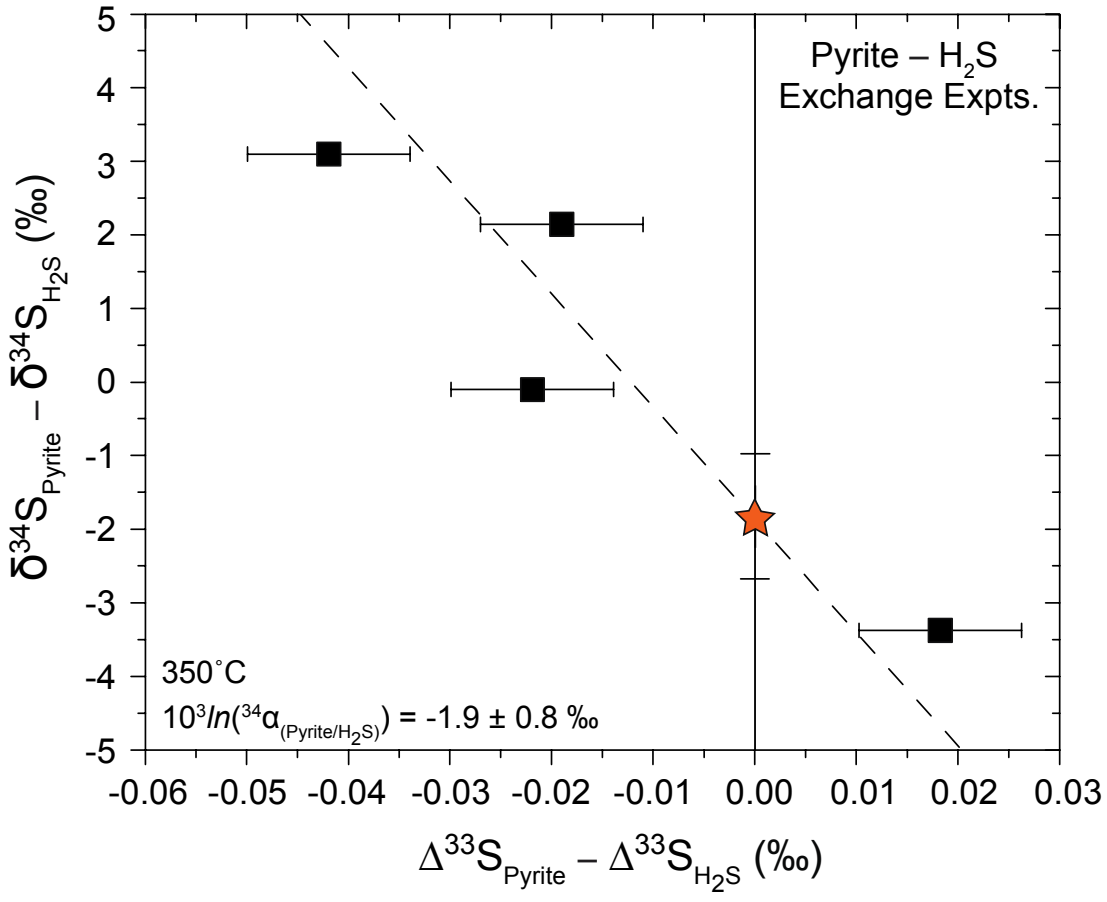

Fig. 2.4 $\delta^{34}S$–$\Delta^{33}S$ fractionation data for the pyrite–H_2S pair at 350°C measured from the pyrite exchange experiments. The pyrite exchange experiments had undergone 3384 hours of recrystallization. The equilibrium $^{34}S/^{32}S$ pyrite–H_2S fractionation at 350°C, -1.9‰, estimated from the *y*-intercept (orange star) as determined by bi-variate linear regression of $\delta^{34}S$ and $\Delta^{33}S$ data (Eqn. 2.7), is far from the past equilibrium estimate from *Ohmoto and Rye* [1979], 1‰. Error (1σ) for each observed $^{34}S/^{32}S$ fractionation between pyrite and H_2S is the vertical length of the symbols, whereas the error (1σ) for the observed $\Delta^{33}S$ fractionation is 0.008‰.

Figure 2.5

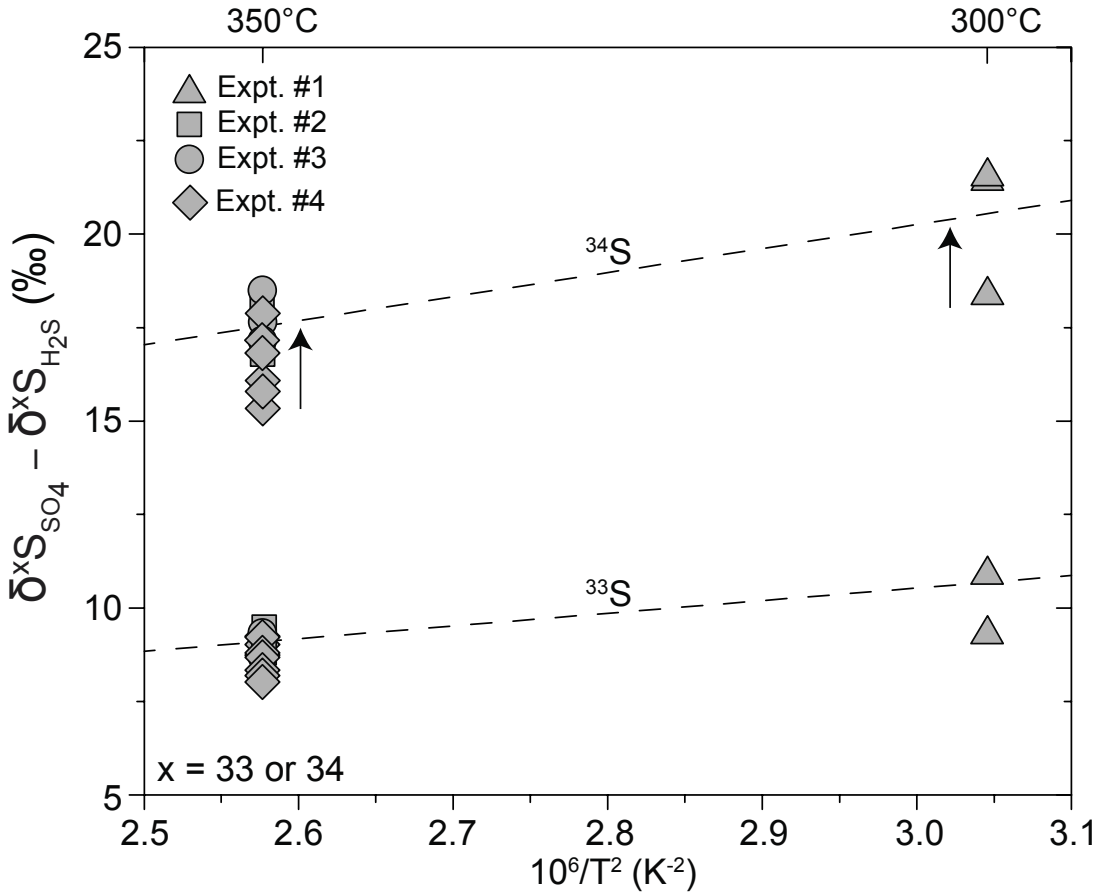

Fig. 2.5 Experimentally determined $^{x}S/^{32}S$ fractionation data, where x=33 or 34, between dissolved SO_4 and H_2S at 300° and 350°C in comparison with available theoretical data. Experimental data (Expt. #1) at 300°C are indicated by triangles. The 350°C experiments, #2, #3, #4, are represented by squares, circles, and diamonds, respectively. The dashed lines for each S isotope ratio presented are derived from vibration frequency data used for SO_4–H_2S isotopic equilibrium predictions from *Ono et al.* [2007]. Theoretical fractionation predictions from *Otake et al.* [2008] (not shown) are similar in magnitude. Arrows indicate the progression of fractionation values with time. The $^{34}S/^{32}S$ isotopic fractionation converges to ~21.5‰ at 300°C (inset arrow). Analogous data from the 350°C experiments, #2–4, approach the predicted equilibrium fractionation with increasing extent of reaction progress (inset arrow). The average terminal $^{34}S/^{32}S$ isotopic fractionation between SO_4 and H_2S at 350°C is 17.3‰. The $^{33}S/^{32}S$ isotopic fractionation data behave similarly to $^{34}S/^{32}S$ fractionation systematics at both temperatures.

Figure 2.6

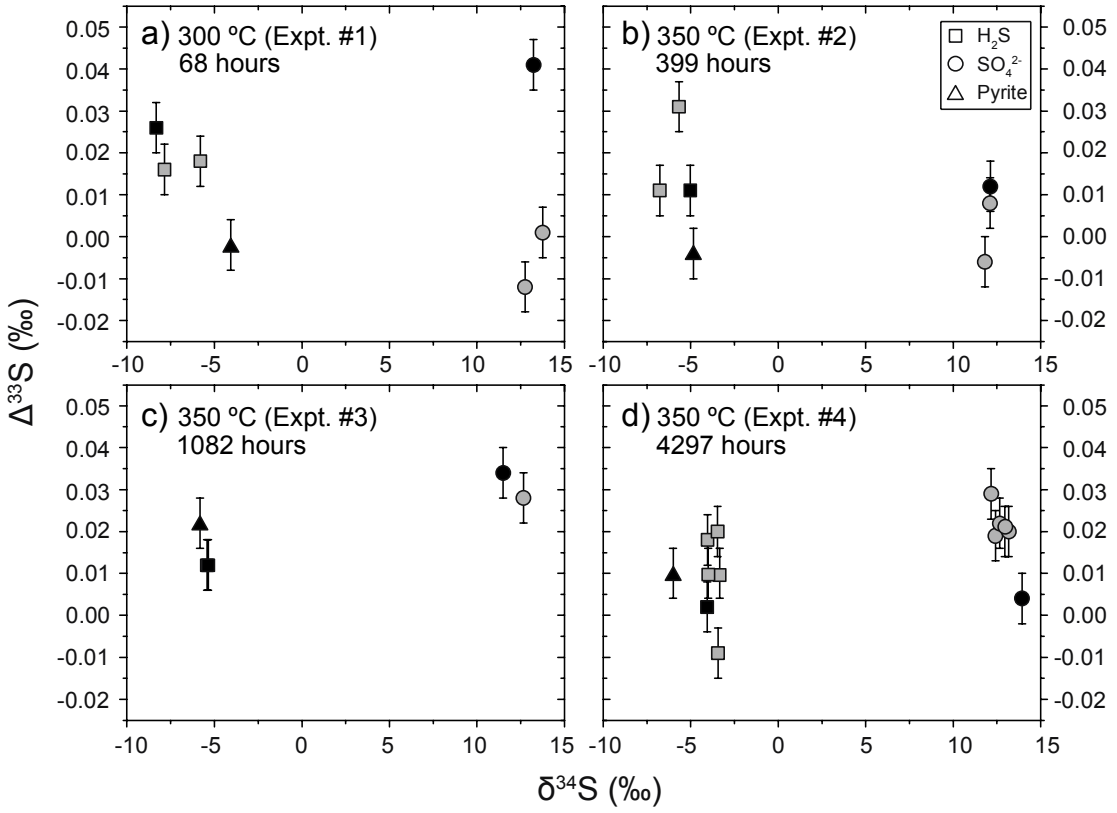

Fig. 2.6 $\delta^{34}S$–$\Delta^{33}S$ data for dissolved S-species and pyrite as a function of temperature and time for each experiment. Dissolved H_2S (squares), SO_4 (circles), and product pyrite (triangles); the terminal (final) $\delta^{34}S$ and $\Delta^{33}S$ composition SO_4, H_2S, and pyrite from each experiment are displayed as black symbols. In general, when comparing the final compositions of pyrite and the aqueous S-species, the time series $\delta^{34}S$–$\Delta^{33}S$ data (a-d) exhibit scatter during the early stages of pyrite recrystallization with the fluid (a-b) but then progressively converge towards more similar values with reaction progress (c-d), demonstrating an approach to isotopic equilibrium for the mineral−fluid system. Error (1σ) for each observed $\delta^{34}S$ for SO_4, H_2S, and pyrite is the horizontal length of the symbols, whereas the error (1σ) for observed $\Delta^{33}S$ is 0.006‰.

Figure 2.7

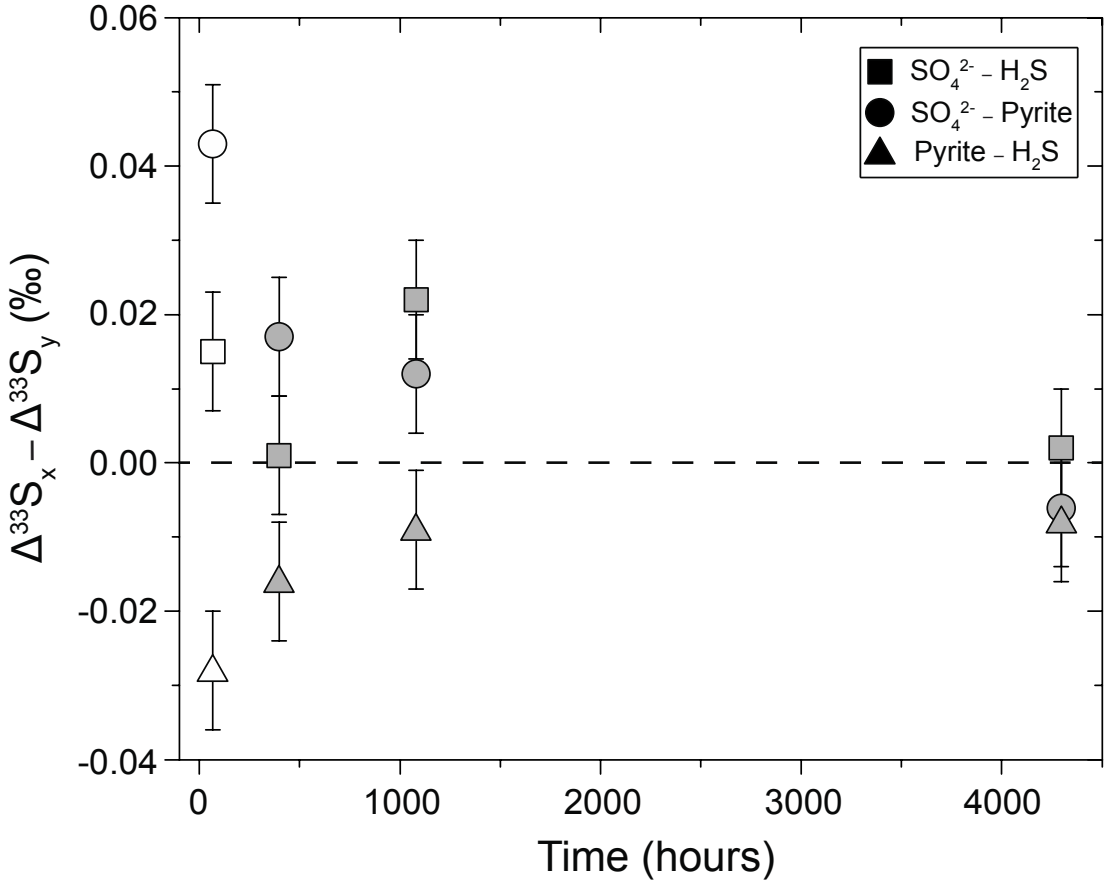

Fig. 2.7 Time series fractionation data for pyrite precipitation experiments at 300-350°C ($\Delta^{33}S = \Delta^{33}S_x – \Delta^{33}S_y$, where x and y are species or minerals of interest) shows the difference in the final $\Delta^{33}S$ composition between SO_4–H_2S, SO_4–pyrite, and pyrite–H_2S. The mineral–fluid S isotope system reaches equilibrium when all $\Delta^{33}S$ fractionation data approach zero at 300-350°C (dashed line). $\Delta^{33}S$ fractionation data for SO_4–H_2S, SO_4–pyrite, and pyrite–H_2S pairs are depicted as squares, circles, and triangles, respectively. The 300°C data is represented by open symbols whereas all 350°C data are represented as grey symbols. The $\Delta^{33}S$ fractionation data during the short term experiment at 300°C, Expt. #1, displays the largest disequilibrium, due to initial non-equilibrium fractionation and a relatively short experimental time-frame of recrystallization. During increasing intervals of reaction progress at higher temperature, 350°C (399–4297 hours), the recrystallization of pyrite facilitates the mineral–fluid system to approach $\Delta^{33}S$ fractionation values indicative of equilibrium. Errors displayed are approximately 0.008‰ (1σ).

Figure 2.8

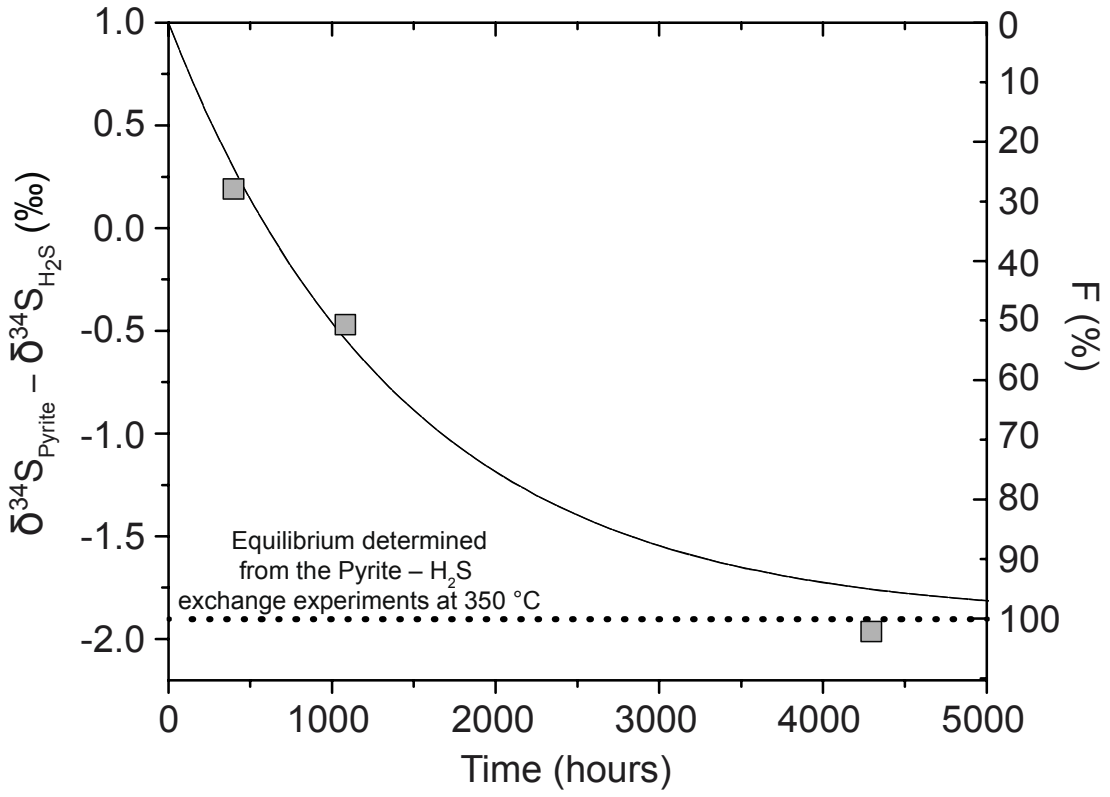

Fig. 2.8 Time series trend of $^{34}S/^{32}S$ pyrite–H_2S fractionation data derived from the pyrite precipitation experiments at 350°C. The observed time-series data asymptotically approach the equilibrium $^{34}S/^{32}S$ fractionation of -1.9‰ between pyrite and H_2S during the exchange experiments (dashed line). The time-series $^{34}S/^{32}S$ fractionation data were regressed with equation 8 (see text) and is illustrated by the continuous line; the rate data was then used to model the degree of exchange, *F* (%), with time. The data indicate progressive exchange between the mineral and fluid S-reservoirs, where greater than ~95 % exchange took place during the approach to equilibrium after 4297 hours. Error (1σ) for each observed $^{34}S/^{32}S$ fractionation between pyrite and H_2S is the vertical length of the symbols.

Figure 2.9

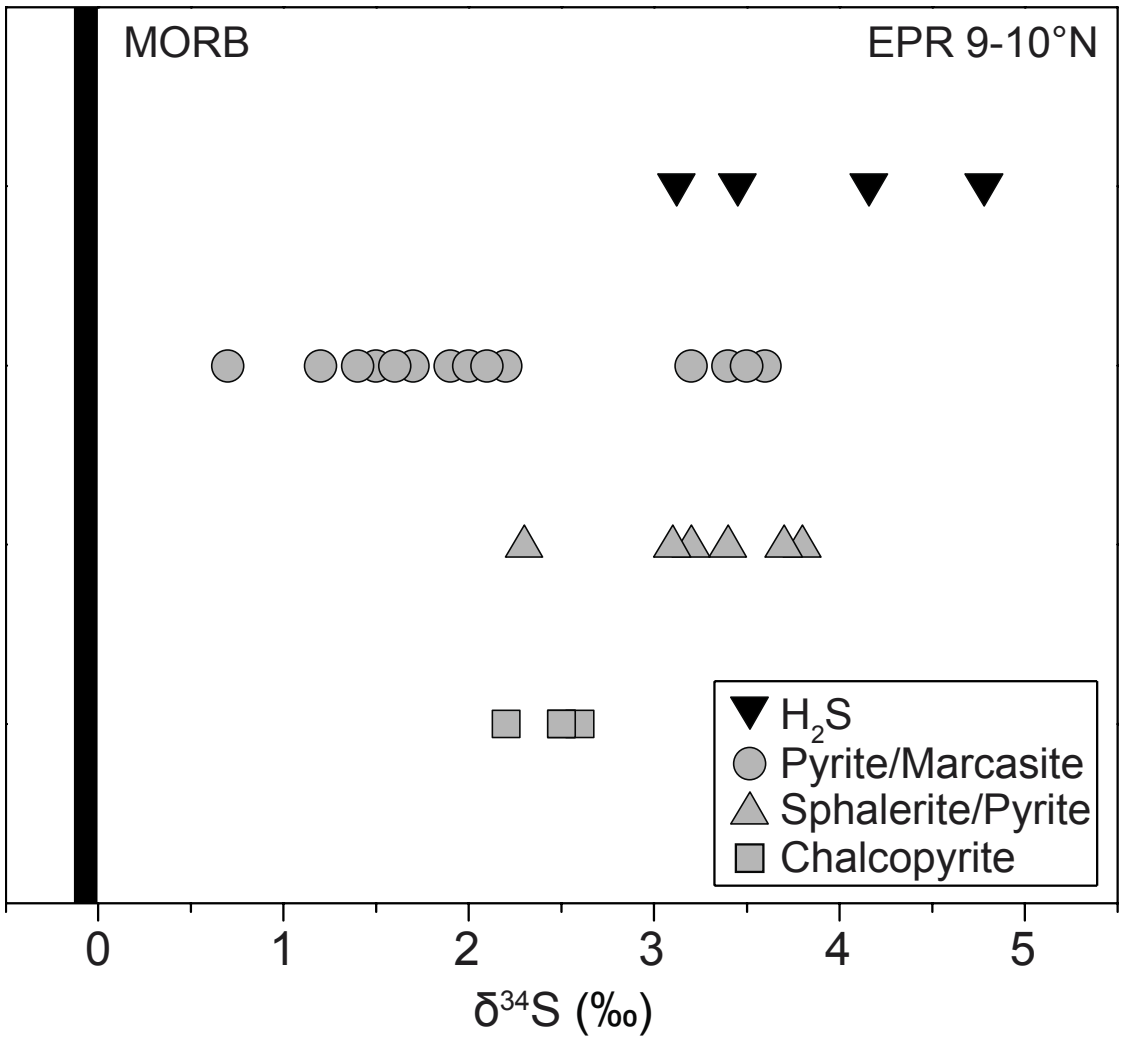

Fig. 2.9 Comparison of the $\delta^{34}S$ composition of metal sulfides and vent fluid H_2S from EPR 9-10°N compiled by *Rouxel et al.* [2008]. The vent H_2S is designated as black triangles whereas the mineral separates, pyrite/marcasite, sphalerite/pyrite, and chalcopyrite, are grey circles, triangles, and squares, respectively. The $\delta^{34}S$ compositional range of mid-ocean ridge basalt (MORB) is designated as the vertical black bar as determined by *Ono et al.* [2012]. Dissolved H_2S is enriched in the heavy isotopes of S relative to the majority of chimney metal sulfides. The pyrite separates has the largest range in $\delta^{34}S$ relative to all other metal sulfides, likely due to inherently slow exchange rates relative to other metal sulfides.

Figure 2.10

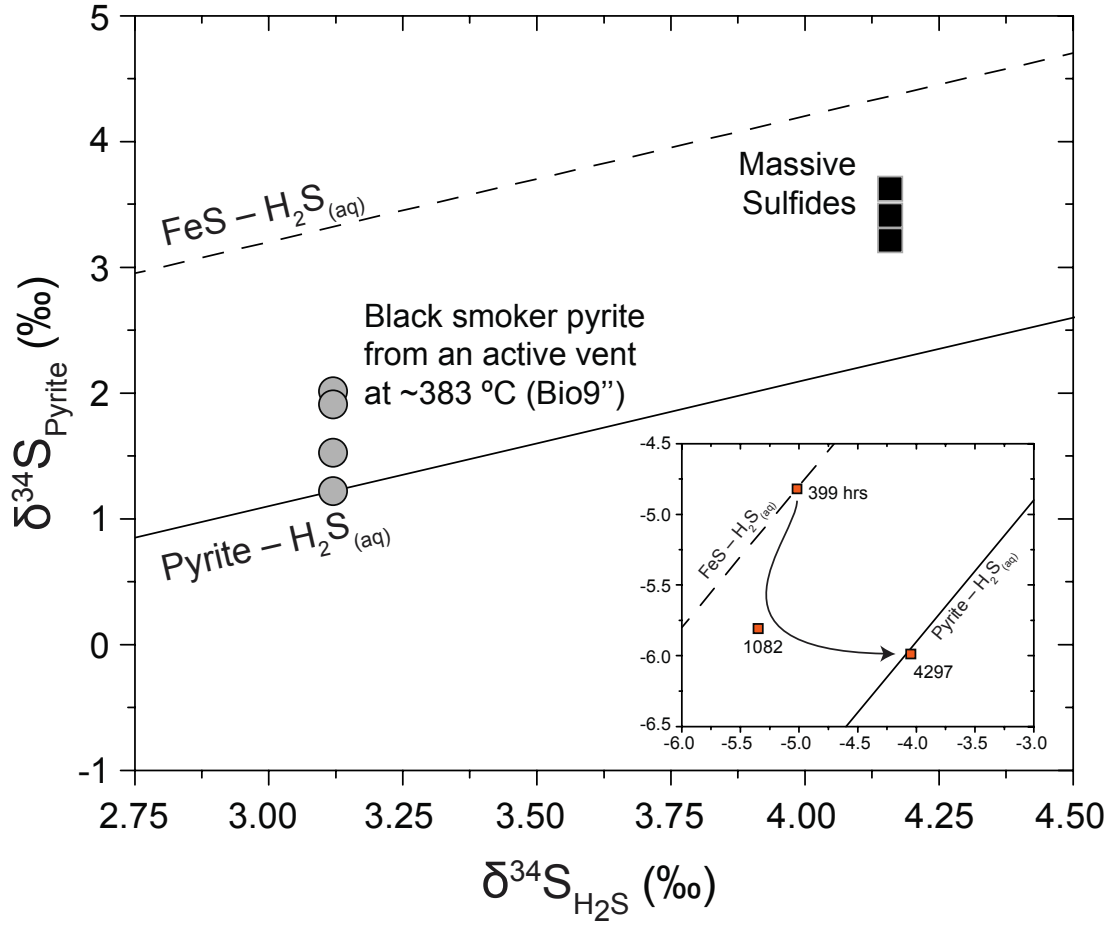

Fig. 2.10 Comparison of measured $\delta^{34}S$ fractionation data between vent fluids and coexisting pyrite from the East Pacific Rise (EPR) 9-10°N [*Rouxel et al.*, 2008] relative to the $^{34}S/^{32}S$ equilibrium fractionation between pyrite and H_2S determined from this study (solid line) and between FeS and H_2S (dashed line) from *Ohmoto and Rye* [1979]. Chimney pyrite recovered from the high temperature black smoker vent, Bio9'' (383°C), relative to the measured vent fluid (circles) exhibit fractionation data intermediate of FeS–H_2S and pyrite–H_2S equilibrium, but relatively close to the equilibrium fractionation between pyrite and H_2S at 350°C. The pyrite derived from the massive sulfide deposit relative to the average S isotope composition of H_2S venting from the high temperature fluids (squares) at EPR 9-10°N also exhibit fractionations intermediate between FeS–H_2S and pyrite–H_2S equilibrium. The inset figure depicts the time-series pyrite precipitation $^{34}S/^{32}S$ pyrite–H_2S fractionation data (orange symbols). These data demonstrate that the relatively early stages of reaction, 399 hours, resemble FeS–H_2S equilibrium and with time approach the equilibrium indicative of pyrite–H_2S. The S isotope data from this study are consistent with Fe isotope systematics and pyrite crystallographic observations, which suggest FeS as a likely precursor upon pyrite formation [*Syverson et al.*, 2013].

Chapter 3

Fe isotope fractionation during phase separation in the NaCl-H_2O System: An experimental study with implications for seafloor hydrothermal vents

Drew D. Syverson [a], Nicholas J. Pester [a], Paul Craddock [b], William E. Seyfried, Jr [a].

[a] *Department of Earth Sciences, University of Minnesota*
310 Pillsbury Drive, S.E., Minneapolis, Minnesota 55455

[b] *Department of Geophysical Sciences and Enrico Fermi Institute, University of Chicago*
5734 South Ellis Avenue, Chicago, Illinois 60637

Published in *Earth and Planetary Science Letters,* vol. 406 (2014), pp. 223-232

Used with permission of the co-authors and by Elsevier Publishing

3.0. Summary

Phase separation has been proposed as a possible mechanism contributing to the Fe isotopic composition of hydrothermal fluids at mid-ocean ridges. The uncertainty results largely from the emphasis on field data that can involve competing processes that obscure cause and effect of any one process. To better understand the potential significance of phase separation in the NaCl-Fe-H_2O system on Fe isotopic fractionation, temperature and pressure of a Fe-bearing NaCl fluid in a titanium flow reactor were carefully adjusted to produce vapor ± liquid ± halite, while the Fe isotope composition between coexisting phases was monitored. Two different P-T regions were emphasized (1): 424-420 °C, 35.2-31.5 MPa; and (2) 464-466 °C, 29.8-24.7 MPa. Both regions were chosen to simulate the range of physical conditions that are experienced by hydrothermal fluids at mid-ocean ridges (MORs). Decompression induced phase separation in both P-T regions

results in the vapor phase becoming enriched in the heavier isotopes of Fe, as the Fe/Cl ratio decreases. The coexisting NaCl-rich liquid phase remains essentially constant with respect to Fe/Cl ratio and Fe isotope composition. Coinciding with the lowest vapor chlorinity in the vapor-liquid stability field, the Fe isotope fractionation between the vapor and liquid ($10^3 ln\alpha^{56/54}_{V/L}$) reached a maximum value of +0.145 ‰. Subsequently, Fe isotope fractionation decreased upon transition into the vapor-halite stability field (P-T region 2). We infer that the observed Fe isotope fractionation between vapor ± liquid ± halite is caused by differences in Fe speciation among coexisting chloride-bearing phases. The experimental study confirms for the first time that measurable Fe isotopic variability can result from phase separation in high temperature hydrothermal systems. The species-dependent Fe isotope fractionation reported here is small relative to predicted mineral-mineral and mineral-fluid fractionations, especially if redox effects are involved as might occur during vent fluid-seawater mixing reactions and/or magmatic activity associated with seafloor eruptive episodes.

3.1. Introduction

Phase separation is a well-recognized process associated with high-temperature hydrothermal vent systems along the world's mid-ocean ridges. Many of these systems, especially those associated with the East Pacific Rise and Juan De Fuca Ridge, are strongly influenced by this process due to the relatively shallow emplacement of subseafloor magma chambers [*Butterfield et al.*, 1994; *Fontaine and Wilcock*, 2006; *Fontaine et al.*, 2007; *Fornari et al.*, 2012; *Lilley et al.*, 2003; *Seyfried et al.*, 2003; *Sohn et al.*, 1998; *Von Damm*, 2000; *Von Damm et al.*, 2003]. Accordingly, temperatures in

excess of 400°C and low to moderate pressures are common, causing seawater-derived fluids to separate into vapor and liquid phases in accordance with phase equilibria in the NaCl-H_2O system [*Bischoff and Pitzer*, 1985; *Bischoff and Rosenbauer*, 1986; *Bischoff and Pitzer*, 1989; *Driesner and Heinrich*, 2007]. Although numerous components in seawater and its hydrothermal equivalent have been shown to partition between the two coexisting aqueous phases [*Berndt and Seyfried*, 1990; *Berndt et al.*, 1996; *Foustoukos and Seyfried*, 2007; *Pester et al.*, 2014], the magnitude to which this occurs and whether the vapor or liquid becomes enriched or depleted in a particular element or isotope depends on an array of chemical and physical factors. For electrolytes, this is usually linked to temperature and pressure dependent variability in density and chloride concentration between coexisting phases. Moreover, where it was once thought that the P-T conditions affecting subseafloor hydrothermal systems would allow only the coexistence of liquid and vapor phases [*Bischoff and Pitzer*, 1985; 1989], magmatic activity linked to diking events and seafloor eruptions can cause hydrothermal fluid temperatures to achieve values sufficiently high that, at near seafloor pressure, halite can be predicted to form in association with chloride-poor vapor [*Berndt and Seyfried*, 1997; *Oosting and Von Damm*, 1996; *Von Damm*, 2000; *Von Damm et al.*, 2003].

Laboratory experiments have demonstrated that charged species, especially divalent transition metals such as Fe, show a strong preference for the liquid phase during vapor-liquid equilibria at elevated temperatures and pressures [*Bischoff and Rosenbauer*, 1987; *Pester et al.*, 2014; *Pokrovski et al.*, 2005]. At the same time, a number of field studies [*Beard et al.*, 2003; *Rouxel et al.*, 2008; *Sharma et al.*, 2001] have considered phase separation as a possible mechanism to induce Fe isotope fractionation in seafloor

hydrothermal vent fluids. Unfortunately, other processes at vents such as conductive cooling and metal sulfide precipitation can potentially obscure the effects of phase separation on the predictably small fractionation of transition metals and their isotopes [*Beard et al.*, 2003; *Polyakov and Soultanov*, 2011; *Rouxel et al.*, 2008]. Thus, samples from a series of hydrothermal experiments addressing the effects of phase separation on metal partitioning [*Pester et al.*, 2014] were analyzed for their Fe isotope composition. These experiments assess the direction and magnitude of Fe isotope fractionation in NaCl bearing multi-phase fluids. The experiments encompass the range of likely physical and chemical conditions in subseafloor at mid-ocean ridges, from vapor + liquid to vapor + halite systems, as shown in Figure 3.1. This is the first experimental study to evaluate the degree of Fe isotope fractionation during phase separation at elevated pressures and temperatures with implications for the chemical evolution of Fe isotopes in subaerial and submarine hydrothermal systems.

3.2. Experimental Methods

A hydrothermal flow-reactor was used to conduct phase separation experiments at temperatures in excess of 400°C and pressures between 22-40 MPa. The experimental design is largely similar to that previously used to determine the vapor-liquid partitioning of trace alkali elements and boron [*Foustoukos and Seyfried*, 2007], but with important modifications to facilitate analogous studies involving transition metals (Fig. 3.2) [*Pester et al.*, 2014]. Thus, the stainless steel hydrothermal flow-through reactor described in *Foustoukos and Seyfried* [2007] was replaced with a corrosion resistant Ti-alloy (Grade 7) reactor, with a volume (165 cm^3) sufficient to meet the sampling and analytical needs

of element and isotope partitioning studies in the two phase region of the NaCl-H_2O system.

Titanium capillary tubing (Grade 2) connects the reactor to external Ti valves and pumps. The only wetted stainless steel component in the system is the back-pressure regulator, which operates at ambient conditions. Temperature control is provided by external band heaters coupled with thermocouples placed externally in ports along the reactor, each of which is regulated by power-proportioning controllers. A Ti-sheathed (type E) monitors the temperature of the internal fluid phase(s), and these temperatures are reported herein. A computer-controlled, dome-loaded back-pressure regulator controls pressure with a high degree of precision (± 0.05 MPa). Thus, upon intersection of the two-phase boundary of the NaCl-H_2O system, the fully integrated temperature and pressure control systems permit acquisition of vapor and/or liquid phase samples with little or no perturbation to the operating pressure and temperature.

The input Ti-capillary tubing enters the reactor at the top and terminates in the middle of the reactor (Fig. 3.2), where the pressurized Fe-bearing source fluid instantaneously achieves the desired temperature, resulting in formation and efficient separation of vapor and liquid phases. The liquid phase is sampled from the bottom of the reactor through Ti-capillary tubing and a manually operated Ti valve, while the vapor phase is recovered from the top of the reactor after having passed through the back-pressure regulator. We performed a blank test with 0.05N HCl (trace-metal grade) at experimental conditions (temperature, pressure, and residence time) to quantify possible Fe contamination from stainless steel during sampling of acidic vapors through the back-pressure regulator. The test revealed sub μmolal concentrations of Fe, effectively ruling

out the back-pressure regulator as a source of Fe that could contaminate Fe-bearing vapor produced in the course of the experiment.

The fluid samples studied here represent a subset of those obtained throughout the course of a much broader and more comprehensive investigation of element partitioning in coexisting vapor and liquid pairs conducted by [*Pester et al.*, 2013; 2014]. Indeed, here we focus only on the partitioning of Fe and its isotopes during phase separation in the NaCl-Fe-H_2O system. Briefly, a NaCl solution (~900 mmol/kg) containing a fixed concentration of $FeCl_2$ (~2 mmol/kg) and constant Fe isotopic composition served as the source fluid for these experiments (Table 3.1). To avoid Fe precipitation at any time during the experiment, the source fluid was acidified (pH ~ 3), continuously purged with N_2, and rendered reducing by the addition of approximately 13 mmol/kg formic acid. Formic acid dissociates to $H_{2(aq)}$ and $CO_{2(aq)}$ at experimental conditions. The samples are indicated as single-phase, vapor, or liquid by the symbols S, V, and L, respectively (Table 3.1). Vapor and liquid samples were taken after steady state concentrations of $H_{2(aq)}$ and pH ($pH_{25°C}$) in the vapor were achieved at constant temperature and pressure, and where flow (0.1-0.3 ml/min) of the Fe bearing source solution was maintained constant for approximately 45 minutes.

The experimental conditions emphasize two different regions in P-T space. Both regions are designed to simulate the range of physical conditions that are experienced by hydrothermal fluids at mid-ocean ridges (MORs) [*Berndt and Seyfried*, 1997; *Oosting and Von Damm*, 1996; *Pester et al.*, 2014; *Pester et al.*, 2011; *Von Damm*, 2000]. Region 1 (Fig. 3.1, yellow circles) encompasses phase separation under moderate P-T conditions. Acquisition of vapor-liquid pairs in region 1 was achieved by decreasing the set pressure

on the backpressure regulator along the 425°C isotherm of the two-phase solvus. We note the slight decrease in the internal temperature of the cell with decreasing pressure as a physical response associated with the phase separation process. This occurred despite the fact that the external (control) temperature remained invariant [*Pester et al.*, 2014]. The magnitude of the effect, however, was sufficiently small so as not to warrant adjustment of the temperature control, which might have induced longer-term instability to the chemical and physical conditions of the system. While still within the two-phase area, temperature was increased to ~465 °C and pressure was decreased to approach halite stability indicated by region 2 (Fig. 3.1, green squares). Region 2 is broadly consistent with P-T conditions associated with basalt-hosted hydrothermal systems when impacted by subseafloor magmatic intrusions [*Fontaine et al.*, 2009; *Fornari et al.*, 2012; *Pester et al.*, 2014].

Considering the relatively large volume of the hydrothermal reactor (~165 ml), the flow rates were sufficiently slow to minimize chemical and physical perturbation while still maintaining pressure constant during sample removal. This is a necessary requirement to calculate trace element partition coefficients between coexisting phases in the NaCl-H_2O system [*Foustoukos and Seyfried*, 2007; *Pester et al.*, 2014] and applies to the objectives of the present study as well. Although the experimental setup allows for dynamic sampling of phases, the agreement between measured and predicted chloride composition of the vapor for coexisting vapor-liquid and vapor-halite phases at relevant temperatures and pressures [*Bischoff and Pitzer*, 1989; *Driesner and Heinrich*, 2007], indicates that equilibrium in the NaCl-H_2O system was achieved. We hypothesize that

this also applies to the distribution of Fe species owing to the well known sensitivity of Fe speciation to Cl variability at elevated temperatures and pressures.

Continuous sampling of vapor and liquid pairs was not possible for all of the pressure and temperature conditions ultimately achieved. The high salinity of the liquids produced at the lowest in-situ pressure conditions exceeds halite saturation upon cooling to ambient temperature. This would inhibit or preclude fluid flow through the sampling line due to precipitation. Accordingly, only vapor compositions are reportable for pressures below 33.6 MPa (Table 3.1).

Concentrations of all cations were measured by inductively-coupled plasma optical emission spectroscopy (ICP-OES) with uncertainties of approximately ±4 % (2σ). Chloride concentrations were analyzed by ion chromatography, with an uncertainty of ±1 % (2σ). In both cases, uncertainties in the reported data were based on replicate measurements, while using sample-standard-blank protocols. pH measurements were made by a Thermo-Ross electrode, which was calibrated between sampling intervals. Samples of dissolved $H_{2(aq)}$ were analyzed by gas chromatography with an accuracy better than ±1 % (2σ).

The Fe isotope composition of all fluid samples (Table 3.1) was determined in the Origins Laboratory in the Department of Geophysical Sciences at The University of Chicago. Analyses were carried out on a *Thermo Scientific Neptune* MC-ICP-MS. The methods for Fe purification and isotopic analysis follow those developed and described in *Dauphas et al.* [2009]. The Fe isotope composition representing the measured $^{56}Fe/^{54}Fe$ and $^{57}Fe/^{54}Fe$ ratios is given in delta notation as the ratio of the sample relative to the standard, $\delta^{i}Fe = 10^{3}*(R^{i/54}_{sample}/R^{i/54}_{IRMM\text{-}14} - 1)$, where IRMM-14 is the reference standard

and i = 56 or 57. The methods have been demonstrated to quantify the $^{56/54}$Fe isotopic composition with an accuracy of approximately ±0.03 ‰ at the 95 % confidence level. Measured δ^{57}Fe values follow the relationship ~3/2δ^{56}Fe expected for mass-dependent isotopic fractionation (Fig. 3.3); hereafter only variations in ^{56}Fe/^{54}Fe ratios will be discussed.

3.3. Results

3.3.1. Chemistry of single phase source fluid and vapors and liquids in P-T regions 1 and 2

Prior to initiation of phase separation, a fluid sample was taken to examine whether or not there existed a source of Fe other than that provided by the primary source fluid (2003 μmol Fe/kg, Table 3.1), in effect serving as a blank. Although close to the uncertainty of the Fe analysis of the primary source fluid, an increase in Fe of approximately 100 μmol/kg was observed (Table 3.1). The associated increase in δ^{56}Fe (Table 3.1) provides a more compelling case that a secondary source of Fe, likely from the Ti-reactor, mixed with the primary source fluid prior to phase separation.

Pressure decrease from the single phase condition (37.1 to 35.2 MPa; Fig. 3.1, Table 3.1) caused the fluid in the reactor to separate into compositionally distinct vapor and liquid phases (P-T region 1). In response, a clearly discernible decrease in the Fe/Cl ratio of the vapor was observed (Fig. 3.4, Table 3.1). The Fe/Cl ratio of the liquid remained essentially constant. This is expected from mass balance constraints following the metered addition of a NaCl-Fe-H_2O source fluid of fixed composition, together with the previously well-established partitioning behavior of Fe that strongly favors the liquid

[*Bischoff and Rosenbauer*, 1987; *Pester et al.*, 2014; *Pokrovski et al.*, 2005]. In P-T region 2 (464-466°C, 29.8-24.7 MPa), halite-vapor coexistence was achieved, which was associated with a sharp increase in the Fe/Cl ratio of the vapor (Fig. 3.4, Table 3.1).

3.3.2. Vapor – Liquid Fe isotope mass balance constraints for P-T region 1

Upon decompression and intersection of the two-phase vapor-liquid boundary, the Fe isotope composition of coexisting liquid and vapor becomes isotopically heavier with respect to the single phase fluid at elevated temperature and pressure (Table 3.1). As emphasized earlier, the source fluid continuously entering the reactor (0.1-0.3 ml/min) mixed with a chemically and isotopically distinguishable source of trace Fe derived from reaction of the acidic source solution with the Ti-reactor. Iron isotope mass balance calculations (Table 3.2), however, that take explicit account of the changing proportions of vapor and liquid reservoirs, and corresponding Fe concentration and δ^{56}Fe composition, indicate a constant δ^{56}Fe composition for the integrated system (vapor + liquid; Fig. 3.5) throughout the experiment. Thus, although two sources of Fe existed in the experimental system- one dominant, one trace, calculations suggest that the flux of each was sufficiently constant that steady state conditions were achieved. This test and corresponding result is a necessary requirement enabling unambiguous interpretation of temperature, pressure and compositional (i.e., dissolved Cl) effects on Fe isotope fractionation between coexisting vapor and liquid phases.

3.3.3. Fe isotopic fractionation between vapor-liquid and vapor-halite

All reported Fe isotopic fractionations between vapor-liquid and vapor-halite phases were calculated as $10^3 ln\alpha^{56/54}_{V/X}$, where the fractionation factor, $\alpha^{56/54}_{V/X}$, is equivalent to $(1+\delta^{56}Fe_{Vapor}/1000)/(1+\delta^{56}Fe_X/1000)$ and X represents either liquid or Fe-

bearing halite. We designate the Fe-bearing salt precipitate in the vapor-halite field (P-T region 2) as "Fe-bearing halite" owing to the uncertainty whether the Fe exists as a minor component in a solid solution of primarily halite, or as a distinct Fe-bearing mineral phase as a result of preferential exclusion from the halite lattice. Noted earlier, obtaining the conjugate liquids (or halite) associated with vapors evolved at pressures less than 33.6 MPa (and associated temperatures) was not possible. Thus, for the lowest chlorinity vapor of P-T region 1, and all vapors of region 2, the reported fractionation factors were calculated assuming the coexisting liquid/halite phase is isotopically equivalent to the integrated system (vapor + liquid) Fe isotopic composition (sample 3-8, P-T region 1, $\delta^{56}Fe_{System}$ = -0.241 ± 0.036‰, Table 3.1 and 3.2). This is a valid assumption at these extreme conditions because the mole fraction, X_{Fe}, of the liquid is essentially that of the integrated system as dictated by mass balance constraints (Table 3.2).

Isotope data from P-T region 1 indicate that within the two-phase field (Table 3.1), the initial Fe isotopic fractionation between higher-chlorinity vapor and liquid is statistically negligible (Fig. 3.6). The Fe isotopic fractionations between low-chlorinity vapors (≤332 mmol/kg [Cl^-], Table 3.1) and corresponding liquids, however, significantly deviate from zero, at the 95 % confidence level. The magnitude of Fe isotope fractionation continues to increase systematically with decompression. For example, at 420 °C and 31.5 MPa, the vapor phase is enriched relative to the liquid by +0.071 ± 0.048 ‰.

Samples associated with P-T region 2 reflect a continued decrease in vapor chlorinity relative to region 1 (Table 3.1). Interestingly, the vapor sampled at conditions closest to, but still outside of, the halite stability field exhibited the largest Fe isotopic

fractionation with $10^3 ln\alpha^{56/54}_{V/L} = +0.145 \pm 0.048$ ‰ (Fig. 3.7). Further decompression resulted in halite saturation (3-V11 and 3-V12, Fig. 3.1 and Table 3.1) and the isotopic fractionation between the vapor and halite decreased to $10^3 ln\alpha^{56/54}_{V/L} = +0.059 \pm 0.048$ ‰ (Fig. 3.7). This fractionation is of similar magnitude to that observed in P-T region 1.

The systematic changes in the magnitude of fractionation upon decompression (Fig. 3.6) and the virtually constant δ^{56}Fe of the integrated system in P-T region 1 (Fig. 3.5) is entirely consistent with constraints imposed by mass and isotope balance calculations precluding time series changes in the flux of Fe from secondary sources. The Fe and Cl poor vapor intrinsic to extreme phase separation (P-T region 2) might be expected to be most vulnerable to contamination effects, but this does not appear to be the case.

3.4. Discussion

3.4.1. Fe isotopic fractionation between vapor and liquid

The experimental approach produced a relatively large reservoir of Fe in the liquid and halite phases relative to the vapor phase during isothermal decompression (Tables 3.1 and 3.2). As a result, chemical and isotopic fractionation was expressed predominantly in the vapor phase. We infer attainment of equilibrium Fe isotope fractionation between coexisting vapor-liquid (halite) pairs in the present experiment by analogy with the well constrained NaCl-H_2O system [*Bischoff and Pitzer*, 1985; *Bischoff and Rosenbauer*, 1986; *Pester et al.*, 2014], and by the time needed to achieve equilibrium recognized from other experimental studies of partitioning of metals between vapor and liquid at similar temperatures, pressures, and bulk chloride compositions

[*Berndt and Seyfried*, 1990; *Bischoff and Rosenbauer*, 1987; *Foustoukos and Seyfried*, 2007; *Pester et al.*, 2014].

3.4.2. Speciation dependent Fe isotopic fractionation

During progressive decompression, the chemical composition of vapor and liquid pairs changed dramatically owing to constraints imposed by phase equilibria in the NaCl-Fe-H_2O system (Table 3.1, Fig. 3.4). Fe solubility and the relative distribution of aqueous Fe-bearing species are undoubtedly sensitive to these compositional changes [*Bischoff and Rosenbauer*, 1987; *Ding and Seyfried*, 1992; *Testemale et al.*, 2009]. Although it is well known that Fe isotope fractionation is significantly affected by redox (Fe^{2+}-Fe^{3+} exchange in a hydrated aqueous species [*Hill et al.*, 2010]), this is unlikely at any stage in the present experiment, owing to the highly reducing conditions imposed by the presence of H_2(aq) from decomposition of formic acid. In effect, redox was buffered throughout the experiment, such that valence change of iron to the ferric species was not possible.

We interpret the observed fractionation of Fe isotopes, especially in the two-phase vapor-liquid region (Figs. 3.6 and 3.7), to reflect differences in the abundance and coordination chemistry of Fe species between vapor and coexisting liquid or halite. Variability in solution composition and solvent properties of vapor and liquid as a function of P, T, and composition can result in significant differences in the type and number of coordinated ligands, such as Cl^- or H_2O, complexed to Fe. For example, *Testemale et al.* [2009] used in-situ X-ray absorption data (25 to 450°C and 0.5 to 12m chloride molality), to confirm the octahedral coordination of Fe^{2+}-chloro complexes, $[FeCl_x(H_2O)_{6-x}]^{2-x}$ where x = 0 – 2, at relatively low temperatures and dissolved chloride concentrations. The coordination changes, however, to a high-order tetrahedral Fe^{2+}-

chloro complex, $[FeCl_4]^{2-}$, upon increasing temperature (>300°C) at similar dissolved chloride concentrations. It is possible that tetrahedral Fe^{2+}-chloro complexes at high temperature are not limited to $[FeCl_4]^{2-}$, which may require an associated cation (e.g., Na^+) to achieve charge neutrality, but might also include the neutral Fe^{2+}-aquo-chloro complex $[FeCl_2(H_2O)_2]^0$ at low dissolved chloride concentrations. An example of this is provided by XAS studies at supercritical conditions of cobalt chloro-complexes, which indicate that at a similar high temperature (440 °C), the water rich $[CoCl_2(H_2O)_2]^0$ complex is predominant at low salinity (< 0.5 mol/kg dissolved Cl), whereas $[CoCl_4]^{2-}$ exists at high salinity [*Liu et al.*, 2011]. Similar spectroscopic studies for the $NiCl_2$-, $CdCl_2$-, and $MnCl_2$-H_2O-NaCl systems [*Bazarkina et al.*, 2010; *Migdisov et al.*, 2011; *Tian et al.*, 2014; *Tian et al.*, 2012] also exhibit increasing degrees of stability for tetrahedrally coordinated metal aquo-chloro-complexes at elevated temperatures with analogous changes in coordination chemistry as a function of dissolved chloride concentration. We infer from previous spectroscopic efforts that the chloride-rich liquid phase is dominated by $[FeCl_4]^{2-}$ at all times of the experiment, whereas the vapor phase is susceptible to changes in the relative abundance of $[FeCl_2(H_2O)_2]^0$ and $[FeCl_4]^{2-}$ upon progressive phase separation. The more volatile H_2O-rich Fe-species, $[FeCl_2(H_2O)_2]^0$, partitions preferentially into the vapor phase, which the Fe isotopic data indicate to be enriched with the heavy isotopes of Fe relative to $[FeCl_4]^{2-}$. Where the coexisting vapor and liquid have the most distinct differences in Cl concentration upon phase separation, we expect the Fe isotopic fractionation to reach a maximum. This is best demonstrated by the largest fractionation of Fe isotopes between the vapor and liquid just prior to halite stability (Fig. 3.7), likely a result of the extreme compositional difference between vapor

and liquid with respect to Cl and Fe (Tables 3.1 and 3.2). To date there are no known independent experimental data for Fe speciation in such dilute low-density vapors at similar P-T-X conditions from which we can predict quantitatively the distribution of Fe-species in the vapor for our study and validate our hypothesis.

Theoretical-based calculations [*Hill and Schauble*, 2008; *Hill et al.*, 2010; *Hill et al.*, 2009; *Schauble et al.*, 2001] have confirmed that differences in coordination chemistry between Fe chloro- and aquo- complexes can result in Fe isotopic fractionation comparable in magnitude to reduction-oxidation processes, where the predicted fractionation between two Fe-bearing phases/species is described by the difference in reduced partition function ratios, β (i.e. isotopic affinity), $10^3 ln\alpha_{a/b}=10^3(\ln\beta_a-\ln\beta_b)$. These predictions for the Fe isotope system are in agreement with other chemical systems, which demonstrate that transition metal-bearing aqueous complexes rich in water (O bonds) preferentially incorporate heavy isotopes relative to coexisting chloride-rich aqueous species [*Black et al.*, 2011; *Fujii et al.*, 2011; *Seo et al.*, 2007]. Furthermore, as the number of chloro ligands increases in the inner-coordination sphere of a transition metal bearing aqueous complex, the degree of enrichment of heavy isotopes decreases. These theoretical constraints suggest that the tentative Fe-bearing chloro complex (e.g., $[FeCl_2(H_2O)_2]^0$ in the vapor phase) is isotopically heavy, while the incorporation of chloride in the inner coordination sphere of Fe complexes (e.g., $[FeCl_4]^{2-}$ in the liquid phase) reduces the degree of isotopic enrichment of the heavy isotopes of Fe in the liquid. This effect creates a positive Fe isotopic fractionation between the vapor and liquid as observed in our experiments (Figs. 6 and 7). We note that current theoretical models predicting Fe isotopic fractionation among aqueous Fe-complexes have not explicitly

considered temperatures above 300 °C, nor has the complete range of coordination chemistries of transition metal-bearing complexes in vapor and liquid phases been fully evaluated.

3.4.3. Fe isotopic fractionation between vapor and halite

Further decompression in our experiments resulted in halite saturation (P-T region 2, Fig. 3.1), which is associated with an abrupt decrease in the Fe isotope fractionation between coexisting phases (Fig. 3.7). In spite of the low chloride concentration at this range of P-T conditions, Fe transfer to the vapor phase is still evident on both an absolute and chloride-normalized basis (Table 3.1, Fig. 3.4) [*Pester et al.*, 2014]. Enhanced partitioning of Fe into the vapor and the decreased δ^{56}Fe composition of the vapor cannot be interpreted unambiguously in the absence of additional information about the fate of Fe as a component in halite or an associated Fe-chloride phase. Mass balance constraints indicate that over 99% of Fe is sequestered in the solid phase in the vapor-halite stability field. The isotopically buffered Fe-bearing halite may fractionate with a vapor that changes in Fe isotopic composition due to differences in the speciation and abundance of various Fe-bearing complexes in the vapor phase and possibly due to differences in the physical state and speciation of Fe in halite, giving rise to the small Fe isotopic fractionation observed between vapor and Fe-bearing halite. These hypotheses, however, require further experimental testing, not only at pressure and temperature extrema that give rise to halite-vapor coexistence, but also with initial Fe concentrations sufficient to produce and retrieve product minerals to investigate their chemical, mineralogical, and isotopic properties. Experiments of this sort would also benefit from additional

theoretical studies combined with spectroscopic data to quantify differences in the speciation of Fe in the across a range of P-T-X conditions.

3.4.4. Implications for the Fe isotopic distribution during phase separation at deep sea vents

The range of metal isotopic compositions measured in seafloor hydrothermal fluids is not correlated with chlorinity in a way that can be immediately recognized [*Anbar and Rouxel*, 2007; *Beard et al.*, 2003; *John et al.*, 2008; *Rouxel et al.*, 2004; *Rouxel et al.*, 2008; *Sharma et al.*, 2001]. Accordingly, other physiochemical processes such as near seafloor metal sulfide precipitation and alteration of the oceanic crust have been proposed to explain the metal isotope signature of hydrothermal vent fluids at mid-ocean ridges. Our experimental results indicate that phase separation imparts a small but measureable Fe isotopic fractionation between coexisting phases in the NaCl-Fe-H_2O system at temperature and pressure conditions relevant to mid-ocean ridge hydrothermal systems. On the basis of our experimental data, magmatic eruptions or diking events in the shallow oceanic crust [*Von Damm*, 2000; *Von Damm et al.*, 2003] are expected to produce chloride-depleted vapors which are preferentially enriched in the heavy isotopes of Fe. These first experimental data hold promise that stable metal isotope studies may be used as indicators of fluid phase separation. Measurement of the Fe isotope composition of vapors and brines from active vents might be one way to demonstrate this, but so too would be the Fe isotopic analysis of vent chimney minerals from active and fossil expressions of these systems (i.e. differences in source Fe isotopic composition upon sulfide mineralization).

3.5. Conclusions

This experimental study demonstrates statistically significant Fe isotope fractionation, $10^3 ln\alpha^{56/54}_{V/L}$ = +0.059 to +0.145 ‰, between coexisting vapor and liquid/halite phases in the NaCl-Fe-H_2O system at elevated temperatures (424-466 °C) and pressures (35.2-24.7 MPa). The mechanism controlling the observed Fe isotopic fractionation is uncertain, but most likely involves formation of aqueous complexes of Fe in the vapor phase that are distinctly different in composition and coordination compared to those in the coexisting liquid, Fe-bearing halite phase, or associated discreet Fe mineral.

The species dependent fractionation is inferred from the correlation in the magnitude of the Fe isotopic fractionation with chemical composition (e.g. Fe/Cl and H_2O/NaCl ratio) of the vapor and liquid phases (P-T region 1). We interpret the isotopically-heavy vapor to be dominated by the neutrally-charged and variably hydrated Fe-chloro species in tetrahedral coordination (e.g., $[FeCl_2(H_2O)_2]^0$), whereas the coexisting isotopically-light liquid comprises primarily chloride-rich Fe-species (e.g., $[FeCl_4]^{2-}$). The experimentally determined Fe isotopic fractionation is in agreement with predictions based on theoretical calculations in the NaCl-Fe-H_2O system. Our experimental data extend the P-T range considered in these calculations to those appropriate for submarine hydrothermal systems and so can be used to inform theoretical model development and to broaden the geochemical interpretations thereof.

Although phase separation of Fe-bearing NaCl fluids produces a small Fe isotopic fractionation between vapors and liquids/halite, the experimental data reported here provide important insight on the potential effects of aqueous complex formation and

mineralization on fractionation of non-traditional metal isotopes at otherwise poorly supported chemical and physical conditions. It is through the combination of experimental data and theoretically-based molecular dynamic simulations, however, that is key to understanding the quantitative controls on transition metal behavior and metal isotope fractionation during extreme phase separation events associated with the temporal evolution of hydrothermal vent fluids at mid-ocean ridges.

Table 3.1: Measured chemical and Fe isotopic composition of experimental fluids with extent of phase separation

	Sample Name	T (°C)	P (MPa)	*pH	ρ (g/cm^3)	[H_2]	[Cl]	[Fe]	Fe/Cl (um/mm)	δ^{56}Fe (‰)	2σ (‰)	δ^{57}Fe (‰)	2σ (‰)	$10^3 ln\alpha^{56}$Fe (Vapor-X)	2σ (‰)
Single Phase	3-S1	22	0.1	3.00	1.054	-	927	2003	2.16	-0.389	0.028	-0.560	0.074	-	-
	3-S2	426	37.1	2.84	0.514	12.7	910	2114	2.32	-0.292	0.032	-0.439	0.061	-	-
Region 1	3-V3	424	35.2	2.76	0.458	14.2	662	1361	2.06	-0.229	0.028	-0.344	0.074	0.009	0.040
	3-L3	424	35.2	4.40	0.702	-	2686	6767	2.52	-0.238	0.028	-0.346	0.074		
	3-V4	423	34.7	2.79	0.417	15.0	481	928	1.93	-0.204	0.032	-0.304	0.061	0.044	0.045
	3-L4	423	34.7	4.60	0.750	-	3269	8224	2.52	-0.248	0.032	-0.359	0.061		
	3-V5	422	34.2	2.76	0.374	15.6	332	573	1.72	-0.184	0.032	-0.281	0.061	0.063	0.045
	3-L5	422	34.2	5.24	0.772	-	3565	9434	2.65	-0.247	0.032	-0.330	0.061		
	3-V6	421	33.6	2.74	0.331	15.3	212	330	1.56	-0.174	0.028	-0.282	0.074	0.071	0.040
	3-L6	421	33.6	5.12	0.797	-	3901	9633	2.47	-0.245	0.028	-0.384	0.074		
	3-V8	420	31.5	2.72	0.248	-	69	79	1.14	-0.170	0.032	-0.236	0.061	0.071[a]	0.048
Region 2	3-V10	464	29.8	2.57	0.135	-	13	21	1.62	-0.096	0.032	-0.132	0.061	0.145[a]	0.048
	3-V11	465	26.8	2.43	0.113	-	9.5	28	2.95	-0.176	0.028	-0.193	0.074	0.065[a]	0.046
	3-V12	466	24.7	2.30	0.100	-	9.1	33	3.63	-0.182	0.032	-0.261	0.061	0.059[a]	0.048

(*) pH measured on quench; (-) indicates components that were not analyzed. "S", "V", and "L" represent single phase solution, vapor, and conjugate liquid, respectively. [a] Calculated from mass balance constraints imposed by the Fe isotopic composition of the integrated system (vapor + liquid), $\delta^{56}Fe_{System}$ = - 0.241 ±0.036 ‰ (see text and Table 2). Dissolved H_2 and Cl concentrations are reported in mmol/kg whereas dissolved Fe concentration is reported in umol/kg.

Table 3.2: Mass balance of Fe for the phase separated NaCl-Fe-H_2O system in P-T region 1

Sample	T (°C)	P (MPa)	$M_{(Liquid)}$ [a]	$X_{Fe(Liquid)}$ [b]	$\delta^{56}Fe_{Liquid}$ (‰)	$\delta^{56}Fe_{Vapor}$ (‰)	$\delta^{56}Fe_{System}$ (‰)
3-3 (V-L)	424	35.2	0.20	0.55	-0.238	-0.229	-0.234
3-4 (V-L)	423	34.7	0.24	0.73	-0.248	-0.204	-0.236
3-5 (V-L)	422	34.2	0.29	0.87	-0.247	-0.184	-0.239
3-6 (V-L)	421	33.6	0.35	0.94	-0.245	-0.174	-0.241
3-8 (V)	420	31.5	0.47	0.99 [c]	-0.241 [d]	-0.170	-0.241

"V" and "L" represent vapor and conjugate liquid sampled from the experiment, respectively. [a] The mass fraction of the liquid accumulating in the reactor, $M_{(Liquid)}$, relative to the vapor + liquid system with decompression is calculated by taking into account flow, density of the source solution, vapor, and liquid phase, and Cl partitioning data upon phase separation of the source solution. [b] The mole fraction of Fe in the liquid relative to the vapor + liquid system, $X_{Fe(Liquid)}$, is determined from measured Fe concentration data coupled with the mass fraction data. [c] Only the vapor was measured for sample 3-8, therefore the Cl and Fe concentrations of the conjugate liquid were predicted from the vapor-liquid isotherm at 420 °C [*Driesner and Heinrich*, 2007] and from Fe partitioning data [*Pester et al.*, 2014], respectively. [d] Calculated from mass balance constraints imposed by the Fe isotopic composition of the integrated system (sample 3-6 (V-L), $\delta^{56}Fe_{System}$ = - 0.241 ±0.036 ‰). Uncertainty for measured vapor and liquid Fe isotopic compositions, $\delta^{56}Fe$, ranges from 0.028-0.032 ‰ (2σ).

Figure 3.1

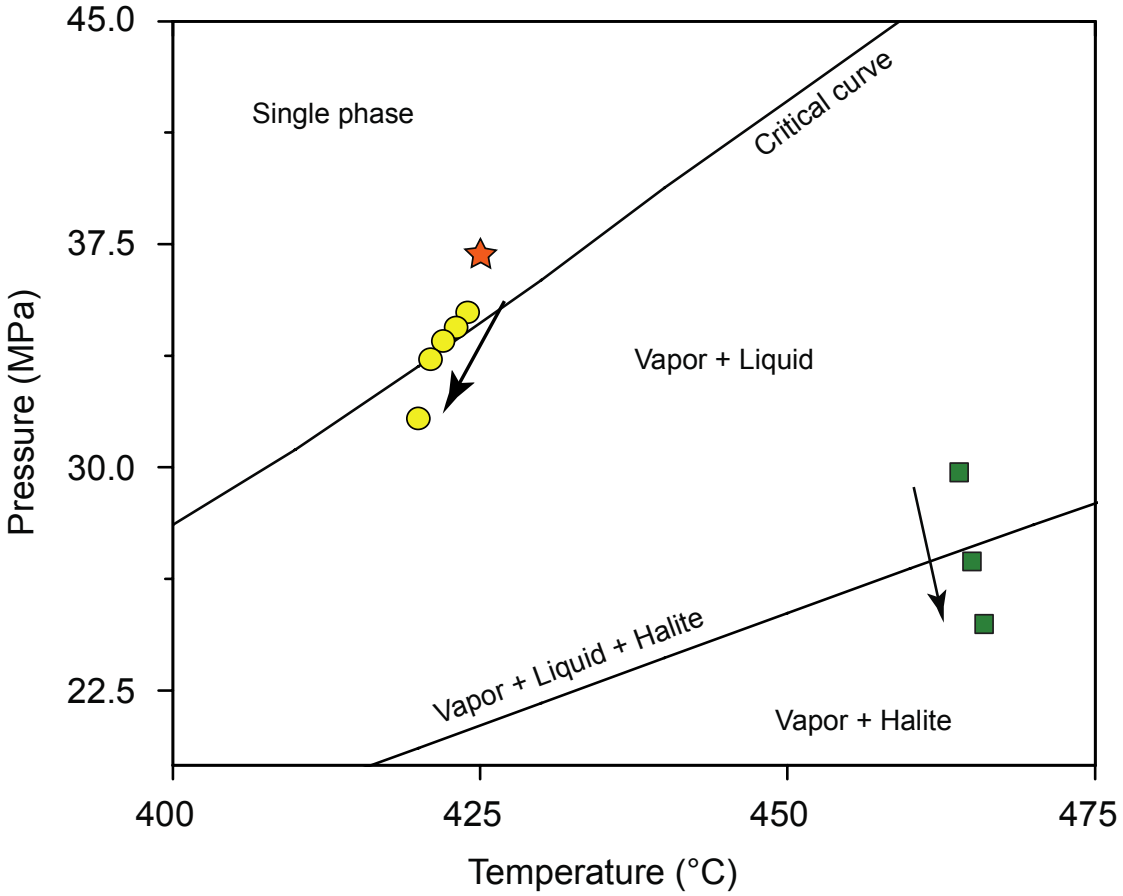

Fig. 3.1 Phase diagram for the NaCl-Fe-H_2O system illustrating the stability fields of vapor-liquid and vapor-halite in comparison with the one-phase system. The initial experimental condition for the single phase Fe- and NaCl-bearing fluid is shown as the orange star. Samples from P-T region 1, yellow circles, intersect the critical curve and move further into to the stability field of vapor + liquid coexistence. Samples from P-T region 2, green squares, transition from vapor + liquid coexistence into the stability field of vapor + halite coexistence. Uncertainties in phase boundaries delineating vapor-liquid-halite stability domains relative to experimental measurements are difficult to quantify unambiguously. This results in part from constraints imposed by limitations in the accuracy of the temperature and pressure measurements inherent to the present experiments (see text), while the position of the phase boundaries reflects errors in the experimental data and statistical models used to describe the phase stability relations in the system H_2O-NaCl (see *Driesner and Heinrich* [2007]). It should also needs to be noted that the formation of $HCl°_{(aq)}$ and aqueous Fe species in the low chloride vapors may have an effect on phase equilibria.

Figure 3.2

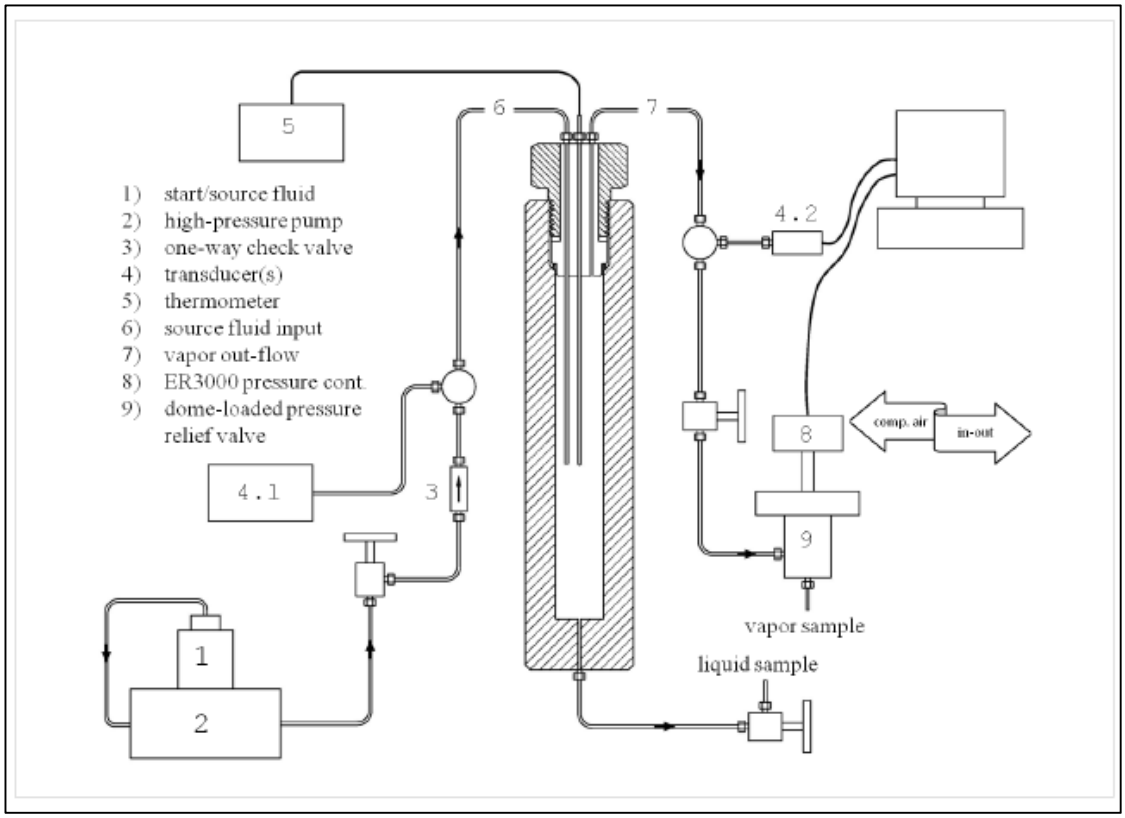

Fig. 3.2 Schematic illustration of the flow-through Ti-alloy reactor (165 cm^3) used for the phase separation experiments in this study [*Pester et al.*, 2014] and supporting temperature and pressure control systems. In practice, pressurized Fe-bearing NaCl source solution (1) is added to the reactor at a flow rate of 0.1 to 0.3 ml/min through Ti-capillary tubing by a portal in the reactor (6), where phase separation of the source fluid is induced by the set temperature and pressure conditions. Outlet flow occurs by vapor release and sampling (7), facilitated by Ti-capillary tubing and back-pressure regulator (9). Sampling of the denser liquid phase is achieved through a manually operated Ti-valve external to the reactor.

Figure 3.3

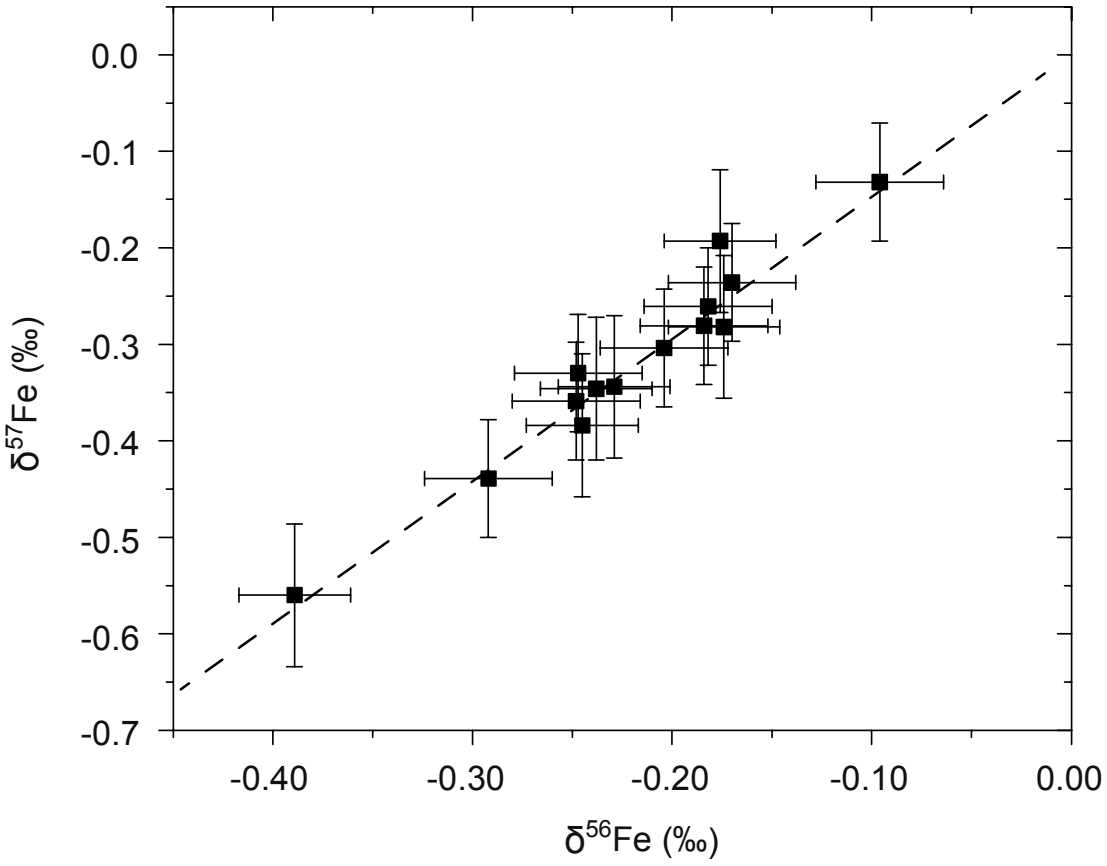

Fig. 3.3 $\delta^{57}Fe$ versus $\delta^{56}Fe$ for all samples measured in this Fe isotope study. Errors bars represent 2σ standard deviation for $\delta^{57}Fe$ and $\delta^{56}Fe$, ~0.07 and ~0.03 ‰, respectively. The Fe isotope data correlate well with the theoretical mass-dependent fractionation line describing the fractionation relationship between $\delta^{57}Fe$ and $\delta^{56}Fe$ (dashed line, slope = ~1.47).

Figure 3.4

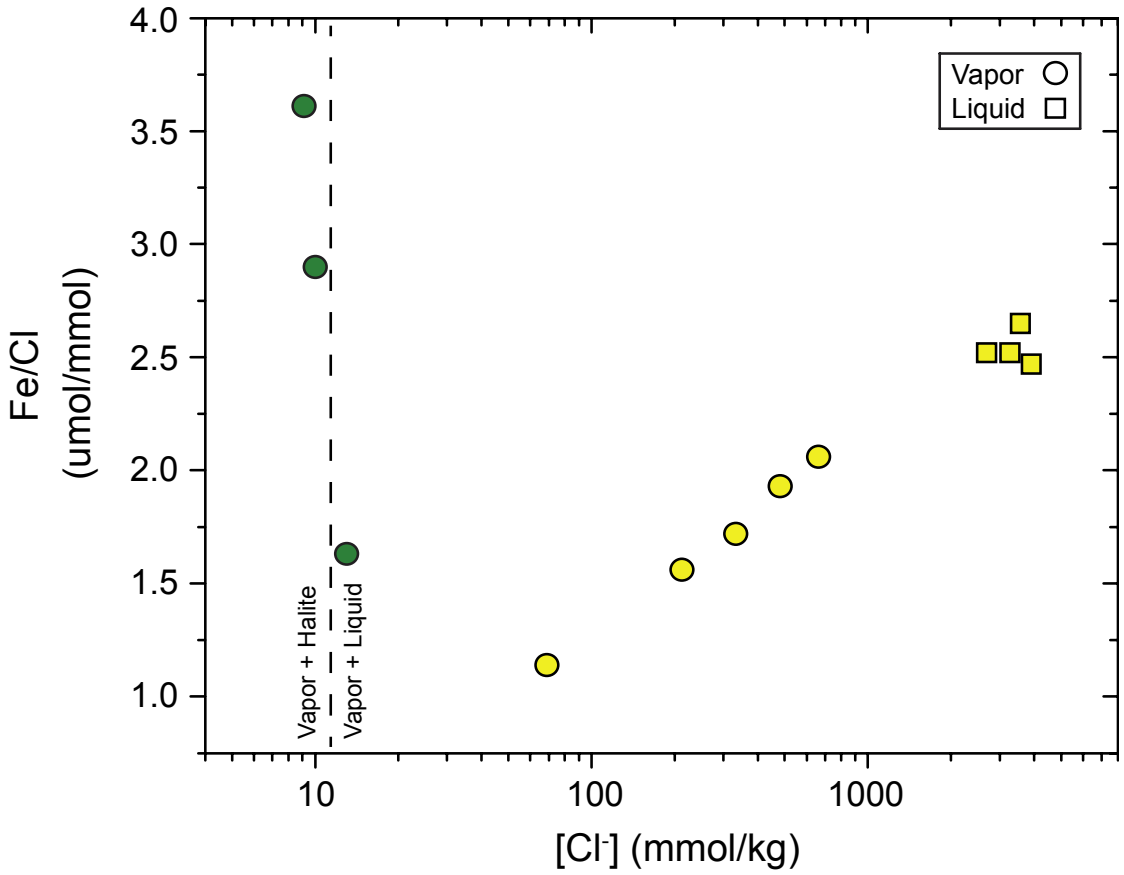

Fig. 3.4 Fe/Cl ratio of vapor and coexisting liquid in P-T region 1 as a function of chlorinity during decompression (yellow symbols: circles and squares are vapors and liquids, respectively). The dashed line indicates the stability limits of liquid and halite coexistence with the vapor phase. Note that the Fe/Cl ratio of the vapor decreases dramatically, while the coexisting liquid samples remain invariant, i.e. the vapors become increasingly depleted in Fe during decompression in the vapor-liquid stability field. However, upon the approach and transition into the vapor-halite field, P-T region 2 (green symbols: sampled vapors only), the vapor Fe/Cl ratio increases greatly despite the continued decrease in vapor chlorinity attending decompression, an opposite trend relative to the Fe/Cl ratio in P-T region 1.

Figure 3.5

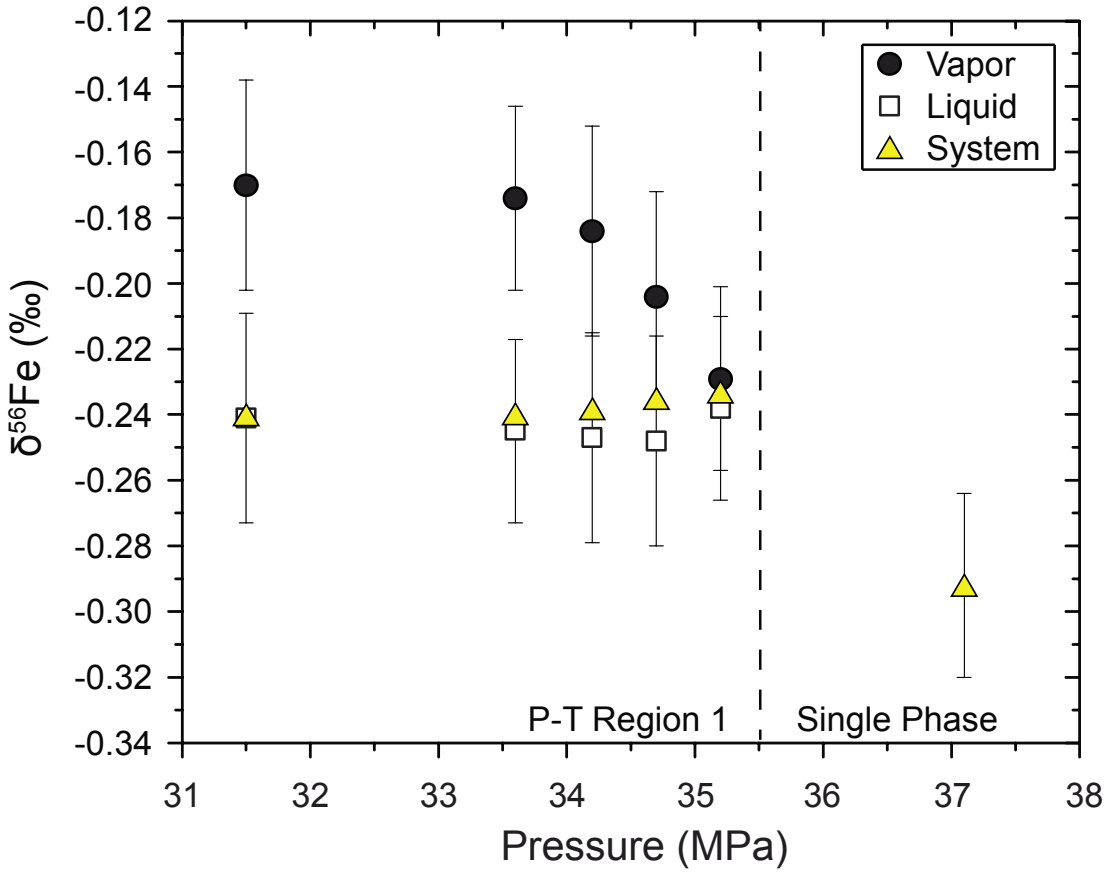

Fig. 3.5 Fe isotope compositions, δ^{56}Fe (‰), of the vapor, liquid, and integrated system (vapor + liquid, calculated from mass balance constraints described in Table 2) as a function of pressure at ~424-420 °C. The vapor phase becomes increasingly isotopically heavy during decompression whereas the isotopic composition of the liquid phase is lighter relative to the integrated system and the vapor phase. The Fe isotope composition of the liquid progressively approaches the integrated isotopic composition as $X_{Fe(Liquid)}$ increases with decompression (Table 3.2). The system Fe isotope composition remains constant throughout P-T region 1, indicating a steady state isotope composition of the system during flow, phase separation of the source fluid, and sampling of the vapor and liquid phases. Error bars shown for the vapor and liquid Fe isotope composition upon decompression represent analytical uncertainties between 0.028 and 0.032 ‰ (2σ).

Figure 3.6

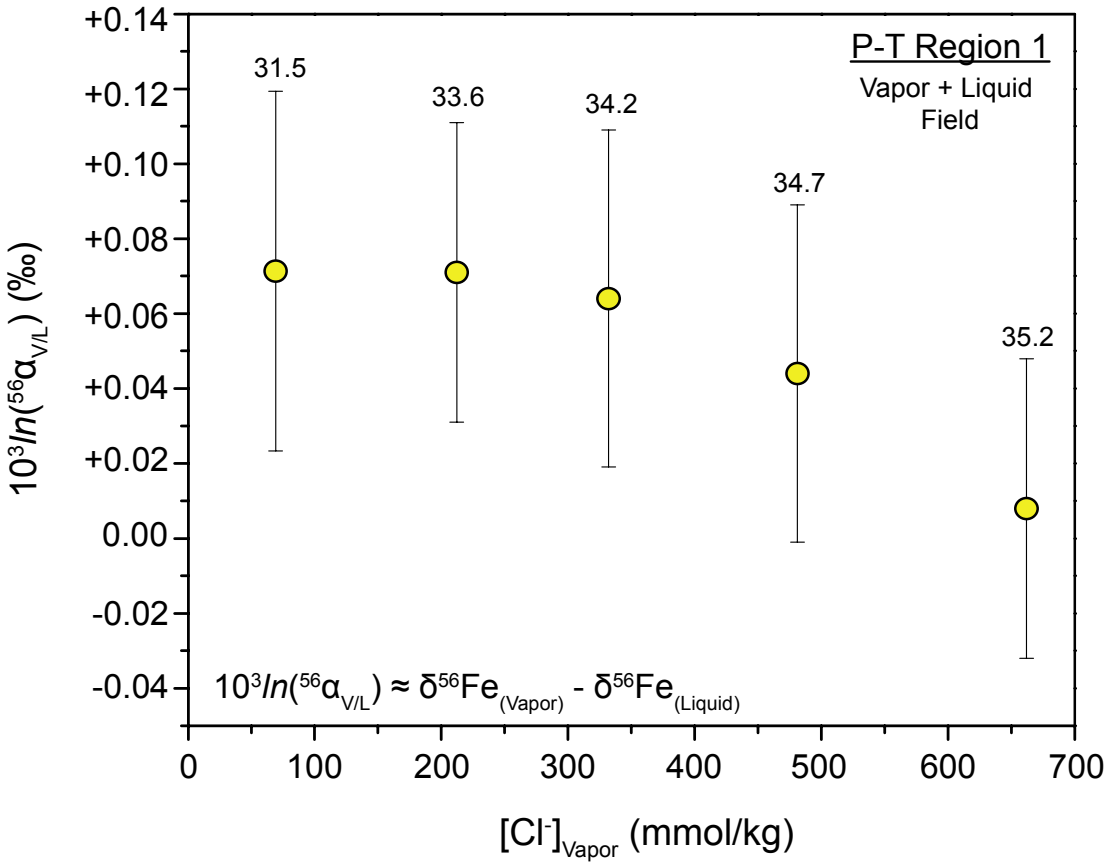

Fig. 3.6 Fe isotope fractionation between vapors and liquids during decompression in P-T region 1 (~424-420 °C); the pressure, in MPa, at each sampling point is indicated. Note that the final Fe isotope fractionation between vapor and liquid at 31.5 MPa is determined by calculating the liquid isotope composition from mass constraints imposed by the $\delta^{56}Fe$ of the integrated system (vapor + liquid) obtained in P-T region 1 (sample 3-8: $\delta^{56}Fe_{System}$ = -0.241 ±0.036 ‰; Table 3.1 and 3.2). The difficulty in sampling the high chloride liquid at this final condition requires this approach (see text). The increase in the Fe isotope fractionation with decompression (i.e. lower chloride in the vapor) suggests that differences in speciation of Fe between the vapor and liquid phases play a major role in the observed Fe isotope fractionation shown. The error bars are the experimental uncertainties of 0.040 to 0.048 ‰ (2σ).

Figure 3.7

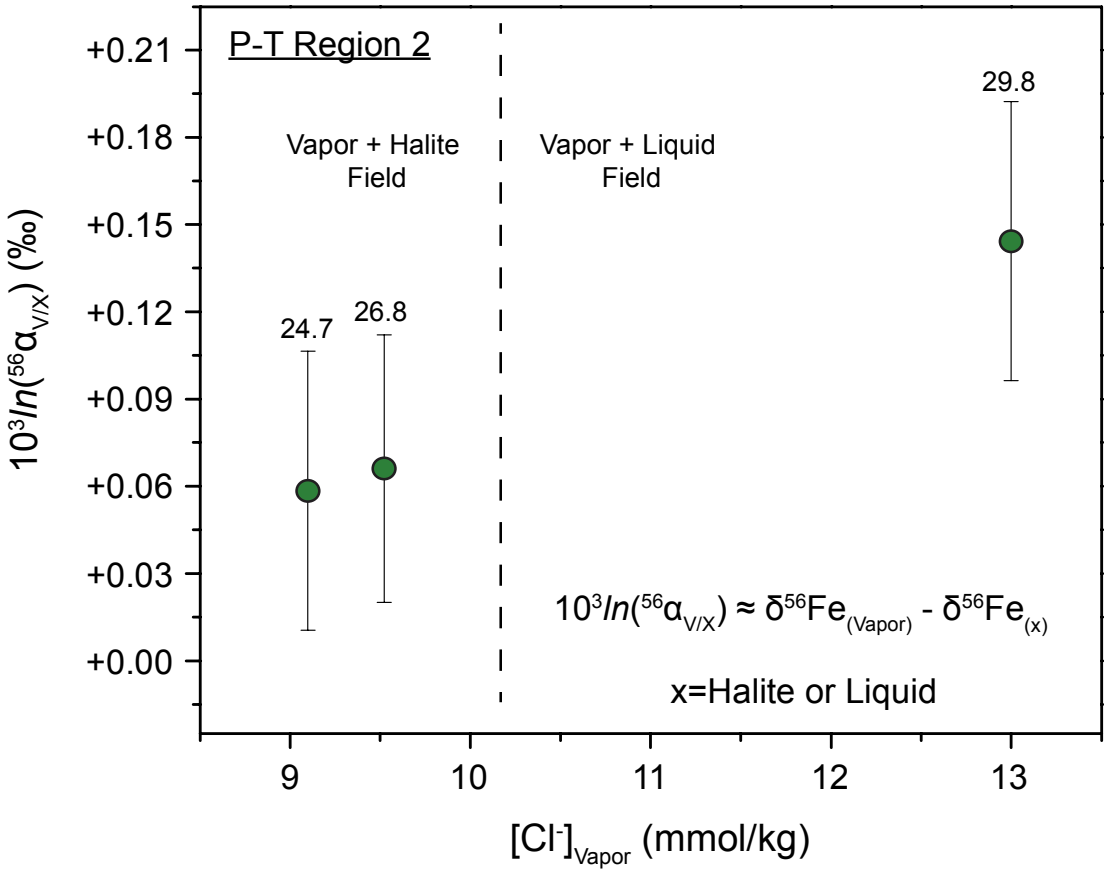

Fig. 3.7 The NaCl-Fe-H_2O system transitions from the vapor-liquid field to the vapor-halite field during decompression (P-T region 2) as indicated by the dashed line representing the phase boundary; pressure in MPa is shown above each error bar. Concomitantly, the Fe isotope fractionation between the sampled vapors and the liquid and halite phases decreases to similar values observed in P-T region 1. The Fe isotope composition of the liquid and halite used for the reported fractionation was calculated assuming that the majority of Fe remained in the non-vapor phase and it had the $\delta^{56}Fe$ equivalent to the integrated system in P-T Region 1 (sample 3-8: $\delta^{56}Fe_{System}$ = -0.241 ±0.036 ‰, Tables 3.1 and 3.2). The error bars are the experimental uncertainties 0.046 to 0.048 ‰ (2σ).

References

Agarwala, U., C. E. Rees, and H. G. Thode (1965), Sulfur isotope effects in the hydrogen ion decomposition of thiosulfate, *Canadian Journal of Chemistry*, *43*, 9.

Alt, J. C., and D. A. H. Teagle (1999), The uptake of carbon during alteration of ocean crust, *Geochimica et Cosmochimica Acta*, *63*, 1527-1535.

Alt, J. C., and W. C. Shanks (2011), Microbial sulfate reduction and the sulfur budget for a complete section of altered oceanic basalts, IODP Hole 1256D (eastern Pacific), *Earth and Planetary Science Letters*, *310*(1-2), 73-83.

Anbar, A. D., and O. Rouxel (2007), Metal Stable Isotopes in Paleoceanography, *Annu. Rev. Earth Planet. Sci.*, *35*, 29.

Anbar, A. D., A. A. Jarzecki, and T. G. Spiro (2005), Theoretical investigation of iron isotope fractionation between Fe(H2O)63+ and Fe(H2O)62+: Implications for iron stable isotope geochemistry, *Geochimica et Cosmochimica Acta*, *69*(4), 825-837.

Angert, A., S. Rachmilevith, E. Barkan, and B. Luz (2003), Effects of photorespiration, the cytochrome pathway, and the alternative pathway on the triple isotopic composition of atmospheric O2, *Global Biogeochemical Cycles*, *17*(1), 14.

Balan, E., P. Cartign, M. Blanchard, D. Cabaret, M. Lazzeri, and F. Mauri (2009), Theoretical investigations of the anomalous equilibrium fractionation of multiple sulfur isotopes during adsoprtion, *Earth and Planetary Science Letters*, *284*, 88-93.

Bazarkina, E. F., G. S. Pokrovski, A. V. Zotov, and J. L. Hazemann (2010), Structure and stability of cadmium chloride complexes in hydrothermal fluids, *Chemical Geology*, *276*, 1-17.

Beard, B. L., C. M. Johnson, and K. Von Damm (2003), Iron isotope constraints on Fe cycling and mass balance in oxygenated Earth oceans, *Geology*, *31*, 3.

Beard, B. L., R. M. Handler, M. M. Scherer, L. Wu, A. D. Czaja, A. Heimann, and C. M. Johnson (2010), Iron isotope fractionation between aqueous ferrous iron and goethite, *Earth and Planetary Science Letters*, *295*(1-2), 241-250.

Bennett, S. A., O. Rouxel, K. Schmidt, D. Garbe-Schönberg, P. J. Statham, and C. R. German (2009), Iron isotope fractionation in a buoyant hydrothermal plume, 5°S Mid-Atlantic Ridge, *Geochimica et Cosmochimica Acta*, *73*(19), 5619-5634.

Berndt, M. E., and W. E. Seyfried (1990), Boron, bromine, and other trace elements as clues to the fate of chlorine in mid-ocean rdige vent fluids, *Geochimica et Cosmochimica Acta*, *54*, 10.

Berndt, M. E., and W. E. Seyfried (1997), Calibration of Br/Cl fractionation during subcritical phase separation of seawater: Possible halite at 9 to 10°N East Pacific Rise, *Geochimica et Cosmochimica Acta*, *61*, 5.

Berndt, M. E., W. E. Seyfried, and J. W. Beck (1988), Hydrothermal alteration processes at mid-ocean ridge: Experimental and theoretical constraints from Ca and Sr exchange reactions and Sr isotopic ratios, *Journal of Geophysical Research*, *93*, 4573-4583.

Berndt, M. E., R. R. Seal, W. C. Shanks, and W. E. Seyfried (1996), Hydrogen isotope systematics of phase separation in submarine hydrothermal systems: Experimental calibration and theoretical models, *Geochimica et Cosmochimica Acta*, *60*(9), 9.

Berner, R. A. (1970), Sedimentary pyrite formation, *American Journal of Science*, *268*, 1-23.

Bethke, C. M. (2006), The Geochemist Workbench Release 6.0 Reaction Modeling Guide. A User Guide to React and Gtplot. University of Illinois.

Bigeleisen, J., and M. G. Mayer (1947), Calculation of Equilibrium Constants for Isotopic Exchange Reactions, *The Journal of Chemical Physics*, *15*(5), 261.

Bischoff, J. L., and K. S. Pitzer (1985), Phase relations and adiabats in boiling seafloor geothermal systems, *Earth and Planetary Science Letters*, *75*, 11.

Bischoff, J. L., and R. J. Rosenbauer (1986), The system NaCl-H2O: Relations of vapor-liquid near the critical temperature of water and of vapor-liquid-halite from 300° to 500°C, *Geochimica et Cosmochimica Acta*, *50*, 7.

Bischoff, J. L., and R. J. Rosenbauer (1987), Phase separation in seafloor geothermal systems: An experimental study of the effects on metal transport, *American Journal of Science*, *287*, 25.

Bischoff, J. L., and K. S. Pitzer (1989), Liquid-Vapor Relations for the System NaCl-H2O: Summary of the P-T-x Surface from 300° to 500°C, *American Journal of Science*, *289*, 31.

Black, J. R., A. Kavner, and E. A. Schauble (2011), Calculation of equilibrium stable isotope partition function ratios for aqueous zinc complexes and metallic zinc, *Geochimica et Cosmochimica Acta*, *75*(3), 769-783.

Blanchard, M., F. Poitrasson, M. Méheut, M. Lazzeri, F. Mauri, and E. Balan (2009), Iron isotope fractionation between pyrite (FeS2), hematite (Fe2O3) and siderite (FeCO3): A first-principles density functional theory study, *Geochimica et Cosmochimica Acta*, *73*(21), 6565-6578.

Blanchard, M., F. Poitrasson, M. Méheut, M. Lazzeri, F. Mauri, and E. Balan (2012), Comment on "New data on equilibrium iron isotope fractionation among sulfides: Constraints on mechanisms of sulfide formation in hydrothermal and igneous systems" by V.B. Polyakov and D.M. Soultanov, *Geochimica et Cosmochimica Acta*, *87*, 356-359.

Blanchard, M., et al. (2014), Reduce partition function ratios of iron and oxygen in goethite, *Geochimica et Cosmochimica Acta*.

Bluth, G. J., and H. Ohmoto (1988), Sulfide-Sulfate Chimneys on the East Pacific Rise, 11°N and 13°N Latitudes. Part II: Sulfur Isotopes, *Canadian Mineralogist*, *26*, 10.

Bondarenko, G. V., and Y. E. Gorbaty (1997), In situ Raman spectroscopic study of sulfur-saturated water at 1000 bar between 200 and 500°C, *Geochimica et Cosmochimica Acta*, *61*(7), 7.

Borrok, D. M., R. Wanty, W. Ridley, R. Wolf, P. Lamothe, and M. Adams (2007), Separation of copper, iron, and zinc from complex aqueous solutions for isotopic measurement, *Chemical Geology*, *242*(3-4), 400-414.

Borrok, D. M., R. B. Wanty, W. I. Ridley, P. J. Lamothe, B. A. Kimball, P. L. Verplanck, and R. L. Runkel (2009), Application of iron and zinc isotopes to track the sources and mechanisms of metal loading in a mountain watershed, *Applied Geochemistry*, *24*, 1270-1277.

Butler, I. B., and D. Rickard (2000), Framboidal pyrite formation via the oxidation of iron (II) monosulfide by hydrogen sulphide, *Geochimica et Cosmochimica Acta*, *64*, 2665-2672.

Butler, I. B., M. E. Böttcher, D. Rickard, and A. Oldroyd (2004), Sulfur isotope partitioning during experimental formation of pyrite via the polysulfide and hydrogen sulfide pathways: implications for the interpretation of sedimentary and hydrothermal pyrite isotope records, *Earth and Planetary Science Letters*, *228*(3-4), 495-509.

Butler, I. B., C. Archer, D. Vance, A. Oldroyd, and D. Rickard (2005), Fe isotope fractionation on FeS formation in ambient aqueous solution, *Earth and Planetary Science Letters*, *236*(1-2), 430-442.

Butterfield, D. A., R. E. McDuff, M. J. Mottl, M. D. Lilley, J. E. Lupton, and G. J. Massoth (1994), Gradients in the composition of hydrothermal fluids from the Endeavour segment vent field: Phase separation and brine loss, *Journal of Geophysical Research*, *99*(B5), 22.

Chu, X., H. Ohmoto, and D. Cole (2004), Kinetics of sulfur isotope exchange between aqueous sulfide and thiosulfate involving intra- and intermolecular reactions at hydrothermal conditions, *Chemical Geology*, *211*(3-4), 217-235.

Cole, D. R., H. Ohmoto, and A. C. Lasaga (1983), Isotopic exchange in mineral-fluid systems. I. Theoretical evaluation of oxygen isotopic exchange accompanying surface reactions and diffusion, *Geochimica et Cosmochimica Acta*, *47*, 1681-1693.

Cole, D. R., M. J. Mottle, and H. Ohmoto (1987), Isotopic exchange in mineral-fluid systems. II. Oxygen and hydrogen isotopic investigation of the experimental basalt-seawater system*, *Geochimica et Cosmochimica Acta*, *51*, 1523-1538.

Criss, R. E. (1999), *Principles of stable isotope distribution*, 254 pp., Oxford University Press, New York.

Czamanske, G. K., and R. O. Rye (1974), Experimentally determined sulfur isotope fractionations between sphalerite and galena in the temperature range 600 to 275 degrees C *Economic Geology*, *69*, 17-25.

Czarnacki, M., and S. Hałas (2012), Ab initio calculations of sulfur isotope fractionation factor for H2S in aqua–gas system, *Chemical Geology*, *318-319*, 1-5.

Dauphas, N., A. Pourmand, and F.-Z. Teng (2009), Routine isotopic analysis of iron by HR-MC-ICPMS: How precise and how accurate?, *Chemical Geology*, *267*, 9.

Dauphas, N., M. Roskosz, E. E. Alp, D. C. Golden, C. K. Sio, F. L. H. Tissot, M. Y. Hu, J. Zhao, L. Gao, and R. V. Morris (2012), A general moment NRIXS approach to the determination of equilibrium Fe isotopic fractionation factors: Application to goethite and jarosite, *Geochimica et Cosmochimica Acta*, *94*, 254-275.

Delacour, A., G. L. Fruh-Green, and S. M. Bernasconi (2008), Sulfur mineralogy and geochemistry of serpentinites and gabbros of the Atlantis Massif (IODP Site U1309), *Geochimica et Cosmochimica Acta*, *72*, 5111-5127.

Ding, K., and W. E. Seyfried (1992), Determination of Fe-Cl complexing in the low pressure supercritical region (NaCl fluid): Iron solubility constraints on pH on subseafloor hydrothermal fluids, *Geochimica et Cosmochimica Acta*, *56*, 11.

Driesner, T., and C. A. Heinrich (2007), The system H2O–NaCl. Part I: Correlation formulae for phase relations in temperature–pressure–composition space from 0 to 1000°C, 0 to 5000bar, and 0 to 1 XNaCl, *Geochimica et Cosmochimica Acta*, *71*(20), 4880-4901.

Ellis, A. J., and W. Giggenbach (1971), Hydrogen sulphide ionization and sulphur hydrolysis in temperature solution, *Geochimica et Cosmochimica Acta*, *35*, 247-260.

Farquhar, J., and B. A. Wing (2003), Multiple sulfur isotopes and the evolution of the atmosphere, *Earth and Planetary Science Letters*, *213*(1-2), 1-13.

Farquhar, J., D. Johnston, B. Wing, K. S. Habicht, D. E. Canfield, S. Airieau, and M. H. Thiemens (2003), Multiple sulphur isotopic interpretations of biosynthetic pathways: implications for biological signatures in the sulphur isotope record, *Geobiology*, *1*, 27-36.

Fontaine, F. J., and W. S. D. Wilcock (2006), Dynamics and storage of brine in mid-ocean ridge hydrothermal systems, *Journal of Geophysical Research*, *111*(B6).

Fontaine, F. J., W. S. D. Wilcock, and D. A. Butterfield (2007), Physical controls on the salinity of mid-ocean ridge hydrothermal vent fluids, *Earth and Planetary Science Letters*, *257*, 13.

Fontaine, F. J., W. S. D. Wilcock, D. I. Foustoukos, and D. A. Butterfield (2009), A Si-Cl geothermometer for the reaction zone of high-temperature, basaltic-hosted mid-ocean ridge hydrothermal systems, *Geochemistry, Geophysics, Geosystems*, *10*.

Fornari, D., et al. (2012), The East Pacific Rise Between 9°N and 10°N: Twenty-Five Years of Integrated, Multidisciplinary Oceanic Spreading Center Studies, *Oceanography*, *25*(1), 18-43.

Foustoukos, D. I., and W. E. Seyfried (2007), Trace element partitioning between vapor, brine and halite under extreme phase separation conditions, *Geochimica et Cosmochimica Acta*, *71*(8), 2056-2071.

Fujii, T., F. Moynier, N. Dauphas, and M. Abe (2011), Theoretical and experimental investigation of nickel isotopic fractionation in species relevant to modern and ancient oceans, *Geochimica et Cosmochimica Acta*, *75*(2), 469-482.

German, C., and W. E. Seyfried (2014), Hydrothermal Processes, in *Treatise on Geochemistry*, edited, pp. 192-227.

Graham, U. M., and H. Ohmoto (1994), Experimental study of formation mechanisms of hydrothermal pyrite*, *Geochimica et Cosmochimica Acta*, *58*, 2187-2202.

Grootenboer, J., and H. P. Schwarcz (1969), Experimentally determined sulfur isotope fractionations between sulfide minerals, *Earth and Planetary Science Letters*, *7*, 4.

Guilbaud, R., I. B. Butler, and R. M. Ellam (2011a), Abiotic pyrite formation produces a large Fe isotope fractionation, *Science*, *332*(6037), 1548-1551.

Guilbaud, R., I. B. Butler, R. M. Ellam, and D. Rickard (2010), Fe isotope exchange between Fe(II)aq and nanoparticulate mackinawite (FeSm) during nanoparticle growth, *Earth and Planetary Science Letters*, *300*(1-2), 174-183.

Guilbaud, R., I. B. Butler, R. M. Ellam, D. Rickard, and A. Oldroyd (2011b), Experimental determination of the equilibrium Fe isotope fractionation between and FeSm (mackinawite) at 25 and 2°C, *Geochimica et Cosmochimica Acta*, *75*(10), 2721-2734.

Haar, L., J. S. Gallagher, and G. S. Kell (1984), *NBS/NRC Steam Tables.* , Hemisphere publishing McGraw-Hill, New York.

Helgeson, H. C., D. H. Kirkham, and G. C. Flowers (1981), Theoretical prediction of thermodynamic properties of aqueous electrolytes at high pressures and temperatures. IV. Calculation of activity coefficients, osmotic coefficients, and apparent molal and standard and relative partial molal properties to 600°C and 5kb, *American Journal of Science*, *281*, 67.

Helgeson, H. C., J. M. Delany, H. W. Nesbitt, and D. K. Bird (1978), Summary and critique of the thermodynamic properties of rock-forming minerals, *American Journal of Science*, *278A*, 1-229.

Hill, P. S., and E. A. Schauble (2008), Modeling the effects of bond environment on equilibrium iron isotope fractionation in ferric aquo-chloro complexes, *Geochimica et Cosmochimica Acta*, *72*, 19.

Hill, P. S., E. A. Schauble, and E. D. Young (2010), Effects of changing solution chemistry on Fe3+/Fe2+ isotope fractionation in aqueous Fe-Cl solution, *Geochimica et Cosmochimica Acta*, *74*, 20.

Hill, P. S., E. A. Schauble, A. Shahar, E. Tonui, and E. D. Young (2009), Experimental studies of equilibrium iron isotope fractionation in ferric aquo–chloro complexes, *Geochimica et Cosmochimica Acta*, *73*(8), 2366-2381.

Ho, P. C., D. A. Palmer, and R. H. Wood (2000), Conductivity measurements of dilute aqueous LiOH, NaOH, and KOH solution to high temperatures and pressures using a flow-through cell, *J. Phys. Chem B*, *104*, 12084-12089.

Hulston, J. R., and H. G. Thode (1965), Variations in the S^{33}, S^{34}, and S^{36} Contents of Meteorites and Their Relation to Chemical and Nuclear Effects, *Journal of Geophysical Research*, *70*(14), 9.

Jamieson, J. W., B. Wing, M. Hannington, and J. Farquhar (2006), Evaluating Isotopic Equilibrium Among Sulfide Mineral Pairs in Archean Ore Deposits: Case Study from the Kidd Creek VMS Deposit, Ontario, Canada, *Economic Geology*, *101*, 1055-1061.

Jamieson, J. W., B. Wing, J. Farquhar, and M. Hannington (2013), Neoarchaean seawater sulphate concentrations from sulphur isotopes in massive sulphide ore, *Nature Geoscience*, *6*, 61-64.

John, S. G., O. J. Rouxel, P. R. Craddock, A. M. Engwall, and E. A. Boyle (2008), Zinc stable isotopes in seafloor hydrothermal vent fluids and chimneys, *Earth and Planetary Science Letters*, *269*(1-2), 17-28.

Johnson, J. W., E. H. Oelkers, and H. C. Helgeson (1992), SUPCRT92: a software package for calculating the standard molal thermodynamic properties of minerals, gases, aqueous species, and reactions from 1 to 5000 bar and 0 to 1000C, *Computers & Geosciences*, *7*, 899-947.

Johnston, D. T., J. Farquhar, and D. E. Canfield (2007), Sulfur isotope insights into microbial sulfate reduction: When microbes meet models, *Geochimica et Cosmochimica Acta*, *71*(16), 3929-3947.

Johnston, D. T., J. Farquhar, B. A. Wing, A. J. Kaufman, D. E. Canfield, and K. S. Habicht (2005), Multiple sulfur isotope fractionations in biological systems: A case study with sulfate reducers and sulfur disproportionators, *American Journal of Science*, *305*, 15.

Kajiwara, Y., and H. R. Krouse (1971), Sulfur isotope partitioning in metallic sulfide systems, *Canadian Journal of Earth Sciences*, *8*(11), 11.

Kajiwara, Y., H. R. Krouse, and A. Sasaki (1969), Experimental study of sulfur isotope fractionation between coexistent sulfide minerals, *Earth and Planetary Science Letters*, *7*, 6.

Kerridge, J. F., R. M. Haymon, and M. Kastner (1983), Sulfur isotope systematics at the 21°N site, East Pacific Rise, *Earth and Planetary Science Letters*, *66*, 9.

Kiyosu, Y. (1973), Sulfur isotopic fractionation among sphalerit, galena, and sulfide ions, *Geochemical Journal*, *7*, 191-199.

Kong, X.-Z., B. M. Tutolo, and M. O. Saar (2013), DBCreate: A SUPCRT92-based program for producing EQ3/6, TOUGHREACT, and GWB thermodynamic databases at user-defined T and P, *Computers & Geosciences*, *51*, 415-417.

Lennie, A. R., S. A. T. Redfern, P. F. Schofield, and D. J. Vaughan (1995), Synthesis and Rietveld crystal structure refinement of mackinawite, tetragonal FeS, *Mineralogical Magazine*, *59*, 677-683.

Levin, N. E., T. D. Raub, N. Dauphas, and J. M. Eilier (2014), Triple-oxygen-isotope variations in sedimentary rocks, *Geochimica et Cosmochimica Acta*.

Lilley, M. D., D. A. Butterfield, J. E. Lupton, and E. J. Olson (2003), Rapid changes in hydrothermal vent chemistry, *Nature*, *422*, 3.

Liu, W., S. Borg, D. Testemale, B. E. Etschmann, J. L. Hazemann, and J. Brugger (2011), Speciation and thermodynamic properties of cobalt chloride complexes in hydrothermal fluids at 35-440C and 600 bar: An in-situ XAS study, *Geochimica et Cosmochimica Acta*, *75*, 21.

Luther, G. (1991), Pyrite synthesis via polysulfide compounds, *Geochimica et Cosmochimica Acta*, *55*, 2839-2849.

Mahon, K. I. (1996), The New "York" Regression: Application of an Improved Statistical Method to Geochemistry, *International Geology Review*, *38*(4), 293-303.

Matsuhisa, Y., J. R. Goldsmith, and R. N. Clayton (1978), Mechanisms of hydrothermal recrystallization of quartz at 250 C and 15 kbar, *Geochimica et Cosmochimica Acta*, *42*, 173-182.

McDermott, J. M., S. Ono, M. K. Tivey, J. S. Seewald, W. C. Shanks, and A. R. Solow (2015), Identification of sulfur sources and isotopic equilibria in submarine hot-springs using multiple sulfur isotopes, *Geochimica et Cosmochimica Acta*, *160*, 169-187.

Migdisov, A. A., D. Zezin, and A. E. Williams-Jones (2011), An experimental study of Cobalt (II) complexation in Cl- and H2S-bearing hydrothermal solutions, *Geochimica et Cosmochimica Acta*, *75*, 4065-4079.

Miller, M. F. (2002), Isotopic fractionation and the quantification of 17O anomalies in the oxygen three-isotope system: an appraisal and geochemical significance, *Geochimica et Cosmochimica Acta*, *66*(11), 8.

Murowchick, J. B., and H. L. Barnes (1986), Marcasite precipitation from hydrothermal solutions, *Geochimica et Cosmochimica Acta*, *50*, 14.

Murowchick, J. B., and H. L. Barnes (1987), Effects of temperature and degree of supersaturation on pyrite morphology, *American Mineralogist*, *72*, 9.

Nakai, N. (1970), Pyrite - SO42- Experimental Exchange? (In Japanese), *The Geochemical Society of Japan*.

Northrop, D. A., and R. N. Clayton (1966), Oxygen isotope fractionations in systems containing dolomite, *Journal of Geology*, *74*, 174-196.

Oana, S., and H. Ishikawa (1966), Sulfur isotopic fractionation between sulfur and sulfuric acid in the hydrothermal solution of sulfur dioxide, *Geochemical Journal*, *1*, 45-50.

Oduro, H., A. Kamyshny, W. Guo, and J. Farquhar (2011), Multiple sulfur isotope analysis of volatile organic sulfur compounds and their sulfonium precursors in coastal marine environments, *Marine Chemistry*, *124*(1-4), 78-89.

Oelkers, E. H., and H. C. Helgeson (1991), Calculation of activity coefficients and degrees of formation of neutral ion pairs in supercritical electrolyte solutions, *Geochimica et Cosmochimica Acta*, *55*, 1235-1251.

Ohmoto, H., and R. O. Rye (1979), Isotopes of sulfur and carbon, in *Geochemistry of Hydrothermal Ore Deposits*, edited by H. L. Barnes, pp. 509-567, J Wiley and Sons.

Ohmoto, H., and A. C. Lasaga (1982), Kinetics of reactions between aqueous sulfates and sulfides in hydrothermal systems, *Geochimica et Cosmochimica Acta*, *46*, 18.

Ohmoto, H., and M. Goldhaber (Eds.) (1997), *Sulfur and carbon isotopes*, 94 pp., John Wiley & Sons, New York.

Ohmoto, H., K. Hayashi, and Y. Kajiwara (1994), Experimental study of the solubilities of pyrite in NaCl-bearing aqueous solutions at 250-350°C, *Geochimica et Cosmochimica Acta*, *58*, 2169-2185.

Ono, S., W. C. Shanks, O. J. Rouxel, and D. Rumble (2007), S-33 constraints on the seawater sulfate contribution in modern seafloor hydrothermal vent sulfides, *Geochimica et Cosmochimica Acta*, *71*(5), 1170-1182.

Ono, S., N. S. Keller, O. Rouxel, and J. C. Alt (2012), Sulfur-33 constraints on the origin of secondary pyrite in altered oceanic basement, *Geochimica et Cosmochimica Acta*, *87*, 323-340.

Ono, S., B. Wing, D. Johnston, J. Farquhar, and D. Rumble (2006), Mass-dependent fractionation of quadruple stable sulfur isotope system as a new tracer of sulfur biogeochemical cycles, *Geochimica et Cosmochimica Acta*, *70*(9), 2238-2252.

Ono, S., J. L. Eigenbrode, A. A. Pavlov, P. Kharecha, D. Rumble, J. F. Kasting, and K. H. Freeman (2003), New insights into Archean sulfur cycle from mass-independent sulfur isotope records from the Hamersley Basin, Australia, *Earth and Planetary Science Letters*, *213*(1-2), 15-30.

Oosting, S. E., and K. Von Damm (1996), Bromide/chloride fractionation in seafloor hydrothermal fluids from 9-10°N East Pacific Rise, *Earth and Planetary Science Letters*, *144*, 12.

Otake, T., A. C. Lasaga, and H. Ohmoto (2008), Ab initio calculations for equilibrium fractionations in multiple sulfur isotope systems, *Chemical Geology*, *249*(3-4), 357-376.

Penniston-Dorland, S. C., E. A. Mathez, B. A. Wing, J. Farquhar, and J. A. Kinnaird (2012), Multiple sulfur isotope evidence for surface-derived sulfur in the Bushveld Complex, *Earth and Planetary Science Letters*, *337-338*, 236-242.

Pester, N. J., K. Ding, and W. E. J. Seyfried (2013), Vapor-Liquid Partitioning of Alkaline Earth and Transitions Metals in NaCl-Dominated Hydrothermal Fluids: An Experimental Study Conducted at 360-460 °C, Univerisity of Minnesota, Minneapolis, MN.

Pester, N. J., K. Ding, and W. E. J. Seyfried (2014), Magmatic eruptions and iron volatility in deep-sea hydrothermal fluids, *Geology*, *42*, 255-258.

Pester, N. J., M. Rough, K. Ding, and W. E. Seyfried (2011), A new Fe/Mn geothermometer for hydrothermal systems: Implications for high-salinity fluids at 13°N on the East Pacific Rise, *Geochimica et Cosmochimica Acta*, *75*(24), 7881-7892.

Peters, M., H. Strauss, S. Petersen, N.-A. Kummer, and C. Thomazo (2011), Hydrothermalism in the Tyrrhenian Sea: Inorganic and microbial sulfur cycling as revealed by geochemical and multiple sulfur isotope data, *Chemical Geology*, *280*(1-2), 217-231.

Peters, M., H. Strauss, J. Farquhar, C. Ockert, B. Eickmann, and C. L. Jost (2010), Sulfur cycling at the Mid-Atlantic Ridge: A multiple sulfur isotope approach, *Chemical Geology*, *269*(3-4), 180-196.

Pokrovski, G. S., and L. S. Dubrovinsky (2011), The S3- ion is stable in geological fluids at elevated temperatures and pressures, *Science*, *331*(6020), 1052-1054.

Pokrovski, G. S., and J. Dubessy (2015), Stability and abundance of the trisulfur radical ion S3- in hydrothermal fluids, *Earth and Planetary Science Letters*, *2015*, 298-309.

Pokrovski, G. S., J. Roux, and J.-C. Harrichoury (2005), Fluid density control on vapor-liquid partitioning of metals in hydrothermal systems, *Geology*, *33*(8), 3.

Pokrovski, G. S., A. Y. Borisova, and J.-C. Harrichoury (2008), The effect of sulfur on vapor–liquid fractionation of metals in hydrothermal systems, *Earth and Planetary Science Letters*, *266*(3-4), 345-362.

Polyakov, V. B., and S. D. Mineev (2000), The use of Mossbauer spectroscopy in stable isotope geochemistry, *Geochimica et Cosmochimica Acta*, *64*, 849-865.

Polyakov, V. B., and D. M. Soultanov (2011), New data on equilibrium iron isotope fractionation among sulfides: Constraints on mechanisms of sulfide formation in hydrothermal and igneous systems, *Geochimica et Cosmochimica Acta*, *75*(7), 1957-1974.

Polyakov, V. B., and D. M. Soultanov (2012), Response to the comment by M. Blanchard, F. Poitrasson, M. Méheut, M. Lazzeri, F. Mauri, E. Balan on "New data on equilibrium iron isotope fractionation among sulfides: Constraints on mechanisms of sulfide formation in hydrothermal and igneous systems" published in Geochim. Cosmochim. Acta 75 (2011) 1957–1974, *Geochimica et Cosmochimica Acta*, *87*, 360-366.

Polyakov, V. B., R. N. Clayton, J. Horita, and S. D. Mineev (2007), Equilibrium iron isotope fractionation factors of minerals: Reevaluation from the data of nuclear inelastic resonant X-ray scattering and Mössbauer spectroscopy, *Geochimica et Cosmochimica Acta*, *71*(15), 3833-3846.

Polyakov, V. B., E. Osadchii, D. Chareev, A. Chumakov, and I. Sergeev (2013), Fe B-factors for Sulfides from NRIXS Synchrotron Experiments, *Mineral. Mag.*, *77*, 1985.

Price, F. T., and Y. N. Shieh (1979), Fractionation of sulfur isotopes during laboratory synthesis of pyrite at low temperatures, *Chemical Geology*, *27*, 8.

Rickard, D., and G. Luther (1997), Kinetics of pyrite formation by the H2S oxidation of iron (II) monosulfide in aqueous solutions between 25 and 125C: The mechanism, *Geochimica et Cosmochimica Acta*, *61*, 135-147.

Rickard, D., and G. Luther (2007), Chemistry of Iron Sulfides, *Chem. Rev.* , *107*, 514-562.

Robinson, B. W. (1973), Sulphur isotope equilibrium during sulphur hydrolysis at high temperatures, *Earth and Planetary Science Letters*, *18*, 7.

Rouxel, O., Y. Fouquet, and J. N. Ludden (2004), Subsurface processes at the lucky strike hydrothermal field, Mid-Atlantic ridge: evidence from sulfur, selenium, and iron isotopes, *Geochimica et Cosmochimica Acta*, *68*(10), 2295-2311.

Rouxel, O., W. C. Shanks, W. Bach, and K. Edwards (2008), Integrated Fe- and S-isotope study of seafloor hydrothermal vents at East Pacific Rise 9–10°N, *Chemical Geology*, *252*(3-4), 214-227.

Rustad, J. R., W. H. Casey, Q.-Z. Yin, E. J. Bylaska, A. R. Felmy, S. A. Bogatko, V. E. Jackson, and D. A. Dixon (2010), Isotopic fractionation of Mg2+(aq), Ca2+(aq), and Fe2+(aq) with carbonate minerals, *Geochimica et Cosmochimica Acta*, *74*(22), 6301-6323.

Sakai, H. (1968), Isotopic properties of sulfur compounds in hydrothermal processes, *Geochemical Journal*, *2*, 20.

Sakai, H., and F. W. Dickson (1978), Experimental determination of the rate and equilibrium fractionation factors of sulfur isotope exchange between sulfate and sulfide in slightly acid solution at 300°C and 1000 bars, *Earth and Planetary Science Letters*, *39*, 10.

Salomons, W. (1971), Isotope fractionation between galena and pyrite and between pyrite and elemental sulfur, *Earth and Planetary Science Letters*, *11*, 2.

Schauble, E. A., G. R. Rossman, and H. P. Taylor (2001), Theoretical estimates of equilibrium Fe-isotope fractionations from vibrational spectroscopy, *Geochimica et Cosmochimica Acta*, *65*, 10.

Schoonen, M. A. A., and H. L. Barnes (1991), Mechanisms of pyrite and marcasite formation from solution: III. Hydrothermal processes, *Geochimica et Cosmochimica Acta*, *55*, 13.

Schuessler, J. A., R. Schoenberg, H. Behrens, and F. v. Blanckenburg (2007), The experimental calibration of the iron isotope fractionation factor between pyrrhotite and peralkaline rhyolitic melt, *Geochimica et Cosmochimica Acta*, *71*(2), 417-433.

Seewald, J. S., and W. E. Seyfried (1990), The effect of temperature on metal mobility in subseafloor hydrothermal systems: constraints from basalt alteration experiments, *Earth and Planetary Science Letters*, *101*, 388-403.

Seo, J. H., S. K. Lee, and I. Lee (2007), Quantum chemical calculations of equilibrium copper (I) isotope fractionations in ore-forming fluids, *Chemical Geology*, *243*(3-4), 225-237.

Seyfried, W. E., and J. L. Bischoff (1979), Low temperature basalt alteration by seawater: an experimental study at 70 and 150 C, *Geochimica et Cosmochimica Acta*, *43*, 1937-1947.

Seyfried, W. E., D. R. Janecky, and M. E. Berndt (1987), Rocking autoclaves for hydrothermal experiments: II. The flexible reaction-cell system, *Hydrothermal Experimental Techniques*, 23.

Seyfried, W. E., J. S. Seewald, M. E. Berndt, K. Ding, and D. I. Foustoukos (2003), Chemistry of hydrothermal vent fluids from the Main Endeavour Field, northern Juan de Fuca Ridge: Geochemical controls in the aftermath of June 1999 seismic events, *Journal of Geophysical Research*, *108*(B9).

Shahar, A., E. D. Young, and C. E. Manning (2008), Equilibrium high-temperature Fe isotope fractionation between fayalite and magnetite: An experimental calibration, *Earth and Planetary Science Letters*, *268*(3-4), 330-338.

Shanks, W. C. (2001), Stable Isotopes in Seafloor Hydrothermal Systems: Vent fluids, hydrothermal deposits, hydrothermal alteration, and microbial processes, in *Reviews in Mineralogy and Geochemistry*, edited, p. 56.

Shanks, W. C., and W. E. Seyfried (1987), Stable isotope studies of vent fluids and chimney minerals, southern Juan de Fuca Ridge: Sodium metasomatism and seawater sulfate reduction, *Journal of Geophysical Research*, *92*, 12.

Shanks, W. C., J. K. Bohlke, and R. R. Seal (1995), *Stable isotopes in mid-ocean ridge hydrothermal systems: Interactions between fluids, minerals, and organisms*, 28 pp.

Sharma, M., M. Polizzotto, and A. D. Anbar (2001), Iron isotopes in hot springs along the Juan de Fuca Ridge, *Earth and Planetary Science Letters*, *194*, 12.

Shock, E. L., and H. C. Helgeson (1988), Calculation of the thermodynamic and transport properties of aqueous species at high pressures and temperatures: Correlation algorithms for ionic species and equation of state predictions to 5 kb and 1000C, *Geochimica et Cosmochimica Acta*, *52*, 2009-2036.

Shock, E. L., H. C. Helgeson, and D. A. Sverjensky (1989), Calculation of the thermodynamic and transport properties of aqueous species at high pressures and temperatures: Standard partial molal properties of inorganic neutral species, *Geochimica et Cosmochimica Acta*, *53*, 2157-2183.

Shock, E. L., D. C. Sassani, M. Willis, and D. A. Sverjensky (1997), Inorganic species in geologic fluids: correlations among standard molal thermodynamic properties of aqueous ions and hydroxide complexes, *Geochimica et Cosmochimica Acta*, *61*, 907-950.

Shock, E. L., E. H. Oelkers, J. W. Johnson, D. A. Sverjensky, and H. C. Helgeson (1992), Calculation of the thermodynamic properties of aqueous species at high pressures and temperatures: Effective electrostatic radii, dissociation constants, and standard partial molal properties to 1000°C and 5 kbar, *Journal of the Chemical Society, Faraday Transactions*, *88*, 23.

Sim, M. S., S. Ono, K. Donovan, S. P. Templer, and T. Bosak (2011), Effect of electron donors on the fractionation of sulfur isotopes by a marine *Desulfovibrio* sp., *Geochimica et Cosmochimica Acta*, *75*, 4244-4259.

Skulan, J. L., B. L. Beard, and C. M. Johnson (2002), Kinetic and equilibrium Fe isotope fractionation between aqueous Fe(III) and hematite, *Geochimica et Cosmochimica Acta*, *66*, 2995-3015.

Sleep, N. H., A. Meibom, T. Fridriksson, R. G. Coleman, and D. K. Bird (2004), H2-rich fluids from serpentinization: Geochemical and biotic implications, *Proceedings of the National Academy of Sciences*, *101*, 12818-12823.

Smith, J. W., S. Doolan, and E. F. McFarlane (1977), A Sulfur Isotope Geothermometer for the Trisulfide System Galena-Sphalerite-Pyrite, *Chemical Geology*, *19*, 7.

Sohn, R. A., D. Fornari, K. Von Damm, J. A. Hildebrand, and S. C. Webb (1998), Seismic and hydrothermal evidence for a cracking event on the East Pacific Rise crest at 9°50'N, *Nature*, *396*, 2.

Sverjensky, D. A., E. L. Shock, and H. C. Helgeson (1997), Prediction of the thermodynamic properties of aqueous metal complexes to 1000°C and 5 kbar, *Geochimica et Cosmochimica Acta*, *61*, 53.

Syverson, D. D., D. M. Borrok, and W. E. Seyfried (2013), Experimental determination of equilibrium Fe isotopic fractionation between pyrite and dissolved Fe under hydrothermal conditions, *Geochimica et Cosmochimica Acta*, *122*, 13.

Tanger, J. C., and H. C. Helgeson (1988), Calculation of the thermodynamic and transport properties of aqueous species at high pressures and temperatures: Revised equations of state for the standard partial molal properties of ions and electrolytes, *American Journal of Science*, *288*, 79.

Testemale, D., J. Brugger, W. Liu, B. Etschmann, and J.-L. Hazemann (2009), In-situ X-ray absorption study of Iron(II) speciation in brines up to supercritical conditions, *Chemical Geology*, *264*(1-4), 295-310.

Thode, H. G., J. Monster, and H. B. Dunford (1961), Sulphur isotope geochemistry, *Geochimica et Cosmochimica Acta*, *25*, 150-174.

Tian, Y., B. E. Etschmann, Y. Mei, P. V. Grundler, D. Testemale, J. L. Hazemann, P. Elliott, Y. Ngothai, and J. Brugger (2014), Speciation and thermodynamic properties of manganese(II) chloride complexes in hydrothermal fluids: *In situ* XAS study, *Geochimica et Cosmochimica Acta*, *129*, 77-95.

Tian, Y., et al. (2012), Speciation of nickel (II) chloride complexes in hydrothermal fluids: In situ XAS study, *Chemical Geology*, *334*, 345-363.

Truche, L., E. F. Bazarkina, G. Barre, E. Thomassot, G. Berger, J. Dubessy, and P. Robert (2014), The role of the S3- ion in thermochemical sulphate reduction: Geological and geochemical implications, *Earth and Planetary Science Letters*, *396*, 190-200.

Tutolo, B. M., X.-Z. Kong, W. E. Seyfried, and M. O. Saar (2014), Internal consistency in aqueous geochemical data revisted: Applications to the aluminum system, *Geochimica et Cosmochimica Acta*, *133*, 216-234.

Urey, H. C. (1947), The thermodynamic properties of isotopic substances, *Journal of the Chemical Society (Resumed)*, 562.

Uyama, F., H. Chiba, M. Kusakabe, and H. Sakai (1985), Sulfur isotope exchange reactions in the aqueous system: thiosulfate-sulfide-sulfate at hydrothermal temperature, *Geochemical Journal*, *19*, 14.

Von Damm, K. (2000), Chemistry of hydrothermal vent fluids from 9-10N, East Pacific Rise: "Time zero," the immediate posteruptive period, *Journal of Geophysical Research*, *105*, 19.

Von Damm, K., M. D. Lilley, W. C. Shanks, M. Brockington, A. M. Bray, K. M. O'Grady, E. Olson, A. Graham, G. Proskurowski, and t. S. S. Party (2003), Extraordinary phase separation and segregation in vent fluids from the southern East Pacific Rise, *Earth and Planetary Science Letters*, *206*, 13.

Wilkin, R. T., and H. L. Barnes (1996), Pyrite formation by reactions of iron monosulfides with dissolved inorganic and organic sulfur species, *Geochimica et Cosmochimica Acta*, *60*(21), 12.

Woodruff, L. G., and W. C. Shanks (1988), Sulfur isotope study of chimney minerals and vent fluids from 21°N, East Pacific Rise: Hydrothermal sulfur sources and disequilibrium sulfate reduction, *Journal of Geophysical Research*, *93*(B5), 4562.

Wu, L., E. M. Percak-Dennett, B. L. Beard, E. E. Roden, and C. M. Johnson (2012), Stable iron isotope fractionation between aqueous Fe(II) and model Archaen ocean Fe-Si coprecipitates and implications for iron isotope variations in the ancient rock record, *Geochimica et Cosmochimica Acta*, *84*, 14-28.

York, D. (1966), Least-squares fitting of a straight line, *Canadian Journal of Physics*, *44*, 1079-1086.

Young, E. D., A. Galy, and H. Nahahara (2002), Kinetic and equilibrium mass-dependent isotope fractionation laws in nature and their geochemical and cosmochemical significance, *Geochimica et Cosmochimica Acta*, *66*(6), 9.

Yücel, M., A. Gartman, C. S. Chan, and G. Luther (2011), Hydrothermal vents as a kinetically stable source of iron-sulphide-bearing nanoparticles to the ocean, *Nature Geoscience*, *4*, 4.

Appendix A:

Multiple Sulfur Isotope Constraints on Mass Transfer Processes during Pyrite Precipitation and Recrystallization: An Experimental Study at 300 and 350 °C

This file contains **Supplementary Information** for Chapter 2:

A.1.: Derivation of the pyrite – H_2S $^{33,34}S/^{32}S$ equilibrium fractionation extrapolation relationship

A.2.: Comparison of experimental data with equilibrium three isotope fractionation factors

A.1. Derivation of Equation *2.7*

Isotope exchange reaction between S-bearing species A and B:

$$^{34}S_A + {}^{32}S_B \leftrightharpoons {}^{32}S_A + {}^{34}S_B \qquad (A.1)$$

Isotope mass action relationship, where X and Y = ^{32}S and x and y = ^{34}S, between two S-bearing species:

$$x + Y \leftrightharpoons X + y \qquad (A.2)$$

The rate equation is:

$$\frac{dx}{dt} = -\frac{dy}{dt} = -k_f xY + k_b yX \qquad (A.3)$$

k_f and k_b are forward and backward second order rate constants, respectively. *Ohmoto and Lasaga* [1982] approximated that the ^{32}S species are abundant and do not change their concentration with time (i.e., X and Y are not a function of time, x+X and y+Y are essentially constant). Under this assumption, the solution of equation (*A.3*) for $x(t)$ is:

$$x(t) = (x_0 - x_e)F + x_e \qquad (A.4)$$

where, F is a degree of equilibrium: $F = \exp(-(k_f Y + k_b X))t$. The subscripts "0" and "e" represent time zero and at equilibrium after infinite time, respectively. It is straightforward to show that:

$$\delta(t) = (\delta^0 - \delta^e)F + \delta^e \qquad (A.5)$$

for a small range of δ fractionation values (±5 ‰, Table A.1),

$$\Delta(t) \cong (\Delta^0 - \Delta^e)F + \Delta^e \qquad (A.6)$$

For the difference between sulfur phases, A and B, for δ^{34}S and Δ^{33}S, respectively:

$$\delta_A(t) - \delta_B(t) = (\delta_A^0 - \delta_B^0 + \delta_A^e - \delta_B^e)F + \delta_A^e - \delta_B^e \qquad (A.7)$$

$$\Delta_A(t) - \Delta_B(t) = (\Delta_A^0 - \Delta_B^0 + \Delta_A^e - \Delta_B^e)F + \Delta_A^e - \Delta_B^e \qquad (A.8)$$

At equilibrium, $\Delta_A^e - \Delta_B^e = 0$. Then, from the above two equations:

$$\delta_A(t) - \delta_B(t) = \frac{(\delta_A^0 - \delta_B^0 + \delta_A^e - \delta_B^e)}{\Delta_A^0 - \Delta_B^0} \Delta_A(t) - \Delta_B(t) + \delta_A^e - \delta_B^e \qquad (A.9)$$

Plot of $\delta_A(t) - \delta_B(t)$ vs. $\Delta_A(t) - \Delta_B(t)$ (Table A.1) produces a line with a *y*-intercept that is the $^{34}S/^{32}S$ equilibrium fractionation between species A and B, $\delta_A^e - \delta_B^e \approx 10^3 ln^{34}\alpha_{A/B}$.

Table A.1.

Table A.1: Multiple sulfur isotope data for the Pyrite – H_2S partial exchange experiments after 3384 hours of recrystallization at 350°C and 500 bars

Pyrite and H_2S	$\delta^{33}S$	$\delta^{34}S$	$\Delta^{33}S$
5-1 Pyr1	0.982	1.954	-0.024
5-2 Pyr2	-0.794	-1.503	-0.020
5-3 Pyr3	2.055	4.087	-0.048
5-4 Pyr4	6.651	13.089	-0.068
5-1 H_2S	2.704	5.330	-0.038
5-2 H_2S	-0.722	-1.407	0.002
5-3 H_2S	0.973	1.947	-0.030
5-4 H_2S	5.098	9.989	-0.034
Product Pair	$\delta^{33}S_{Pyr} - \delta^{33}S_{H2S}$	$\delta^{34}S_{Pyr} - \delta^{34}S_{H2S}$	$\Delta^{33}S_{Pyr} - \Delta^{33}S_{H2S}$[a]
5-1 Pyr1 – H_2S	-1.722	-3.376	0.014
5-2 Pyr1 – H_2S	-0.072	-0.097	-0.022
5-3 Pyr1 – H_2S	1.082	2.140	-0.018
5-4 Pyr1 – H_2S	1.553	3.100	-0.034

The average precision for $\delta^{33}S$ and $\delta^{34}S$ is ~0.010 ‰ (1σ). The average precision for $\Delta^{33}S$ is 0.006 ‰ (1σ). The 1σ error for $\delta^{33,34}S$ and $\Delta^{33}S$ pyrite – H_2S fractionation pairs is 0.014 and 0.008‰, respectively. [a]The $\Delta^{33}S$ fractionation is derived from the $^{33}S/^{32}S$ and $^{34}S/^{32}S$ fractionations between pyrite and H_2S as described for the product pairs.

A.2. Three Isotope Fractionation Factor Relationships, $^{33}\lambda$ and $^{33}\theta$

Mass-dependent fractionation is expressed as follows [*Hulston and Thode*, 1965; *Miller*, 2002; *Young et al.*, 2002]:

$$^{33}\alpha_{A/B} = {}^{34}\alpha_{A/B}{}^{33\lambda} \qquad (A.10)$$

where the exponential term, known as the observed three-isotope fractionation factor, is defined as $^{33}\lambda$, and can be calculated from measured S isotope data between different S-bearing substances [*Miller*, 2002]:

$$^{33}\lambda = \frac{\delta^{33}S'_A - \delta^{33}S'_B}{\delta^{34}S'_A - \delta^{34}S'_B} \qquad (A.11)$$

The observed three isotope fractionation factor, $^{33}\lambda$, is a direct observation of a net process, whereas the theoretical equilibrium mass-dependent fractionation, $^{33}\theta$, is a representation of intrinsic isotopic equilibrium between two S-bearing substances [*Johnston et al.*, 2005; *Ono et al.*, 2007; *Ono et al.*, 2006]:

$$^{33}\theta = \left[\frac{ln(^{33}\alpha_{A-B})}{ln(^{34}\alpha_{A-B})}\right] \qquad (A.12)$$

The equilibrium mass dependent fractionation, $^{33}\theta$, between SO_4 and pyrite or H_2S is approximately 0.5153, whereas the equilibrium dependent fractionation between pyrite and H_2S is approximately 0.5150 at 300 - 350 °C. The convergence of experimental data, $^{33}\lambda$, towards these $^{33}\theta$ values is indicative of the mineral – fluid system approaching isotopic equilibrium.

A.2.1. Time Series Changes in $^{33}\lambda$ relative to $^{33}\theta$: Pyrite Precipitation and Recrystallization

The observed $^{33}\lambda$ value (Table A.2) between the final SO_4 and pyrite for Expt. #1 at 300 °C deviates significantly from equilibrium mass dependent fractionation

predictions, with $^{33}\lambda$=0.5175±0.0004 (1σ), which is consistent with the gross disequilibrium displayed by traditional $^{34}S/^{32}S$ isotope fractionation data (see main text). The observed $^{33}\lambda$ values at 350 °C (Expt. #2 - 4) (Table A.2) are in better agreement with mass dependent equilibrium predictions, suggesting that $^{33}\lambda$ between final SO_4 and pyrite is slowly converging towards the canonical values of ~0.5150-0.5153 with an increasing degree of reaction progress/isotopic exchange. The relatively large errors associated with $^{33}\lambda$ values for pyrite − H_2S fractionation (not shown), however, requires that caution be applied to the interpretation and application of these particular data [*Johnston et al.*, 2007].

The $^{33}\lambda$ values describing the fractionation between SO_4 and H_2S during the early stages of the 350°C experiments, #2 and #3, significantly deviate from mass-dependent predictions, $^{33}\lambda$~0.5134-0.5141±0.0004 (1σ), similar to what is observed during the initial stages of Expt. #1 at 300 °C. Similarly, the initial stage $^{33}\lambda$ value from Expt. #4 at 350 °C is different from mass dependent predictions (0.5168), although greater than. In general, with increasing extents of reaction progress, SO_4−H_2S $^{33}\lambda$ values converge towards equilibrium, ~0.515, 0.5151±0.0004 (Table A.2).

The most notable change in $^{33}\lambda$ values is for SO_4−pyrite fractionation, where the data clearly exhibit an approach to equilibrium between the two major S-reservoirs with increasing extents of reaction time (Table A.2). The data during the early stages of the precipitation and recrystallization event exhibit anomalous $^{33}\lambda$ values and eventually converge towards ~0.515, indicative of equilibrium, within uncertainty of the measurements.

Table A.2

Table A.2. Three isotope fractionation factors between SO_4^{2-} and H_2S or Pyrite.							
#1 (300 °C)		**#2 (350 °C)**		**#3 (350 °C)**		**#4 (350 °C)**	
Time (hours)	**$^{33}\lambda$ ($SO_4 - H_2S$)**	**Time (hours)**	**$^{33}\lambda$ ($SO_4 - H_2S$)**	**Time (hours)**	**$^{33}\lambda$ ($SO_4 - H_2S$)**	**Time (hours)**	**$^{33}\lambda$ ($SO_4 - H_2S$)**
0	-	0	-	0	-	0	-
0.8	0.5134	0.3	0.5141	0.6	n.a.	0.5	0.5168
56	0.5143	333	0.5137	720	0.5159	25	0.5156
68	0.5157	399	0.5151	1082	0.5163	46	0.5151
						865	0.5162
						3553	0.5151
						4297	0.5151
Time (hours)	**$^{33}\lambda$ ($SO_4 - Pyrite$)**	**Time (hours)**	**$^{33}\lambda$ ($SO_4 - Pyrite$)**	**Time (hours)**	**$^{33}\lambda$ ($SO_4 - Pyrite$)**	**Time (hours)**	**$^{33}\lambda$ ($SO_4 - Pyrite$)**
68	0.5175	399	0.5160	1082	0.5157	4297	0.5147
1σ error for $^{33}\lambda$ between SO_4 and H_2S and between SO_4 and pyrite is ~0.0004-0.0005 ‰. $^{33}\lambda$ between pyrite and H_2S is not shown due to the large inherent error associated with this particular calculation, i.e. $1\sigma > 0.01$ ‰.							